DNA nanostructures for biotechnological applications

Bouran Sohrabi

University College London

A thesis submitted in partial fulfilment of the requirements of the degree of Doctor of Philosophy

Declaration

I, Bouran Sohrabi, confirm that the work presented in this thesis is my own. Where information has been derived from other sources, I confirm that this has been indicated in the thesis.

July 2018

Abstract

Deoxyribonucleic acid (DNA) is a versatile biomolecule which can be used for the rational design and assembly of nanoscale structures. This thesis explores the use of functional DNA-enzyme nanostructures for applications in biocatalysis and for directed motion on the nanoscale. In the first part of this thesis, a DNA scaffold was outlined for the display and immobilization of enzyme cascades. Confinement or spatial organization of enzyme cascades is adopted in biological systems to prevent loss of reactive intermediates and to facilitate substrate conversion in chemically complex and crowded intracellular environments. We adopt a strategy to create concentrated enzyme assemblies directed by a DNA structure generated by Φ29 rolling circle amplification (RCA). These DNA assemblies, DNA nanoballs, were investigated for the display of two bi-enzyme systems. Firstly, a horseradish peroxidase and glucose oxidase enzyme pair, and secondly, a transaminase and norcoclaurine synthase bi-enzyme system for the synthesis of biotechnologically relevant benzylisoquinoline (BIA) precursors. The second part of this thesis concerns the use of enzymatic catalysis as a means of affecting the motion of a nanoscale DNA structure. Molecular movement on the micro and nanoscales is a fundamental feature of biological systems, and recreating this functionality represents an important step in the realization of intelligent synthetic devices for directed transport and chemotaxis in response to stimuli. While directed motion has been shown for DNA structures on predefined tracks to which they are hybridized, enzymatic catalysis has not been investigated as an approach to controlling the motion of DNA nanostructures. We show that the motion of a DNA structure tethered to multiple lysine decarboxylase molecules is enhanced by its substrate, L-lysine the ‘fuel’, in a concentration dependent manner, based on nanoparticle tracking analysis (NTA) and DLS analyses.

Impact Statement

Biomolecular based technologies find use in a range of applications, such as diagnostics, next generation sequencing and personalised medicine. The ability to accurately manipulate biomolecules on the micro and nanoscales is essential for the creation and development of such technologies. DNA nanotechnology describes the rational design and construction of nanometre scale structures using DNA, and it has proven to be an unparalleled technology for the purpose of producing functional structures and objects on the nanoscale. The potential for DNA as the basis for biomolecular based technologies or products is therefore considerable. In this thesis, DNA nanotechnology was applied to the area of biocatalysis, specifically the immobilisation of enzyme cascades on DNA nanostructure for the production of biotechnologically relevant benzylisoquinoline precursors. Enzymatic catalysis was also investigated as a means of actuating the motion of a DNA nanostructure in response to an external substrate, L-lysine. This was explored in the context of a growing interest in self autonomous nanostructures for directed transport and, potentially, nanomedicine. The findings of this thesis contribute to our knowledge of enzymatic reactions displayed on nanoscale DNA structures, and the feasibility of such devices. More broadly it offers insights into the challenges associated with the manipulation of biological systems and their application to biotechnologically relevant areas.

Acknowledgements

I would like to express my gratitude to Professors John Ward and Gary Lye for their supervision, advice and for checking this thesis. I'd like to also thank members of Lab 4.02 in the department of biochemical engineering and the chemical biology lab in the department of chemistry for their help and assistance in various aspects of this project. Lastly, I would like to acknowledge the EPSRC and the department of biochemical engineering for funding this PhD.

Contents

Table of tables

Table of equations

Table of figures

List of Abbreviations

3-HPA	*3-hydroxyphenethylamine*
ADP	*Adenosine diphosphate*
AEC	*Anion exchange chromatography*
ATP	*Adenosine triphosphate*
BMC	*Bacterial microcompartment*
cP	*Centipoise*
Cy3	*Cyanine 3*
Cy5	*Cyanine 5*
Da	*Dalton*
DLS	*Dynamic light scattering*
DNA	*Deoxyribonucleic acid*
dNTP	*Deoxyribonucleotide Triphosphate*
DTT	*1,4-dithiothreitol*
DX	*Double-crossover*
E. coli	*Escherichia coli*
EDTA	*Ethylenediaminetetraacetic acid*
EtBr	*Ethidium bromide*
FLUDT	*Fluorescein-dT*
FPLC	*Fast protein liquid chromatography*
FPS	*Frames per second*
GOx	*Glucose oxidase*
IMAC	*immobilized metal affinity chromatography*
IPTG	*isopropyl β-D-1-thiogalactopyranoside*
K_d	*Dissociation constant*
LB	*Luria-Bertani*
m/z	*Mass-to-charge ratio*
MSD	*Mean-squared displacement*

MW	*Molecular weight*
MWCO	*Molecular weight cut off*
NAD	*Nicotinamide adenine dinucleotide*
NB	*Nanoball*, *Nanoball*
NCS	*Norcoclaurine synthase*
NHS ester	*N-hydroxysuccinimide esters*
NPs	*Nanoparticles*
nt	*nucleotide*
PAGE	*Polyacrylamide gel electrophoresis*
PCS	*Photon correlation spectroscopy*
PEG	*Polyethylene glycol*
pfu	*Plaque forming units*
pI	*Isoelectric point*
Pi	*Phosphate*
PLP	*Pyridoxal-5'-phosphate*
Q-TOF	*Quadrupole time-of-flight mass spectrometer*
RNA	*Ribonucleic acid*
RPM	*Revolutions per minute*
S. cervisea	*Saccharomyces cerevisiae*
sCMOS	*scientific complementary metal-oxide-semiconductor*
SD	*Standard deviation*
SDS	*Sodium dodecyl sulfate*
SEM	*Standard error of the mean*
SPM	*Scanning probe microscopy*
ssDNA	*Single stranded deoxyribonucleic acid*
sulfo-SMCC	*sulfosuccinimidyl 4-(N-maleimidomethyl)cyclohexane-1-carboxylate*
TAm	*Transaminase*
TAMRA	*Carboxytetramethylrhodamine*
TBE	*Tris/Borate/EDTA*

UHPLC	*Ultra high preformance liquid chromatography*
UV/VIS	*Ultraviolet–visible*
X-Gal	*5-Bromo-4-Chloro-3-Indolyl β-D-Galactopyranoside*
YT	*Yeast extract-tryptone*

Chapter 1

Introduction

1.1 Deoxyribonucleic acid (DNA)

Deoxyribonucleic acid (DNA) is a biopolymer of nucleotides which serves as the chemical basis for genetic inheritance in all organisms[1]. The structure of a nucleotide comprises of three components, a nitrogenous heterocyclic base (a pyrimidine or purine) a pentose sugar (2-deoxy-D-ribose) and a phosphate group[2] (Figure 1-1). Each nucleotide is joined to another through a phosphate diester bond, from the 5' carbon atom of a pentose sugar to the 3' position (hydroxyl group) of its neighbour[2,3]. The phosphodiester linkage also gives rise to the chemical polarity of DNA; its 5'-> 3' directionality[2] (Figure 1-3). dsDNA assumes an anti-parallel double helical structure[4], where the DNA strands are held together through hydrogen bonding between complementary nucleobases, A to T and G to C, this is known as canonical Watson-Crick base pairing[4]. Hydrogen bonding between the bases occurs due to the acid-base behaviour of the nucleotides; the NH groups make good hydrogen bond donors, while the C=O and ring nitrogen atoms act as hydrogen bond acceptors[5]. The A to T and G to C base pairings are held by two and three hydrogen bonds respectively[5], which is illustrated in figure 1-2.

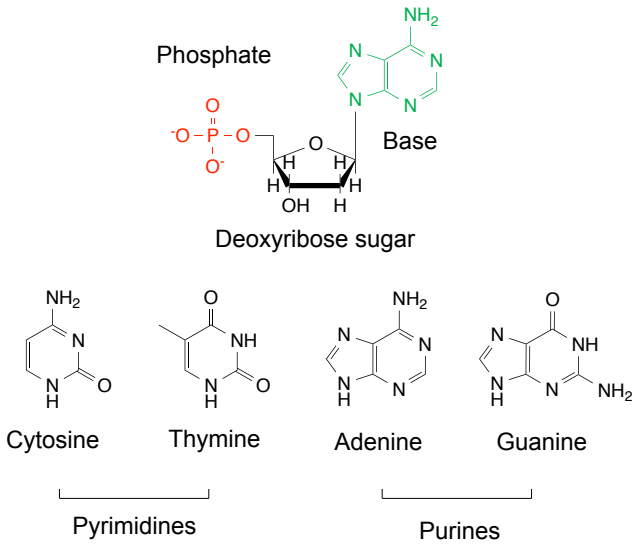

Figure 1-1 The structure of a nucleotide. A nucleotide contains a cyclic nitrogen containing base, either a pyrimidine or purine, a five carbon sugar and a phosphate group, the base is

joined to pentose sugar through a N-glycosidic bond[3]. The sequence of bases, A,T G or C constitute the chemical basis of hereditary in all organisms[6].

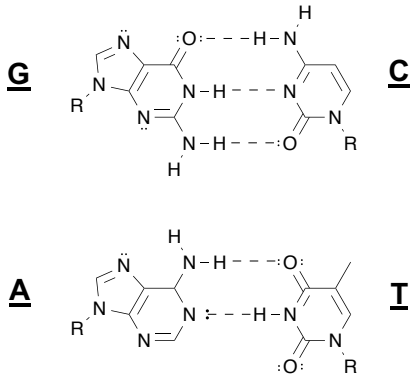

Figure 1-2 Canonical Watson crick base pairing. Top: Guanine base pairs to cytosine through three hydrogen bonds. Bottom: Base pairing between adenine to thymine occurs through two hydrogen bonds.

Double stranded DNA (dsDNA) can assume different helical forms, B-, A-, or Z-forms, depending on relative humidity, salt concentration, as well as the chemical composition of the DNA sequence[6,7]. Under high relative humidity and in aqueous solution, dsDNA assumes the B-form structure (the Watson-Crick model), which is also the main form encountered under physiological conditions[6,7]. B-form DNA is a right-handed helix, where base pairs are stacked above one another perpendicular to the helical axis[7]. The stacking of base pairs and their tilt give rise to major and minor grooves along the double helix[8] (Figure 1-4).

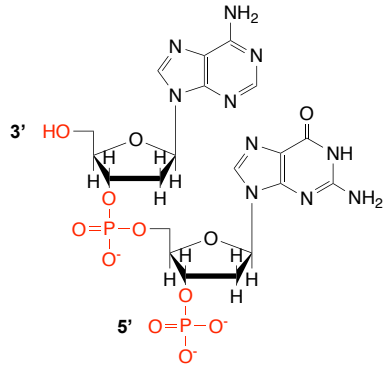

Figure 1-3 The covalent structure of DNA. Showing the 3' to 5' directionality of DNA. Nucleotides are joined to one another through a phosphodiester linkage on the 5' and 3'

carbon atoms of the pentose sugar. A heterocyclic base, either a pyrimidine or purine is joined via a N-glycosidic bond at the 1' position on the pentose sugar[3,6].

For B-form DNA, a full helical turn equates to approximately 10 nucleotides (10nt/turn), giving a rise of 0.34nm per residue and a helix diameter of 2nm[6] (figure 1-4). Water molecules hydrate the phosphate backbone and interact with the minor and major grooves to confer stability to the double helix[5]. As well as hydrogen bonding between complementary base pairs, stacking interactions between neighbouring bases stabilise the helical structure and minimize unfavourable interactions between the heterocyclic (hydrophobic) bases and the surrounding aqueous (polar) solvent[5]. DNA is also an inherently flexible molecule, which can adopt many different structural conformations[6,9].

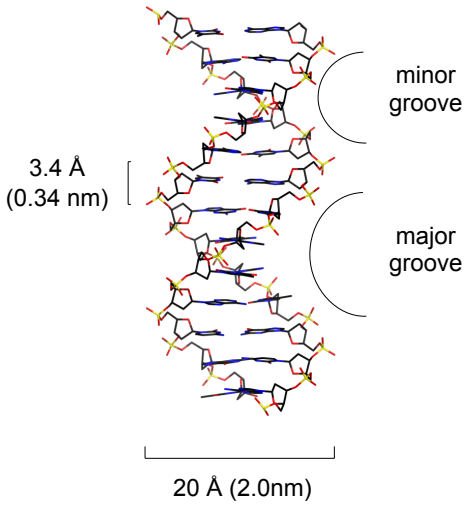

Figure 1-4 The three dimensional structure of B-form DNA (PDB: 1BNA). The major and minor grooves which run along the duplex are highlighted above. B-form DNA constitutes the Watson-Crick model of DNA[6,7]. It is thought to represent the main conformation of DNA *in vivo*[10]. The diameter of a duplex is approximately 2nm, and the rise per base pair is 0.34nm, which corresponds to a full helical turn of 10.5bp[6]. The phosphate group constituting the backbone is depicted in yellow/red and the bases in black.

Through the sequence of nucleotide bases, deoxyribonucleic acid (DNA) encodes the instructions for the expression and replication of genetic information in all organisms[4]. Intracellularly, DNA also serves roles which are dependent on its 'quaternary' structure. For example, the process of homologous genetic recombination relies on the formation of a four-

armed DNA crossover structure known as a Holliday junction[11,12] (Figure 1-5). Other notable examples of quaternary DNA structure include the DNA cruciform; a cross shaped DNA which is generated from palindromic sequences[13]. These structures play an important role in a range of biological processes, such as the regulation of gene expression, replication and the process of genetic recombination[13]. In eukaryotes, DNA is organized into dense protein-DNA assemblies, known as the nucleosome core particle, which involves the association of DNA with an octameric protein complex (NCP)[14]; the NCP constitutes the basic repeating unit of chromatin in eukaryotes[14].

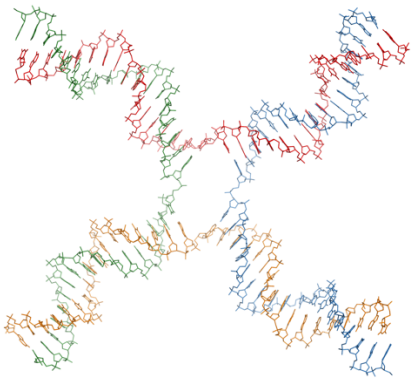

Figure 1-5 The molecular structure of an unstacked Holliday junction (PDB:3CRX). Holliday junctions (HJs) are four-way branched DNA structures which occur as intermediates during the process of genetic recombination, integration and DNA repair[11]. The unstacked or 'open' conformation, shown above, is observed at low salt concentrations[15].

1.1.1 DNA for the construction of nanoscale architectures - hierarchal assembly based on DNA motifs or tiles

The predictable base pairing pattern that constitutes the DNA duplex, that A pairs with T and G with C, has been exploited for the design and assembly of rationally designed nanostructures[16–18] with precise control over spatial and temporal structure[16,17]. On one level, DNA structures can be assembled from discrete DNA tiles or motif structures. Synthetic branched DNA can be assembled to create discrete 'closed' target objects[19], or regular periodic arrays/lattices[18]. Examples of such motifs include the four-way junction tile[18] and DX double-crossover motifs (where two parallel helices are connected to one another twice by crossovers)[20], these component structures are hybridized to one another through complementary 'sticky ends' or through covalent ligation[21,22]. This approach has been used to create a range of structures, including helix bundles[9], nanotubes[23,24], numerous two dimensional

lattices and arrays[16,17] (figure 1-6), and discrete three dimensional geometric objects[27–29]. Figure 1-6 (a) illustrates the principle of DNA tile assembly, involving a 4 way junction tile which anneals to form a periodic array based on the complementarity of its ends.

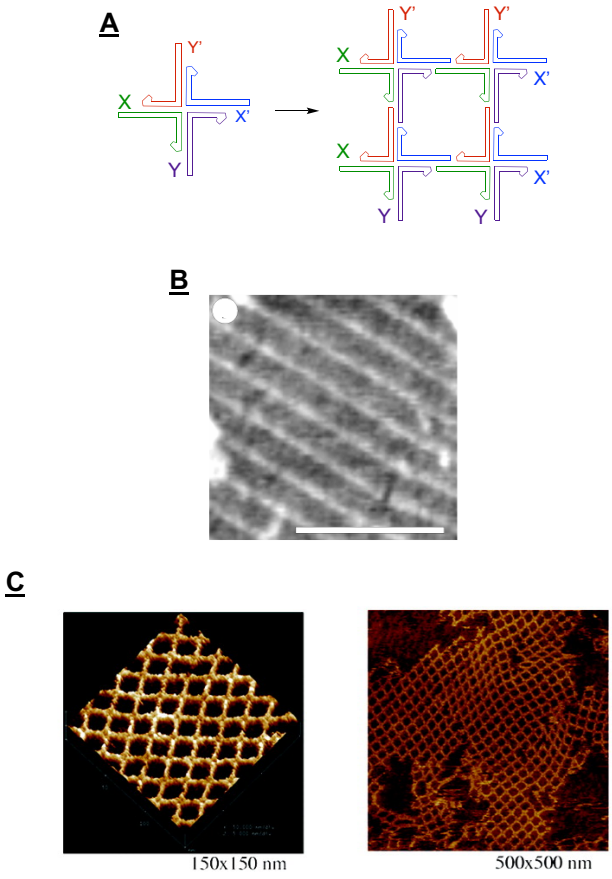

Figure 1-6 Assembly of DNA motifs. **(A)** The self-assembly of a DNA four-way junction tile with complementary ends to form an interconnected lattice. **(B)** AFM micrograph of a DNA lattice based on the assembly of a rectangular double-crossover (DX) DNA tile, scale bar = 300 nm, adapted with permission from ref. 30, Macmillan Publishers Limited. **(C)** Two AFM micrographs demonstrating the self-assembly of a 2D nanogrid with a corrugated design, adapted with permission from ref. 31, American Association for the Advancement of Science (AAAS). Here, a four-armed tile associates with itself such that neighbouring tiles face opposite planes (i.e. up or down); in this way, inherent surface curvature is cancelled to produce lattice nanogrid structures.

1.1.2 Scaffold based DNA nanostructure

Alternatively, DNA nanostructures may be formed using a single stranded DNA which is 'folded' into a desired structure using shorter DNA oligonucleotides to guide the assembly

process. This approach has been used for the assembly of a patterned DNA lattice (barcode lattice) using DNA tiles to direct the assembly of a longer ligated DNA scaffold strand[32], and similarly for the formation of a three dimensional DNA octahedron, from a 1.7 kb DNA strand directed by five short helper DNA[33]. The DNA origami method[34] describes the process of 'folding' a single-stranded DNA to form two dimensional shapes by annealing multiple 'staple strands' (typically 15-60 nt in length) to form periodic crossovers between antiparallel helices. Crossovers are positioned every odd half turn, alternating along the length of a helix to join adjacent helices in the same plane. The DNA origami method is depicted in figure 1-7.

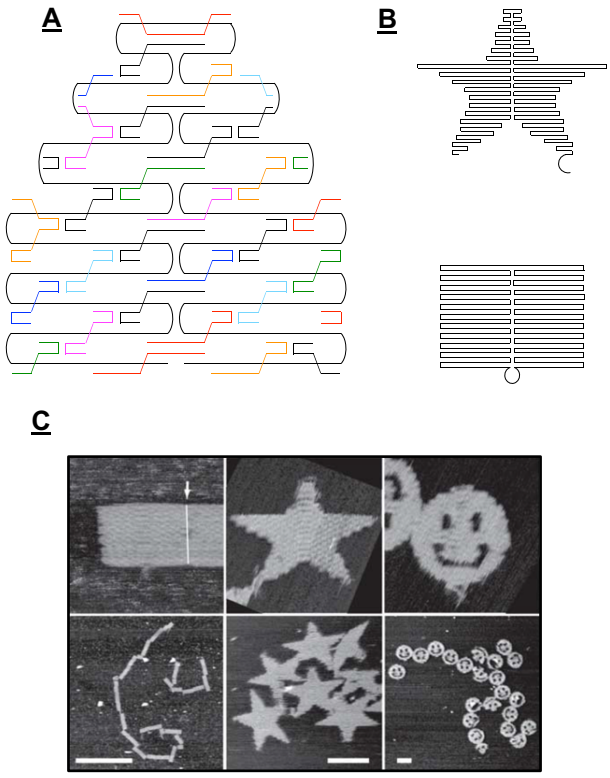

Figure 1-7 DNA origami. (A) DNA origami involves folding a single scaffold ssDNA (black line) by annealing multiple 'staple' DNA oligonucleotides (depicted in multiple colours) to the longer scaffold. Parallel helices are joined through periodic crossovers along the length of helices by staple strands. **(B)** Potentially any arbitrary shape can be constructed using DNA origami; folding paths for a star and rectangle are shown[34]. **(C)** Atomic force microscopy (AMF) micrographs of annealed DNA origami structures. Adapted with permission from ref. 34, Macmillan Publishers Limited.

The assembly process proceeds via a one-pot reaction comprising of template and excess staple strands. Typically, the scaffold ssDNA is derived from a viral genome, for example

bacteriophage M13, however, other ssDNA 'scaffolds' may be used[35] such as miniature sized scaffolds[36], or those derived from phagemid systems. The DNA origami method has proven to be highly versatile, and there are numerous examples of two dimensional DNA structures constructed using this particular approach[34]. Three-dimensional architectures have also been described, such as triangular, rectangular, and pentagonal prisms[37,38], a cube based on connected DNA origami panels[39–41] and a DNA box with a dynamic lid[41]. In these examples 2D DNA origami structures are connected using strand cross-overs at interfacing edges to create 3D objects.

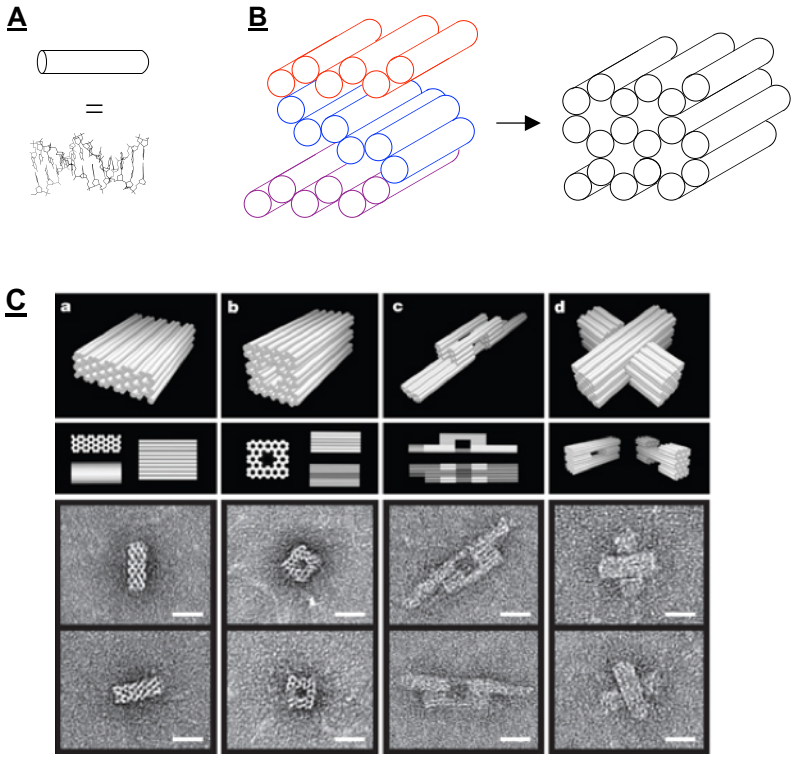

Figure 1-8 Three-dimensional DNA origami. **(A)** Each cylinder represents a DNA double helix. **(B)** Three layers of connected DNA duplexes are arranged onto one another according to a honeycomb lattice arrangement. Layers of DNA double helices are connected to one another through crossovers to form a compacted three-dimensional object; crossovers occur every 240° along a helix (every 7 bps). **(C)** The top rows show cylinder models of target three dimensional objects. Bottom 2 rows: show corresponding transmission electron (TEM) micrographs of particles, scale bar: 20nm. Adapted with permission from ref. 42, Macmillan Publishers Limited.

Separately, a scaffolded approach for constructing three dimensional, or multilayer DNA structures has been described[42]. This is achieved through packing arrays of interconnected antiparallel helices, which follow a hexagonal honeycomb or rectangular lattice arrangement[42]. As with two dimensional DNA origami described above (figure 1-7), structures are formed through a one pot reaction in which a ssDNA is annealed to many helper DNA oligonucleotides to guide the folding of the scaffold strand[42], usually over an extended annealing step[43,44]. Figure 1-8 shows a schematic representation of a three-dimensional DNA origami object assembled according to this approach. Each helix is connected to three adjacent helices through a series of crossovers. For a multilayer object following a honeycomb arrangement, crossovers occur every 240° along a helix, which corresponds to a crossover every 7 bps. Other structural characteristics can be introduced to three dimensional objects constructed in this way, such as curvature[45], through super twisted or bent helical axes by adding or removing base pairs along helical layers, and tensegrity[46]. Computational tools have been developed to assist the design and fabrication of three-dimensional DNA origami nanostructures. Notably caDNAno[47], a three dimensional origami design tool, as well as CanDo[48], a predictive tool for nanostructure conformation.

1.1.3 Enzymatically derived DNA nanostructures and other methods for the construction of DNA based structures

As well as sequence dependent hybridization, enzymatic methods can be used to synthesize or manipulate DNA nanostructures, through enzymatic ligation or DNA polymerization. For instance, 'sticky' ended DNA tiles can be covalently closed to form DNA arrays or dendrimer-like assemblies[49,50]. Equally, DNA structures may be replicated or synthesized using DNA polymerisation. One particular DNA polymerization method, rolling circle amplification (RCA), is notable since it involves the amplification of a circularised or covalently closed ssDNA or RNA template in a highly processive (or 'rolling') manner. This property has made it a useful technique for the synthesis and replication of DNA structures and templates, due to its exceptional strand displacement activity and ability to synthesize through secondary DNA structure. It has been used to replicate a four arm DNA nanojunction[51] and DNA nanotubes[52–54], as well as for the *in vivo* cloning of artificial DNA nanostructures embedded within a phagemid[55]. Disordered or unstructured DNA objects can also be synthesised using RCA, such as fluorescent structural DNA particles[56] - incorporating modified nucleotide triphosphates (dNTPs), and liquid crystalline DNA 'nanoflowers'[57,5859]. Assembly components, such as scaffold and 'staple' strands have also been synthesised in this way[60]. This has been shown for the assembly of DNA nano wires and plate structures, using thousands of RCA synthesized nucleotide(nt)-long single strand DNAs[61,62].

The self-assembly of DNA nanostructures is not limited to sequence dependent hybridization or enzymatic methods. Chemical moieties may also be used to control and direct the assembly of DNA structures: supramolecular chemistry. Self-assembly may be mediated by hydrophobic, electrostatic or affinity based interactions, through either organic and inorganic species to connect multiple DNA nanostructures or DNA strands at angles, junctions or vertices. Perylene bisimide caps[63] have been used to assemble DNA triangles using Y shaped DNA tiles; dendritic alkyl chains for the assembly of DNA cages through hydrophobic interactions[64]; and the use of polyethylene glycol and poly(p-phenylene ethynylene) to assemble micron sized double-stranded (ds) DNA−organic molecule hybrid structures[65].

1.2 Functionalized DNA nanostructures

Although DNA is a highly amenable molecule for the design and assembly of nanoscale architectures, supported by the wide range of structures and assembly methods described, it is a chemically inert molecule; a feature which is essential for its role as the chemical basis for hereditary. Unlike proteins, whose primary sequence of amino acids impart a range of physical and chemical properties through their respective side chains, a DNA nanostructure must be 'functionalised' in order to introduce equivalent properties or desired functionalities. The commercial availability of DNA through solid phase phosphoramidite synthesis, has meant that DNA oligonucleotides can be modified with a range of chemistries to impart additional biomolecular, organic and inorganic moieties onto DNA nanostructures[66–70].

Typically, a target molecule is recruited through modified DNA oligonucleotides to a complementary DNA or supporting nanostructure. These methods could include, non-covalent coupling methods, such as biotin-streptavidin coupling, using biotinylated oligonucleotides to a (strept)avidin modified target[71–73], or recruitment of polyhistidine tagged proteins to DNA structures through the his tag-nickel (II)-nitrilotriacetate (Ni-NTA) coordination, which has been demonstrated for a number of structures[24,74–77]. Covalent bio conjugate chemistries, e.g. Thiol/NHS ester (between amine and thiol groups) and click chemistries, are particularly useful for the functionalisation of DNA with biomolecules as they exploit the availability of accessible amine (of lysine side chains) or sulfhydryl groups (cysteine side chains) on target proteins. In addition to the 5' and 3' positions of DNA oligonucleotides, modifications can also be introduced on the phosphate backbone. Such as phosphorothioate modified DNA (the phosphorothioate bond substitutes a non-bridging oxygen atom with sulphur on a phosphate group), to align protein molecules on the DNA backbone[78,79].

As well as for the recruitment of molecules of interest to DNA structures, the addition of chemical groups can impart altered chemical or physical properties to DNA objects, such as hydrophobicity, redox and photophysical properties, for specific applications. For instance, DNA structures have been modified with cholesterol or other hydrophobic molecules to promote their association, or manipulate, lipid bilayers or liposomes[80,81]. This has been shown for artificial DNA 'nanopores'[82–85] which used cholesterol and porphyrin moieties to promote their association with lipid bilayers. Similarly, DNA-metal complexes can impart properties to create plasmonic structures[86,87] with optically active properties[86–88], such as DNA functionalised Au NPs.

1.2.1 Methods for the functionalization of DNA with biomolecules

Proteins and peptides represent an important group of target molecule for the functionalisation of DNA nanostructures as they confer biologically relevant properties and activities. While DNA oligonucleotides can be modified with a variety of chemistries, such as thiol, amino, biotin, and azide/alkyne modifications, at various positions (3',5' or internally), the covalent modification of a target protein or peptide of interest is usually restricted to the ionisable side chains of amino acids. They include, aspartic acid, glutamic acid, lysine, arginine, cysteine, histidine, and tyrosine residues. Two biomolecules can be crosslinked using a heterobifunctional crosslinker, commonly SMCC or SPDP, which comprise of an amine reactive NHS ester and a thiol reactive maleimide or pyridyldithiol group. The protein or amine of a target molecule is activated through the N-hydroxysuccinimide NHS ester moiety of the crosslinker, the maleimido activated protein may then react with a thiol modified target (figure 1-9). This particular method is advantageous since any protein or amine containing molecule can be targeted (provided those groups are accessible, particularly in the case of proteins), and yields non-reversible covalent coupling between target molecules.

Another commonly used covalent bioconjugate technique is the copper-free azide-strained alkyne reaction (figure 1-9). This method involves the reaction between an azide and a strained alkyne, such as dibenzocyclooctyne (DIBO) or ibenzocyclooctyne Group (DBCO), introduced onto the biomolecules of interest. The reaction proceeds via a strain-promoted alkyne azide cycloaddition (SPAAC) to form a triazole linkage, and benefits from high reactive specificity between the diarylcyclooctynes towards the azide, and high quantitative yield.

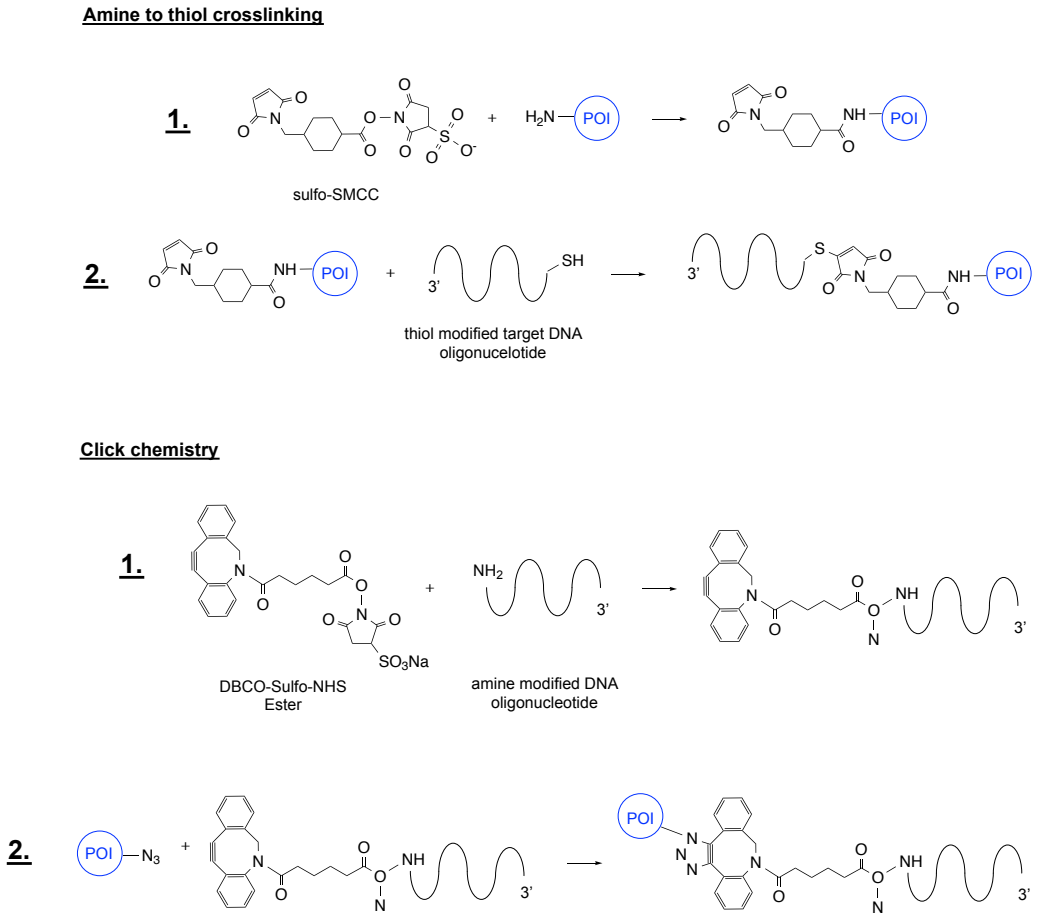

Figure 1-9 Covalent strategies for the generation of DNA oligonucleotide-protein conjugates. Amine to thiol crosslinking: covalent coupling between a thiol modified oligonucleotide and protein containing an amine group using the heterobifunctional crosslinker sulfo-SMCC. The bifunctional crosslinker comprises of an NHS ester and maleimide group. **(1)** A protein of interest is activated through the NHS ester portion of the crosslinker which is reactive towards primary and secondary amine groups. **(2)** The protein of interest is subsequently coupled to a thiol modified DNA oligonucleotide of interest through the maleimide portion of the linker. **Click chemistry:** depiction of a DNA-protein labelling strategy based on copper-free click chemistry. **(1)** A 5' amine modified DNA oligonucleotide is modified with DBCO-Sulfo-NHS ester, in order to introduce a dibenzocyclooctyne (DBCO) group onto the oligonucleotide. DBCO groups preferentially and spontaneously react with azide groups ($–N_3$). **(2)** Spontaneous coupling between the DBCO modified oligonucleotide and an azide modified target protein. A protein may be derivatized with an azide, for example, through surface accessible lysine residues using an NHS-azide or through incorporation of non-natural amino acid analogs, such as L-Azidohomoalanine[89].

Alternatively, DNA- protein conjugates can be prepared by creating a genetic fusion to the protein of interest (POI). For example, the SNAP-tag[90] (figure 1-10) and CLIP-tag[91] systems involve fusing a 20 kDa mutant of the DNA repair protein O6-alkylguanine-DNA alkyltransferase (or its engineered form for the CLIP tag system) to a POI. The fusion protein reacts specifically with a benzylguanine (for the SNAP tag) or benzylcytosine (CLIP tag) derivative in order to covalently link the two species of interest. Fusions can also be prepared using relaxase proteins which recognize their cognate ssDNA; such as the truncated form of the relaxase VirD2 protein (from *Agrobacterium tumefaciens*) which conjugates to unmodified DNA oligonucleotides[92]. Non-covalent approaches, as mentioned in the previous section, include use of biotin-(strept)avidin[73,93] interactions typically between a biotinylated oligonulecotide and (strept)avidin modified target protein. This interaction exhibits a particularly high affinity constant (K_d=40), which makes it suitable for many applications requiring a sufficiently long half-life.

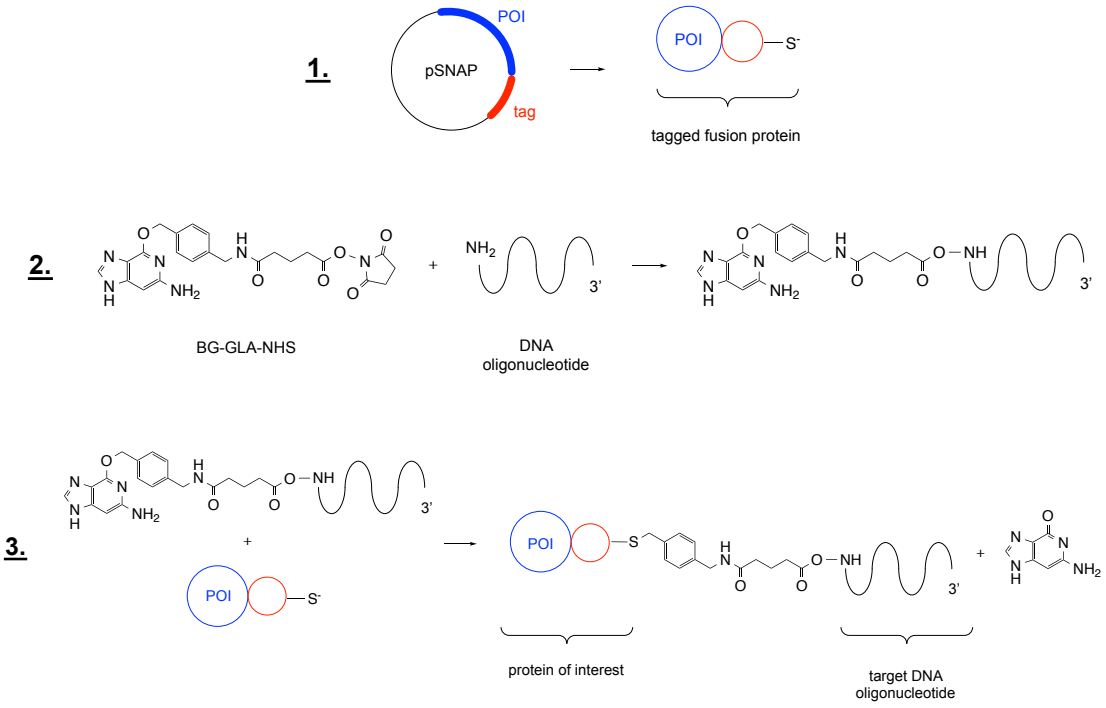

Figure 1-10 Generating DNA oligonucleotide-protein conjugates using the SNAP tag system. The SNAP tag system is a site specific labelling system which relies on the reactivity of a fusion protein (O6-alkylguanine-DNA-alkyltransferase) towards benzylguanine. **(1)** The SNAP tag is a 20 kDa mutant of the DNA repair protein, O6-alkylguanine-DNA-alkyltransferase (hAGT). The tag, depicted as a red sphere, is fused to a protein of interest (blue sphere). To generate the fusion protein, a sequence of interest is cloned adjacent to the tag within an expression vector. **(2)** A target DNA oligonucleotide is modified with a

benzylguanine moiety. Here, an amine modified DNA oligonucleotide is modified with BG-GA-NHS ester, in order to introduce the benzylguanine group. **(3)** The SNAP tag (fused to the protein of interest), covalently and irreversibly reacts with the benzylguanine (BG) derivative[90]. Other systems, such as the CLIP-tag[91] and HaloTag®[94] technologies, rely on a similar mechanism.

1.3 Enzyme immobilization

Enzyme immobilization describes the association of an enzyme to a solid support such that it is unable to freely diffuse. A key advantage of immobilization is that it allows the recovery of enzymes from reactants. Immobilization can take the form of covalent attachment of enzymes onto a surface (surface immobilization), physical entrapment within a compartment or a macromolecular network in which enzymes are confined in space[95], or through non-covalent adsorption onto a surface or object of interest through ionic, hydrophobic, affinity or bio specific based interactions[96] (figure 1-11).

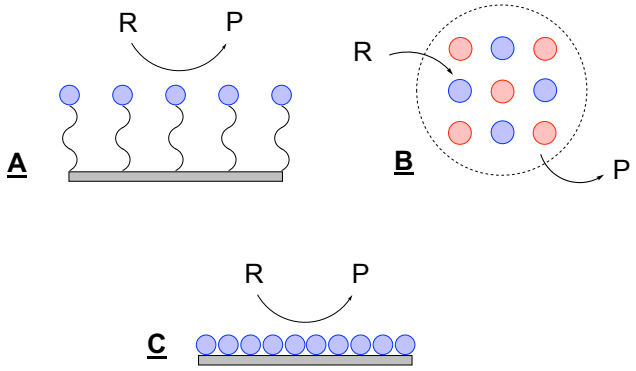

Figure 1-11 A schematic depiction of enzyme immobilization strategies. (A) immobilization of enzymes (depicted as spheres) on a solid support through covalent attachment or (B) entrapment or encapsulation of enzymes within a porous vesicle in which the reactants and products are able to freely diffuse. (C) non-covalent adsorption onto a surface. R = reactants, P = products.

Immobilization enables the use of enzymes in biotechnological or industrial settings, where it would be economically unfeasible if they had to be discarded. As well as their use as biocatalysts, immobilized enzymes find applications in a range of technologies, for example, in analytical devices such as biosensors, for controlled drug release, and as fundamental

compositions for solid-phase protein chemistry[96]. It is often reported that immobilization can improve enzyme stability, however, this is not always found[97]. Immobilization of enzymes affects their activity. Although improved activity has been reported, such as for enzymes immobilized on nanoparticles (NPs)[98], activity can be reduced due to decreased conformational flexibility, steric hindrance or restricted diffusion[98]. Other factors, such as interactions between an immobilized enzyme and its carrier or support can alter enzyme properties, such as their pH optimum, specific activity and selectivity[99].

1.4 Enzymes immobilized on DNA nanostructures - inspiration from nature

1.4.1 Enzyme cascades *in vivo*

Intracellularly, enzymatic reactions are compartmentalized or 'scaffolded' to spatially separate reactions from other metabolic processes in an otherwise complex and molecularly crowded environment[95,100,101]. For instance, many enzymatic reactions occur within multi enzyme complexes associated with biological membranes[101]. Another approach to the organization of cascades *in vivo* involves the encapsulation of enzymes belonging to a particular metabolic pathway within a protein shell, as demonstrated by bacterial microcompartments (BMCs)[102]. Figure 1-12 below depicts a carboxysome, a bacterial microcompartment for the fixation of CO_2. The effect of compartmentalization, in the case of carbon fixation, is to drive equilibrium in the direction of CO_2 and to protect metabolites from the intracellular environment. Electron micrographs, illustrating the principle of enzyme entrapment are also shown (figure 1-11, c).

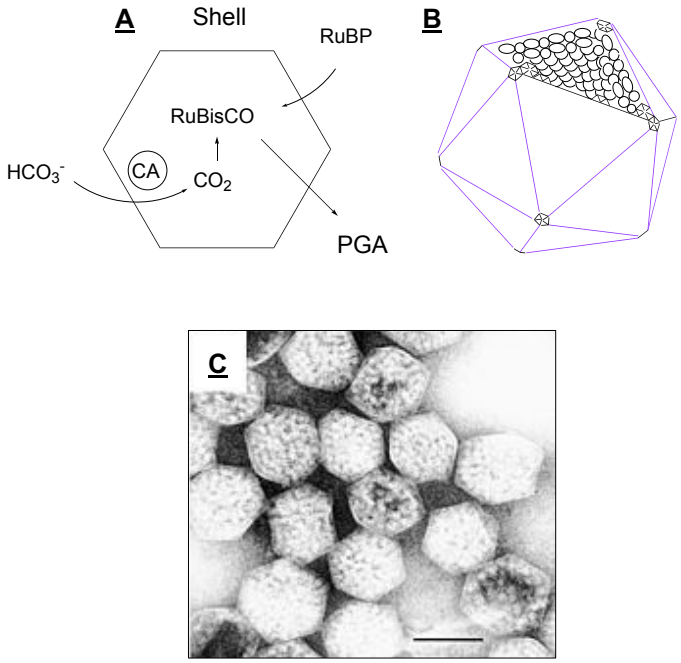

Figure 1-12 Enzyme entrapment - bacterial microcompartments. (A) A schematic representation of a carboxysome; a bacterial microcompartment encapsulating carbonic anhydrase (CA) and ribulose-1,5-bisphosphate carboxylase/oxygenase (RuBisCO) enzyme molecules, illustrating the process of CO_2 fixation[102]**. (B)** A representation of the structure of a carboxysome, featuring an icosahedral outer protein shell, composed of proteins belonging to the BMC protein family [103]. **(C)** A negatively stained electron micrograph of purified carboxysomes from *Halothiobacillus* neapolitanus, scale bar = 100nm. RuBisCO enzymes are discernible within the interior of the icosahedral structure, figure adapted with permission from ref. 104.

Another approach to the arrangement of multi enzyme systems or cascades is substrate channelling, where reactive intermediates are non-covalently transferred between separate catalytic sites without their dissociation to the bulk environment[105]. Substrate channelling can occur through a number of mechanisms, such as through intramolecular tunnels, electrostatic steering of intermediates between active sites, or through transport by flexible carrier proteins[106]. This process can occur between separate subunit domains in a multienzyme complex, or across separate domains on a single multifunctional enzyme. This phenomenon is observed in a number of bifunctional enzymes as a means of facilitating intermediates between separate catalytic sites. In the context of chemically dynamic and crowded intracellular environments, substrate channelling mechanisms serve an important purpose. Firstly, the transit time for intermediates between active sites is reduced, intermediates are chemically protected

from the external environment, and are sequestered themselves from competing metabolic reactions.

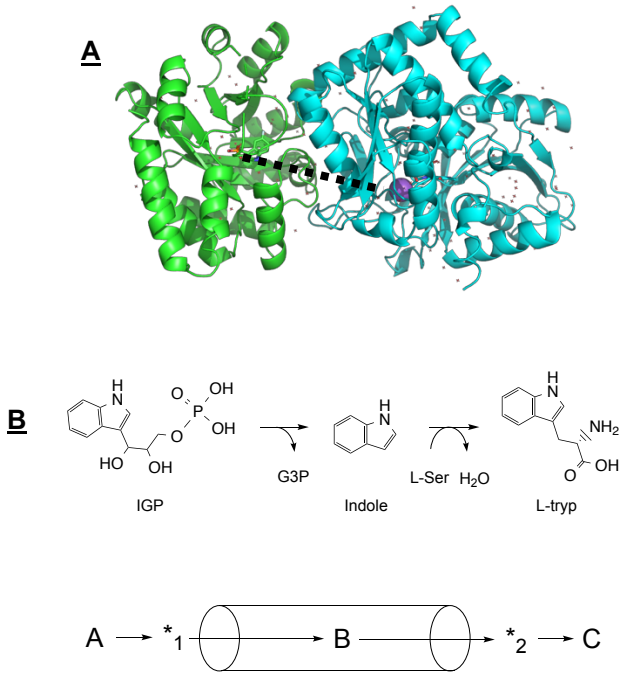

Figure 1-13 Substrate channelling through intramolecular tunnelling (A) The crystal structure of tryptophan synthase, depicting the alpha and beta subunits in blue and green respectively. The dashed line depicts the separation between the two active sites (PDB: 1A5S). The intermediate, indole, is channelled between active sites through an intramolecular tunnel located within the core of the dimeric protein. **(B)** The reaction scheme for the conversion of 3-glycerol-phosphate (IGP) to indole and glyceraldehdye-3-phosphate (G3P) (at the 1st active site), followed by the condensation of indole with serine to yield tryptophan (at the 2nd active site). **Below:** a schematic representation of the general mechanism of channelling by an intramolecular tunnel. *1, *2, denote separate active sites, B = intermediate.

Figure 1-13 depicts the process of substrate tunnelling through intramolecular tunnelling. The enzyme tryptophan synthase catalyses the two step conversion of indole 3-glycerol-phosphate and glyceraldehyde-3-phosphate to tryptophan[107]. The intermediate, indole, is channelled through a 2.5-3 nm hydrophobic intramolecular tunnel[108], which connects separate catalytic sites. Reactive intermediates can also be electrostatically channelled along a charged segment of a protein's surface. This occurs for enzyme dihydrofolate reductase-thymidylate synthase

(TS–DHFR), where a positively charged section of the protein surface supports the diffusion of the negatively charged cofactor, dihydrofolate, between active sites[109]. The malate dehydrogenase (MD)-citrate synthase (CS) bienzyme system also employs a substrate channelling mechanism through electrostatic guidance (figure 1-14), in order to guide the intermediate, oxaloacetate, from the MD and CS active sites. Dynamic assemblies, or 'swinging arms'[110] represent another approach to substrate channelling in nature, this mechanism is employed by the mammalian fatty acid synthase[111]. Here, covalently bound reaction intermediates are translocated between active sites within the multifunctional enzyme complex by a flexible acyl carrier protein or 'swinging arm', for the *de novo* synthesis of fatty acids[112].

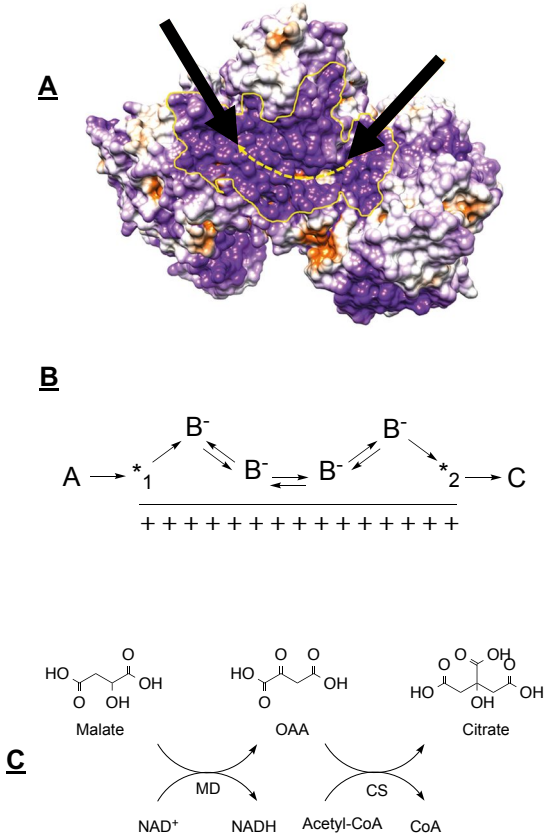

Figure 1-14 Substrate channelling through electrostatic guidance demonstrated by the malate dehydrogenase-citrate synthase bienzyme system. (A) The structure of the malate dehydrogenase (MD)-citrate synthase (CS) bienzyme system (PDB: mMDH:1MLD; CS: 1CTS). A positively charged region (indicated between the arrows) acts to steer the negatively charged intermediate, oxaloacetate, between MD and CS active sites. **(B)** A schematic representation of electrostatic guidance of the negatively charged intermediate B^- (oxaloacetate). **(C)** The reaction cascade depicting the conversion of malate to citrate by MD and CS. Adapted with permission from ref. 106, Macmillan Publishers Limited.

1.4.2 Spatial organisation of enzymes on DNA nanostructures

In vivo, metabolic pathways and multi enzyme systems coordinate numerous multistep reactions. Many pathways are highly organized, with respect to their cellular localisation and structural arrangement to facilitate efficient substrate transfer and product conversion[113]. The programmability of DNA as a nanoscale material, and its amenability to functionalisation through crosslinking strategies, makes it ideal for the display and control of enzyme cascades. A number of studies have reported the display of enzymes on DNA nanostructures, often with a view of replicating the forms of organization that appear in nature, or to improve reaction activity or turnover[113–127128]. The glucose oxidase - horseradish peroxidase bi-enzyme system (also known as the peroxidase-glucose oxidase (PGO) system) is commonly used as a model bi enzyme system for the display of enzymes on DNA structures, since it demonstrates Michaelis-Menten kinetics, and can be readily monitored through the reduction of a fluorogenic or colourimetric substrate.

A six fold enhancement in activity compared to the free enzyme pair[129] was reported for the GOx/HRP bi-enzyme pair arranged on DNA nanowires, (constituting repeated circular DNA-cocaine aptamer subunits). This was attributed to an increase in local concentration of the reactive intermediate H_2O_2 adjacent to HRP. A similar effect on the HRP/GOx cascade was observed on 'hexagonal' DNA scaffolds[130] (Figure 1-12). Where the oxidation of the substrate $ABTS^{2-}$ was found to be ~ 1.2-fold higher when arranged on a two-hexagon structure compared to a four hexagon arrangement (Figure 1-12). And on a DNA origami tile with reduced interenzyme spacing[123] (Figure 1-13), where an ~18 fold enhancement is reported for the enzyme pair spaced at a distance of 10nm compared to the equivalent unscaffolded enzymes. In both examples, it has been suggested these enhancements are due to the restricted diffusion of the intermediates due to reduced inter-enzyme spacing. A similar distance dependent enhancement is reported for other enzyme systems on DNA nanostructures, including the xylose reductase and xylitol dehydrogenase enzyme pair on DNA origami[124].

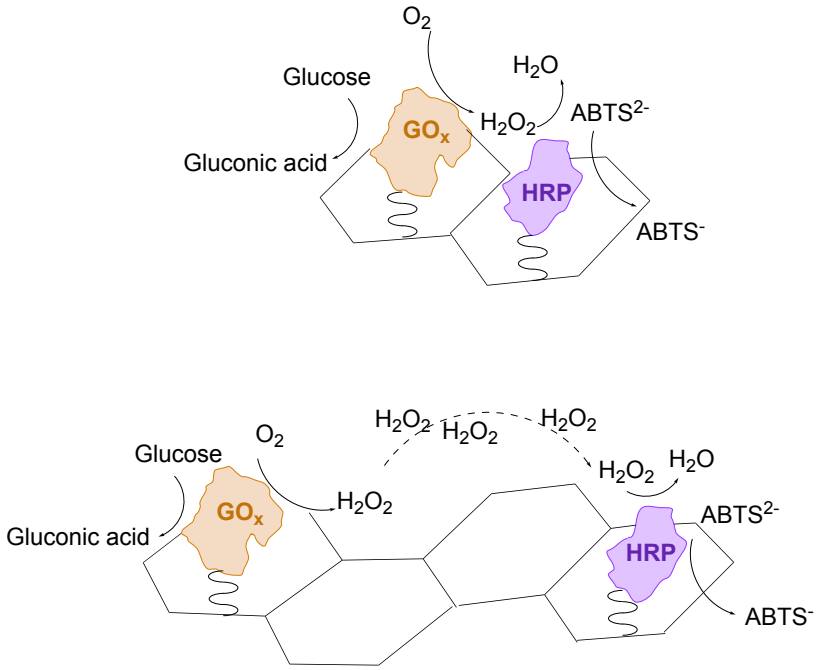

Figure 1-15 Glucose oxidase and Horseradish peroxidase enzymes topologically arranged on DNA hexagonal strip[130]**.** Reduced interenzyme spacing on the two hexagon structure is reported to improve reaction throughput[123].

As well as spatial separation of individual enzymes, it has also been reported that the geometric arrangement of an enzyme cascade can impart effects on its overall activity. This effect has been reported for a malic dehydrogenase- oxaloacetate decarboxylase-lactate dehydrogenase cascade[125], in which the rate of reaction was found to be positively affected by the geometric arrangement of the individual enzymes, in a triangular vs linear arrangement on a DNA nanostructure. The intermediate, NADH, is thought to be facilitated more efficiently between catalytic sites in the triangular arrangement, giving rise to a rate improvement of ~5 fold compared to the linear arrangement of enzymes. Enzymes may also be confined or entrapped within a DNA nanostructure. This has been demonstrated for a horseradish peroxidase and glucose oxidase enzyme pair, within a DNA nano cage, where an~8 fold enhancement in activity was observed compared to the equivalent free enzymes[115]. A similar effect is described for a modular nanoreactor composed of two three dimensional DNA origami tubes, to which individual enzymes, either HRP or GOx are tethered. A greater activity for the enzyme pair is observed when the origami tubes are brought together (bringing the enzymes within greater proximity to one another), compared to the unstructured tubes[131]. Similarly, it is thought that the confining DNA structures restricts diffusion of reaction intermediates, and that this results in the enhanced reaction rates observed for entrapped enzyme cascades.

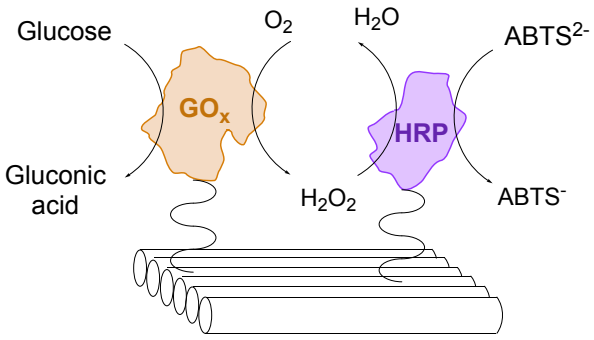

Figure 1-16 Glucose oxidase and Horseradish peroxidase enzymes immobilized on a DNA origami tile. Reduced interenzyme spacing on the DNA tile is reported to improve reaction throughput[123].

1.4.3 Modulating enzyme activity through DNA nanostructures

The activity of an enzyme system can be modulated through programmable or dynamic DNA structures, this usually involves the spatial separation of enzymes through the rearrangement of the DNA structure onto which they are immobilized. One example of a dynamic structure are DNA tweezers which control the spatial separation between two molecules on opposing arms of the structure. The regulation of an enzyme cascade immobilized on DNA tweezers has been demonstrated for a dehydrogenase and NAD^+ cofactor pair, attached to opposite arms of the tweezer[132]. Activation and inactivation of the catalysed reaction is achieved by spatially separating the enzyme cofactor pair between open and closed states. A similar tweezer structure is reported for the control of a GO/HRP enzyme pair, where closed and open states are reversibly regulated by the addition of 'fuel' and 'anti-fuel' strands[133]. Regulation of an enzymatic reaction can also be achieved by precluding an enzyme from solution, through the 'opening' and 'closing' of a DNA container in which that enzyme is encapsulated. This has been demonstrated for bovine alpha-chymotrypsin within a DNA nanovault, whose activity is regulated through the opening and closing of the 'vault' through a lock and key mechanism[113] (Figure 1-4). Regulation through a dynamic 'swinging' DNA arm has also been reported, (where cofactor NAD+ is immobilized on the 'arm') to facilitate hydride transfer between two dehydrogenases, glucose 6 phosphate dehydrogenase and malic dehydrogenase tethered on a DNA double-crossover (DX) tile scaffold[134] (Figure 1-5).

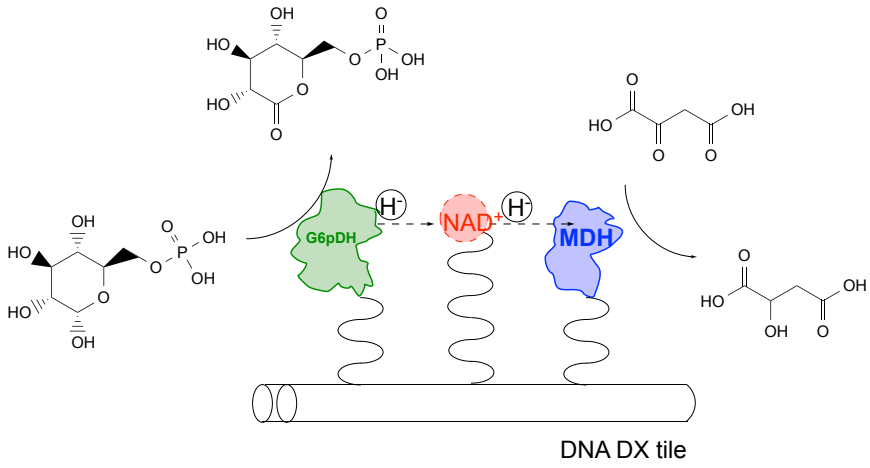

Figure 1-17 Enzymes arranged on DNA nanostructures. Glucose oxidase and Horseradish peroxidase enzymes immobilized on a DNA origami tile. Immobilized NAD+, on a 'swinging arm' facilitates hydride transfer between two dehydrogenases tethered to a DX DNA tile (Glucose-6-phosphate dehydrogenase and malate dehydrogenase)[134].

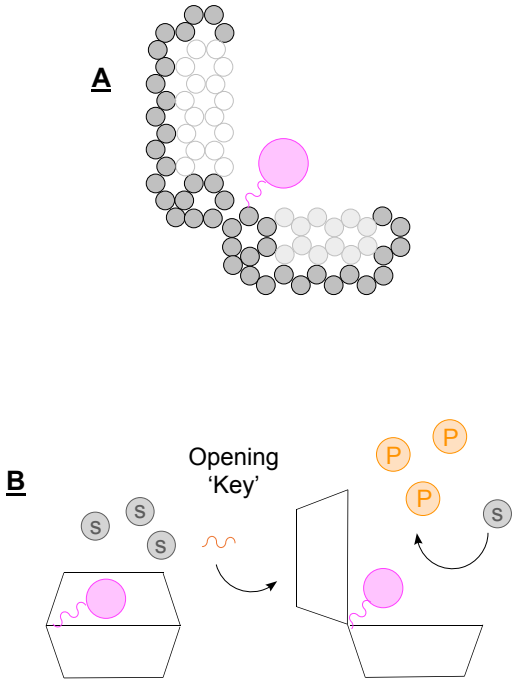

Figure 1-18 Control of enzymatic reactions with DNA nanostructures. 'Control of enzyme reactions by a reconfigurable DNA nanovault' from Ref [113]. (A) Cross section of the three-dimensional structural design of the DNA Vault. Bovine alpha-chymotrypsin (depicted

as a pink sphere) is encapsulated within the 'vault' whose opening is regulated by a DNA 'key' (B).

1.4.4 The basis for rate enhancements of enzyme cascades on DNA scaffolds

The basis of enhanced reaction rates for enzyme cascades arranged on DNA nanostructures, is often attributed to the spatial proximity of enzymes, which is thought to result in 'substrate channelling' or the enhanced diffusion of intermediates between enzyme active sites. In certain cases, this could be facilitated by the negative charge of the DNA structure on which the enzymes are scaffolded. For example, interactions between substrates and/or intermediates with the DNA scaffold could increase their effective local concentration, or facilitate their guidance between active sites[135,136]. However, the mechanisms underlying the observed rate enhancements for immobilized enzyme cascades on DNA nanostructures remain unclear[137,138]. Moreover, reported activity enhancements vary considerably[137], despite the use of similar display strategies and DNA-enzyme coupling techniques. For example, a 15-fold enhancement in reaction rate was observed for the GOx–HRP enzyme pair separated by a distance of 10nm on a DNA origami tile[123]; whilst the same enzyme same pair only yields a 1.5-fold enhancement when positioned in closer proximity on a DNA structure described elsewhere[133].

Other explanations have been proposed to account for the observed improvements in enzyme activity on DNA scaffolds. For instance, it has been suggested that the negative charge of DNA structures impart a stabilizing effect on immobilized enzymes[115]. Elsewhere, it has been suggested that DNA scaffolding affects the activity of immobilized enzymes in a way that is analogous to the Sabatier principle[135] - a qualitative concept that states that the interaction between a catalyst and substrate should be neither too strong/nor weak in order to achieve highest catalytic activity. In the case of DNA-enzyme structures, substrates bind the structure, not a catalyst. Here[135], it was observed that intermediately bound substrates improved the activity of the horseradish peroxidase (HRP) enzyme associated with a DNA scaffold. Alternatively, it has been suggested that other effects, imparted by the DNA structures on which enzymes are displayed, can account for the reported improvements in reaction rates[137,138]. For example it has been suggested that changes to the local pH at the DNA-solution interface favours the pH optimum of HRP, and that this results in the improvements in reaction rate reported for HRP/GOx cascades (a lowered local pH is imparted by the negative charge of the DNA structure)[106,139,140].

1.5 Aims of thesis

The aim of this thesis is to investigate the application of a DNA-enzyme nanostructures for functional applications. In the context of other DNA-enzyme nanostructures described in the literature, all have entirely focused on the spatial arrangement of enzyme cascades positioned discretely within the nm range. However, there are limitations associated with these forms of arrangements, particularly for functional or biotechnological applications. Here, we will specifically investigate the 'sequestration' of an enzyme cascade directed by a concatemer ssDNA synthesized by phi29 rolling circle amplification. This approach differs from existing work in the literature, in that it attempts to achieve a concentrated or 'agglomerate' arrangement of multiple enzymes of interest supported by a DNA structure. Initially a model bi-enzyme system, the horseradish peroxidase and glucose oxidase enzyme pair, will be investigated. To further probe the effect of the NB structure on immobilized enzyme cascades, and to assess the applicability of this system to a biotechnologically relevant enzyme system, a transaminase and norcoclaurine synthase enzyme pair will be immobilized on DNA nanoballs. This bi-enzyme system will be used for the synthesis of biotechnologically relevant benzylisoquinoline (BIAs) precursors.

In the second part of this thesis, enzymatic catalysis will be investigated as a mechanism to affect the motion of a DNA nanostructure. It has been demonstrated that a number of enzymes display enhanced diffusive motion in the presence of their substrate[141–146], and that enzymatic catalysis can affect the motion of nano and microscale structures to which they are attached[144,145,147]. Although the exact mechanism underlying this effect is unclear[148], enzymatic catalysis may represent an alternative approach to achieving directed motion of self-assembled DNA structures. In chapter 6, lysine decarboxylase, catalysing the decarboxylation of L-lysine to cadaverine and CO_2, was tethered to a DNA structure to affect its diffusive motion on the addition of the substrate, the 'fuel'. While there are examples of DNA devices which demonstrate directed motion on the nanoscale (such as DNA based 'walkers' on predefined DNA or RNA tracks), to the best of our knowledge, the use of enzymatic catalysis to affect the motion of a DNA nanostructure has not been described previously.

Chapter 2

Materials and methods

2.1 List of materials

LB Broth (Miller) Powder microbial growth medium, LB Broth with agar (Lennox), 2xYT Medium, Acrylamide-bis ready-to-use solution 40% (29.1:0.9), N,N,N′,N′-Tetramethylethylenediamine (TEMED), Tris base, HEPES, Magnesium chloride, Sodium chloride, Glycerol, Calcium chloride, Imidazole, Dopamine hydrochloride, Sodium pyruvate, 2,2′-Azino-bis(3-ethylbenzothiazoline-6-sulfonic acid) diammonium salt (ABTS), Peroxidase from horseradish (Type VI) lyophilized powder, Glucose Oxidase from Aspergillus niger (Type X-S) lyophilized powder, SIGMAFAST™ Protease Inhibitor Cocktail Tablets EDTA-Free, were obtained from Sigma Aldrich.

3-Hydroxyphenethylamine hydrochloride was obtained from Santa Cruz Biotechnology.

UltraPure™ TBE Buffer, 10X (Invitrogen™), UltraPure™ Agarose (Invitrogen™), Sulfo-SMCC (sulfosuccinimidyl 4-(N-maleimidomethyl)cyclohexane-1-carboxylate) crosslinker, DTT (dithiothreitol) and BupH™ Phosphate Buffered Saline Packs, S.O.C. Medium, UltraPure™ 0.5M EDTA, pH 8.0 and Acclaim™ 120 C18 Column were purchased from Thermo Fisher Scientific.

12% Mini-PROTEAN® TGX™ Precast Protein Gels and 10x Tris/Glycine/SDS running buffer were obtained from Bio-Rad Laboratories.

phi29 DNA Polymerase and reaction buffer, Prestained Colour Protein Standard Broad Range (11–245 kDa), Blue Gel Loading Dye(6X), Blue Loading Buffer Pack, T4 DNA Ligase, Quick-Load® 1 kb DNA Ladder and Deoxynucleotide (dNTP) Solution Set were from New England BioLabs.

RESOURCE Q anion exchange chromatography column, HisTrap FF, PD MidiTrap G-25 and illustra NAP Columns were obtained from GE healthcare life sciences. Vivaspin® 500 Centrifugal Concentrators and Vivacon® 500 ultrafiltration spin columns were obtained from Sartorious Stedim Biotech.

BugBuster® 10X Protein Extraction Reagent was purchased from Merck Millipore. InstantBlue™ Coomassie stain was from expedeon. DNA Clean & Concentrator™-5 and ZymocleanTM Gel DNA Recovery Kit was procured from Zymo Research.

Custom DNA oligonucleotides were purchased from Sigma Aldrich, MWG operon or Integrated DNA technologies. Typically, oligonucleotides were purchased on a 0.1μg synthesis scale with standard desalting, or with HPLC purification for chemically (i.e thiol) or fluorophore modified oligonucleotides. All DNA ultramers were purchased from Integrated DNA technologies at a 0.5 nmol synthesis scale with PAGE purification.

2.1.1 List of plasmids/phagemids

Name of plasmid/phagemid	Origin/ Manufacturer	Ref	Purpose	Map
pBluescript II SK (-)	Agilent	GenBank: X52330.1	Cloning vector (phagemid) for the rescue of sense strand ssDNA.	Appendix B.2
pET29a(+)-deC_ 87095	-	-	Plasmid for the expression of lysine decarboxylase (gene: deC_87095)	B.3
pET29a-CV_2025	*Chromobacterium violaceum*	[149]	Plasmid for the expression of CV2025 transaminase (TAm)	A.6
pJ411-Δ29TfNCS	*Thalictrum flavum*	[150], [151]	Plasmid for the expression of Δ29TfNCS norcoclaurine synthase.	n/a*

Table 2-1 List of plasmids/phagemids used. *pJ411-Δ29TfNCS was commercially prepared by DNA2.0. The plasmid map is unavailable as the pJ411 vector (DNA2.0) is proprietary.

2.1.2 List of bacterial and bacteriophage strains

Strain	Ref	Genotype	Resistance	Purpose
***E. coli* BL21 (DE3)**	[152]	*F– ompT hsdSB (rB–, mB–) gal dcm (DE3)*	-	For the recombinant expression of Lysine decarboxylase (deC_87095), Δ29TfNCS norcoclaurine synthase (NCS) and CV2025 transaminase (TAm) enzymes.
***E. coli* XL1-Blue MRF'**	Agilent	*Δ(mcrA)183 Δ(mcrCB-hsdSMR-mrr)173 endA1 supE44 thi-1 recA1 gyrA96 relA1 lac [F´ proAB lacIqZΔM15 Tn10 (Tetr)]*	Tetracycline	For the transformation and propagation of phagemid pBluescript II SK (-).
Helper phage VCM13	Agilent	-	-	For the rescue of ssDNA pBluescript II SK (-) from phagemid transformed *E. coli* XL1-Blue MRF'.

Table 2-2 List of bacterial/bacteriophage strains used.

2.2 Preparation of DNA nanostructures

2.2.1 Preparation and storage of DNA oligonucleotides

All DNA oligonucleotides were re-suspended in Milli-Q grade water to a final concentration of 100μM based on the manufacturers given synthesis amount, all solutions were stored at -20°C.

2.2.2 Annealing of DNA nanostructures

For the structures described in chapters 5: The annealed starting template structure was formed by annealing staple oligonucleotides to the pBluescript SK (-) ssDNA template. The annealing mixture, containing 5x excess complementary oligonucleotide to pBluescript ssDNA template, was prepared with a final concentration of 0.2μM scaffold ssDNA and 1μM DNA oligonucleotides, with 12mM $MgCl_2$, 1 X TBE (Tris-Borate-EDTA) by heating to 95°C for 5 minutes in a thermal heat block (Eppendorf ThermoMixer® C with a max cooling rate of 2.5 °C/min) and cooling to room temperature (23°C). For the structures described in chapter 6:

Purified DNA oligonucleotides were combined at a final concentration of 1μM each in a volume of 100μL with 12mM $MgCl_2$, Tris-HCL pH 7.5. Samples were annealed over a cooling ramp from 95°C to 25°C over a total of 8 or 24 hours using a Bio-Rad C1000 Touch™ Thermal Cycler (with an average temperature ramp of 3.3°C/sec). Annealed samples were stored at 4°C for further use.

2.2.3 Hybridization of DNA oligonucleotide-enzyme conjugates and fluorescent oligonucleotides to DNA structures

DNA Oligonucleotide-enzyme conjugates were hybridized to target DNA structures by incubating conjugates to target DNA structures in 10-fold molar excess, in 1X TBE, 10mM $MgCl_2$, at 37°C in a thermal heat block (Eppendorf ThermoMixer® C) for 1 hour. Excess or unhybridized DNA oligonucleotides were removed by ultracentrifugation using a Sartorious Vivacon® 500 centrifugal spin filter, with a 100 kDa or 125 kDa molecular weight cut off, centrifugation was performed at 3000 x g at room temperature for 15-30 minutes.

2.3 Gel electrophoresis

2.3.1 Agarose gel electrophoresis

Agarose gels were prepared at a final percentage of 1 or 2%, with 1X TBE (Tris-borate-EDTA) and EtBr at a final concentration of 0.5μg/ml. Samples were combined with 6X blue gel loading dye and electrophoresed with 1X TBE running buffer at constant voltage, 100V, typically for 45 minutes to 1 hour. Gels were visualised by UV trans illumination and acquired using a protein simple alphaimager(r) mini. For fluorescence analysis, agarose gels were prepared without the addition of EtBr and were visualised/imaged using an Amersham imager 600RGB scanner (GE healthcare).

2.3.2 Denaturing Tris-glycine-SDS polyacrylamide gel electrophoresis (denaturing PAGE)

Denaturing polyacrylamide gel electrophoresis was preformed using BioRad 12% Mini-PROTEAN® TGX™ Precast Gels. Samples were prepared with addition of 3X NEB blue SDS gel loading buffer and were electrophoresed with 1X Tris/Glycine/SDS running buffer at constant voltage, 200V. Gels were stained using instantblue™ ultrafast protein stain for approximately 30 minutes then rinsed in deionized water. Staining was visualized using a white light conversion screen with a protein simple alpha imager system. For fluorescence analysis,

unstained gels were rinsed in Milli-Q grade water before imaging using an Amersham imager 600RGB scanner by epi light illumination (emission filters: Cy2: 525BP20, Cy3/EtBr: 605BP40, Cy5: 705BP40).

2.3.3 Non-denaturing polyacrylamide gel electrophoresis

Non-denaturing polyacrylamide gel electrophoresis was preformed using 10% Acrylamide:bisacrylamide (29:1), 1X TBE gels. Samples were prepared with 6X blue gel loading dye and gels were electrophoresed with 1 X TBE running buffer at 150V constant. Gels were stained with stains all solution (0.005% (w/v) Stains-All, 10% (v/v) formamide, 25% (v/v) isopropanol, 15 mM Tris-HCl, pH 8.0, 65% (v/v) H_2O), under darkness for 30 minutes - 1 hour. gels were washed with 1 X TBE buffer and visualised/de-stained by using a white light conversion screen with a protein simple alpha imager system.

2.4 DNA polymerase based methods for the formation of DNA nanostructures

2.4.1 Preparation of DNA nanoballs by phi29 DNA polymerase rolling circle amplification (RCA)

Preparation of the circularized ssDNA template: The ssDNA starting template was prepared by first annealing the 200-mer template to a bridge oligonucleotide in a final molar ratio of 1:2 in a total volume of 50µL final concentration of ssDNA 25µM, 50µM bridge oligonucleotde, 1X T4 DNA ligase buffer (50 mM Tris-HCl, 10 mM $MgCl_2$, 1 mM ATP, 10 mM DTT, pH 7.5). The annealing mixture was heated to 95°C for five minutes then cooled to room temperature (23°C) in a heat block (Eppendorf ThermoMixer® C with a max cooling rate of 2.5 °C/min). To ligate the annealed circularized ssDNA template, 5µL T4 DNA ligase (400,000 units/ml) was added to the annealed mixture and incubated at room temperature for 1 hour. The ligated circularised ssDNA product was purified by centrifugal spin column purification using a Zymo DNA Clean & Concentrator™-5, according to the manufacturer's instructions. The sample eluted in 20µL milli-Q water.

phi29 rolling circle amplification: Rolling circle amplification was preformed using approximately 0.5-1µM purified/ligated starting 200-mer template (concentration determined by absorbance at 260nm) in a final volume of 250µL, 1X phi29 reaction buffer (50 mM Tris-HCl, 10 mM $MgCl_2$, 10 mM $(NH4)_2SO_4$, 4 mM DTT, pH 7.5), 1mM dNTP mix, 20U phi29 polymerase (10,000 units/ml). The amplification reaction was incubated at 30°C for 1 hour in a thermal heat block. Reactions were quenched with EDTA added to a final concentration of

10mM. For time course analysis of RCA reaction products, aliquots were taken at time intervals between 1-3 hours and combined with 6 X gel loading buffer for analysis by agarose gel electrophoresis.

Amplified DNA structures were purified using Takara biotech QuickClean™ Enzyme Removal resin to remove excess phi29 DNA polymerase. The purification procedure was performed as follows: to the amplified EDTA quenched reaction mixture, 1/10th volume of quickclean enzyme removal mixture was added (resuspended prior to use), and gently mixed by pipetting. The resin was removed by centrifugation at 13, 000 rpm for 30 seconds and collected from the solution using a wide bore pipette tip. The purification procedure was repeated 2X by adding and recovering the purification resin as described. Purified RCA reaction products were stored at 4°C.

2.5 Cell culture

2.5.1 General cell culturing methods (*E. coli*)

Small scale overnight cultures were prepared by inoculating 10mL LB media or 2 X YT media, supplemented with appropriate antibiotics (working concentrations given in table 2-3), with a single bacterial colony from a freshly streaked plate. Cultures were incubated at 37°C with agitation at 300 RPM, for approximately 16 hours. For isolation of single bacterial colonies, an inoculation loop was used to scrape icicles from glycerol stock and was used to streak an LB agar plate supplemented with appropriate antibiotic. For the preparation of glycerol stocks, typically 2ml mid-log culture or 1 ml of a freshly saturated culture was added to 1ml 100% glycerol, which was aliquoted and stored at -80°C.

Antibiotic	Working concentration (µg/mL)
Ampicillin	100
Tetracycline	10
Chloramphenicol	25
Kanamycin	25

Table 2-3 Antibiotic working concentrations used for cell culture.

2.5.2 Preparation of chemically competent *E. coli*

Chemically competent *E. coli* was prepared by inoculating 10ml LB media with a single *E. coli* colony from a pre-streaked plate. The culture was incubated at 37°C with agitation for 16 hours. From the overnight culture, a 1% culture in 25mL LB media was prepared and incubated at 37°C until an OD_{600nm} ~ 0.4 was reached. Cells were recovered by centrifugation at 3000 rpm at 4°C for 15 minutes, and the pellet was re-suspended in 10mL ice cold 100mM $MgCl_2$. The cell suspension was centrifuged at 16000 x g at 4°C. The supernatant was removed and 1.25mL 100mM $CaCl_2$ was added to the cell pellet which was incubated on ice for 1.5 hours. 200µl of 50% glycerol was added to the solution and 150µL aliquots were prepared on dry ice. Competent cell stocks were stored at -80°C.

2.5.3 Transformation of chemically competent *E. coli*

Approximately 1 pg-100 ng of plasmid/phagemid DNA, in a total volume <10µl, was added to a 150µl aliquot of chemically competent *E. coli* and incubated on ice for 30 minutes. The sample was heat shocked by incubation at 42°C for 30 seconds, followed by addition of 850µL S.O.C media. The mixture was incubated with agitation at 37°C for 1 hour. Typically, 100µl of sample was spread onto a LB agar plate supplemented with appropriate antibiotic using a cell spreader. Plates were incubated at 37°C for 16 hours.

2.5.4 Recovery of single stranded pBluescript II SK (–) Phagemid ssDNA from transformed cells

Prior to infection of phagemid transformed *E. coli*, the titre of VCM13 helper phage was determined. A culture of *E. coli* XL1-Blue MRF' was prepared by inoculating 10mL LB media with a single colony from a freshly streaked plate. The cultures were incubated at 37°C until an OD_{600nm} ~ 0.8 was reached. A 10-fold serial dilution of the VCM13 helper phage stock was prepared by diluting 100µl successively in 0.9ml LB media. For each dilution, 100µl of the diluted stock was combined with 3ml of top agar (0.7g agar per 100 ml of LB Broth), 40µl of 20mg/ml X-Gal and 4µl isopropyl β-D-1-thiogalactopyranoside (IPTG) 20% solution. Top agar preparations were immediately mixed and poured onto LB agar (unsupplemented) plates and evenly distributed. Plates were incubated at 37°C for 16 hours. The tire of the stock solution was determined based on a count of the plaque forming units (pfu).

Infection of phagemid transformed *E. coli* culture for the isolation of pBluescript II SK (-): First, chemically competent *E. coli* XL1-Blue MRF' was prepared and transformed with phagemid pBluescript II SK (-) as described under the cell culturing methods section. A single *E. coli* XL1-Blue MRF' colony (transformed with pBluescript II SK (-) phagemid) was used to inoculate 5ml 2 X YT, supplemented with ampicillin at a final concentration of 100µg/mL and VCM13 helper phage at a final pfu (plaque forming unit) of approximately 10^7 pfu/ml. After 2 hours, the culture was supplemented with kanamycin at a final concentration of 70µg/mL and was incubated at 37°C for a further 14 hours (total incubation time was 16 hours). 1.5ml of the infected overnight culture was centrifuged at 16000 x g for 2 minutes, 1ml of the supernatant was removed and added to 150µl 20% PEG8000, 2.5M NaCl. The solution was incubated on ice for 30 minutes to precipitate phage particles.

The culture was centrifuged at 4°C for 30mins, the supernatant was discarded and 400µL 0.3M NaOAC, 1mM EDTA was added to the pellet. 400µL Phenol:Chloroform:Isoamyl Alcohol (25:24:1, v/v) was added to the solution and mixed by inversion. The solution was centrifuged at 13000 rpm for 5 minutes to separate the phases. The aqueous phase was removed and added to 1ml of 100% ethanol. The samples were incubated at -20°C for approximately 3 hours. The ssDNA was precipitated by centrifugation at 4°C at 16000 x g for 10 minutes. Ethanol was removed and the pellet was dried and resuspended in 50µl TE buffer pH 7.5.

Purification of the ssDNA by agarose gel electrophoresis: The extracted ssDNA was analysed by agarose gel electrophoresis on a 1% agarose gel with EtBr. To remove unwanted phage ssDNA genome (co-packaged in addition to the phagemid derived ssDNA), the band corresponding to pBlusecript SK II (-) was excised and purified using a ZymocleanTM Gel DNA Recovery Kit according to the manufactures protocol. The purified ssDNA was eluted in 20µL milli-q water and stored at 4°C.

2.6 Expression and purification of histidine tagged proteins

Histidine tagged proteins were expressed and purified as follows. Using a 10 ml overnight culture a 2% 500 ml 2 X YT culture were prepared and incubated at 37°C. Once an OD_{600nm} ~ 0.7-0.8 was reached, the cultures were induced by adding 500µl 0.1M IPTG. The cultures were incubated for a further 3 hours at 37°C with agitation. The cell pellet was recovered by centrifugation at 1200 x g for 10 mins at 4°C, and then frozen at -80°C overnight (for approximately 16 hours). To the thawed pellet, binding buffer (50 mM Tris-HCl, 300mM NaCl, 30 mM imidazole, pH 7.5) and was added at final volume of 4ml/g cell pellet and crushed

SIGMAFAST™ protease inhibitor cocktail tablet, EDTA-Free (added at final concentration of 1 tablet per 100ml). SIGMAFAST™ protease inhibitor cocktail tablet contains: 4-(2-Aminoethyl)benzenesulfonyl fluoride hydrochloride (AEBSF), Bestatin hydrochloride, Leupeptin, E-64, Aprotinin, Pepstatin A, and Phosphoramidon disodium salt.

BugBuster® 10X Protein Extraction Reagent was added to the resuspended cell pellet to a final concentration of 1X. DNAse I powder was added to the resuspended cultures to reduce the viscosity of the lysate. The cell suspension was incubated at room temperature on a rotary mixer for 20 minutes. Cell debris was removed by centrifugation at 16,000 x g for 20 minutes at 4°C. The supernatant was removed and filtered using a 0.2µm syringe filter before loading onto a purification column. Histidine tagged proteins were purified by immobilized metal affinity chromatography (IMAC).

Histidine tagged proteins were purified using a His GraviTrap prepacked gravity-flow column (bed volume: 1ml, GE healthcare). The column was pre-equilibrated with 10ml binding buffer (50 mM Tris-HCl, 300 Mm NaCl, 30 mM imidazole, pH 7.5). Samples were added in a volume no more than 15ml and the column was washed with 10ml binding buffer. To elute the histidine tagged protein, 3ml elution buffer (50 mM Tris-HCl, 300 Mm NaCl, 500 mM imidazole, pH 7.5) was added to the column. The eluted fraction was collected, and buffer exchanged using a 5mL PD MidiTrap G-25 (GE healthcare). For long term storage, aliquots were prepared added to an equal volume of glycerol and stored at -20°C.

2.7 Bioconjugate techniques

2.7.1 Conjugation of enzymes to DNA oligonucleotides using heterobifunctional cross linker sulfo-SMCC

Sulfo-SMCC (sulfosuccinimidyl 4-(N-maleimidomethyl)cyclohexane-1-carboxylate) was reconstituted in milli-q water at a final concentration of 10mg/ml. For the conjugation of horseradish peroxidase and glucose oxidase, described in chapter 3, enzymes were resuspended to 10mg/ml in conjugation buffer (BupH™ Phosphate Buffered Saline Packs, 0.1M sodium phosphate, 0.15M NaCl, pH 7.2). For recombinantly expressed enzymes, transaminase and norcoclaurine synthase (chapter 5) and lysine decarboxylase (chapter 6), purified enzymes were buffer exchanged into conjugation buffer using vivaspin 500 centrifugal spin filters with a 3K molecular weight cut off (usually exchanging buffer X 3) and adjusted to a final concentration of 10mg/ml based on their theoretical extinction coefficient. Enzymes were activated with 5 X molar excess sulfo-SMCC in conjugation buffer. The activation reaction was incubated at room

temperature for 30 minutes. Excess crosslinker was removed from the enzyme solution using a 5mL PD G25 minitrap gravity-flow gel filtration column pre-equilibrated with conjugation buffer.

Thiol modified oligonucleotides (100μM stock solution in milli-q water) were reduced using DTT (1,4-dithiothreitol) at a final concentration of 0.1M in conjugation buffer, at room temperature for 1 hour. DTT was removed from the reduced oligonucleotides using an illustra NAP-5 gravity-flow column (5mL prepacked with Sephadex™ G-25 DNA grade gel), pre-equilibrated with conjugation buffer, according to the manufacturers protocol (GE healthcare). The SMCC activated enzyme and reduced oligonucleotide were combined at a final molar ratio of 1:1 and incubated for a further 30 minutes at room temperature. The crosslinking reaction products were analysed by polyacrylamide gel electrophoresis to determine the extent of the crosslinking.

For storage, conjugates were buffer exchanged using a 5mL PD MidiTrap G-25 gravity gel filtration column, and then stored at 4°C for short term storage. For long term storage, conjugates were stored with glycerol at a final concentration of 50% and frozen at -20°C.

2.8 Chromatographic techniques

2.8.1 Purification of DNA-enzyme conjugates by anion exchange chromatography (AEC)

Anion exchange chromatography was preformed using an AKTA explorer FPLC system equipped with a frac-950 fraction collector and Resource Q strong anion exchanger column, prepacked with Source 15Q (GE healthcare). Conjugation reaction products were desalted in starting buffer A (20mM Tris, pH 7.5) using an amicon vivaspin centrifugal column or PD midi trap gel filtration column, samples were typically loaded in 0.5-1mL volumes. All analysis was preformed using a flow rate of 1ml/min at room temperature. Products were eluted using a gradient of elution buffer B (20mM Tris, 1M NaCl, pH 7.5) from 0 to 90% over 45 minutes. Fractions were collected in 0.2ml volume and desalted using illustra NAP-5 columns (5mL prepacked with Sephadex™ G-25 DNA grade gel, GE healthcare). The identity and purity of fractions were assessed by denaturing polyacrylamide gel electrophoresis.

2.8.2 Purification of DNA-enzyme conjugates by centrifugal spin filtration

For conjugation reactions purified using centrifugal filters (sartorious® 500 µl viva spin MWCO filters) samples were made up to a volume of 500µL with BupH™ phosphate buffered saline (0.1M sodium phosphate, 0.15M NaCl, pH 7.2) and centrifuged at 15,000 x g in a bench top centrifuge at 4°C for 15 minutes. Typically, 3-5 washes with BupH™ phosphate buffered saline was preformed, each time adjusting the concentrated sample to 500 µl.

2.9 Biophysical techniques

2.9.1 UV/VIS spectrometry (melt curve analysis)

UV/VIS spectroscopy was preformed using a Varian 100 Bio UV-VIS spectrophotometer equipped with a Peltier temperature-controlled cuvette holder. Measurements were conducted using a quartz UV/VIS cuvette with a path length of 1cm. For melting temperature profile curves, samples were prepared in a total volume of 500µL, and heated from 25 to 95°C, absorbance was monitored at 260 nm.

2.9.2 Atomic force microscopy (AFM)

Atomic force microscopy was performed using a Bruker Multimode 8 scanning probe microscope equipped with an E/J scanner PeakForce Tapping™ with ScanAsyst. Data was obtained using the Bruker Nanoscope software. Typically, 5µL-10µL sample was combined with 45µL 5 mM $NiCl_2$ and deposited onto a cleaved mica disc (cleaved using a scalpel) which was mounted on a specimen plate (Agar scientific). All analyses were performed at room temperature. Bruker MSNL Silicon Nitride cantilever F cantilevers were used for all analyses.

SPM data was analysed using Gwyddion scanning probe microscopy (SPM) analysis software[153]. Data were flattened, and horizontal scarring was removed, no further manipulation of the original data was made. For the analysis of particles, grains were selected using the thresholding function, and the selection was further refined to exclude outliers using the Remove Edge-Touching function. For grain property distributions, the maximum value (height) occurring inside the grain and the minimum circumcircle radius, the radius of minimum circle that contains the grain were obtained.

2.9.3 Dynamic light scattering (DLS)

Dynamic light scattering was preformed using a Malvern Zetasizer Nano ZS. All measurements were performed in a 0.5ml polystyrene cuvette with a path length of 1cm. For the sizing of DNA nanoball structures described in chapter 4, measurements were performed at 25°C in 0.1 M HEPES 5 mM $MgCl_2$ pH 7.5. For sizing and determination of the diffusion coefficient described in chapter 6, all analysis was performed in 0.1 M HEPES 5 mM $MgCl_2$ pH 7.5 (pre-filtered using a 0.22μm syringe filter) at 37°C, L-lysine was added to a final concentration of 1mM-10mM. All samples analysed by DLS were pre-equilibrated at the target temperature for 60 s before measurements were made. The temperature was maintained by the integrated heater. Measurements were repeated three times and averaged using the zetasizer software averaging function.

2.9.4 Nanoparticle tracking analysis (NTA)

Nanoparticle tracking analysis was preformed using a Malvern NanoSight NS300 NTA analyser equipped with a blue 488nm Blue Laser Module, sCMOS camera, integrated temperature control and Nanoparticle Tracking Analysis (NTA) software suite. Analysis was performed in 0.1 M HEPES 5 mM $MgCl_2$ pH 7.5 pre-filtered using a 0.22μm syringe filter, the DNA structure was buffer exchanged prior to analysis. Samples were diluted such that approximately 30-40 particles were visible in a single view. 500μl of sample was loaded into the viewing chamber using a 1ml plastic syringe. Prior to analysis, a blank sample (buffer only) was analysed to confirm the absence of particulates. To investigate the effect of L-lysine on the diffusive motion of structures: L-lysine was added at a final concentration of 1 5, or 10mM or in the absence of L-lysine. NTA analysis was performed at 37°C; this temperature was maintained using the integrated heater/temperature control function.

Video tracking of particles was captured for 60 seconds and repeated 6 times for each condition. Typically, tracks for 800-1000 individual particles were obtained. Particles deemed false by the tracking software were excluded from subsequent analyses. The capture settings and video analysis parameters used are given in the tables 2-3 and 2-4 respectively. Data analysis: Mean square displacement analysis of particle trajectories was preformed using the @msdanalyzer MATLAB per-value class to analyse particle trajectory data[154]. Calculation of the ensemble mean averaged all MSD curves and standard deviation of the mean for MSD curves were also obtained using this MATLAB class. Diffusion coefficients, measured for individual particles, were determined by the NTA analysis software and analysed using graphpad Prism using the frequency analysis and Gaussian distributions functions.

For the conversion of distances (measured in pixels) to m, a conversion factor of 0.182nm/pixel was used. This was based on a CCD camera pixel size of 3.63μm and an objective magnification of 20X (3.36μm/20). Videos were captured at a frame rate of 25fps.

Capture parameter	Setting
Camera Type	sCMSO
Laser Type	Blue405
Camera Level	16
Slider Shutter/ Slider Gain	1300/512
Frames per second (FPS)	25
Temperature	37°C
Viscosity	(Water) 0.690 cP

Table 2-4 Capture parameters for nanoparticle tracking analysis.

Analysis parameter	Setting
Detection Threshold	6
Blur Size	Auto
Max Jump Distance	Auto: 14.5 - 23.2 pix

Table 2-5 Video analysis settings for nanoparticle tracking analysis.

2.10 Enzymatic assays

2.10.1 GOx/HRP ABTS reaction assay

DNA-enzyme conjugate structures were prepared in a total of 100 μL: to 50 μl purified DNA nanoballs (1-hour incubation, concentration A_{260nm} ~ 1), DNA-oligonucleotide-HRP/GOx conjugates were added at a final concentration of 0.1 μM (concentrations of DNA-enzyme conjugates were determined based on A_{280nm} measurements), with the remaining volume made

up with 0.1M sodium phosphate, 0.15M NaCl, pH 7.2. The oligonucleotide-enzyme conjugates were annealed to the DNA nanoball at 37°C in a thermal heat block (Eppendorf ThermoMixer® C) for 1 hour. For reactions with free enzymes (+/- DNA nanoballs): to 50 µl purified DNA nanoballs (1-hour incubation, concentration A_{260nm} ~ 1) each enzyme was added at a final concentration of 0.1 µM. The remaining volume was made up to 100 µL with 0.1M sodium phosphate, 0.15 M NaCl, pH 7.2.

DNA-enzyme solutions were buffer exchanged in 0.1M β-D-glucose, 0.1M sodium phosphate, 0.15M NaCl, pH 7.2, by ultracentrifugation using a Sartorious Vivacon® 500 centrifugal spin filter, with a 100 kDa or 125 kDa molecular weight cut off. Centrifugation was performed at 3000 x g at room temperature for 15-30 minutes. 50 µL of the DNA nanoball-enzyme solution was deposited in 96-well plates. The total volume of this reaction mixture was made up to 200 µL with reaction buffer (0.1M β-D-glucose, 0.1M sodium phosphate, 0.15M NaCl, pH 7.2) and ABTS added to a final concentration between 0.125mM - 5mM. All reactions were performed in clear 96 well plates (Corning® clear polystyrene 96 well microplates). After adding ABTS substrate, the reaction progress was monitored at 405 nm using a TECAN Safire2™ multi-mode microplate plate reader, with Magellan™ Data Analysis Software. All measurements were conducted at room temperature.

2.10.2 Analysis of Transaminase and norcoclaurine synthase conversion products by analytical HPLC

DNA-enzyme and DNA-enzyme conjugate solutions were prepared by combining 50 µl purified DNA nanoballs (1-hour incubation, concentration A_{260nm} ~ 1), with DNA-oligonucleotide-TAm/NCS conjugates (or free enzyme) added at a final concentration of 0.1 µM (concentration determined based on A_{280nm} measurements), the final volume of the sample was 200 µl, with any remaining volume made up with reaction buffer (50 mM HEPES, 1 mM Pyridoxal phosphate, 10 mM sodium pyruvate, 5mM ascorbic acid, with either 10mM dopamine hydrochloride or 3-hydroxyphenethylamine). The sample was then buffer exchanged (in reaction buffer) by ultracentrifugation using a Sartorious Vivacon® 500 centrifugal spin filter, with a 100 kDa or 125 kDa molecular weight cut off. Centrifugation was performed at 3000 x g at room temperature for 15-30 minutes. Reactions were then immediately incubated at 37°C for 6 hours in a thermal heat block (Eppendorf ThermoMixer® C). To analyse product formation by RP-HPLC, DNA-enzyme (conjugate) structures were removed from the reaction mixture by ultrafiltration using a Vivaspin® centrifugal concentrator with a 3K molecular

weight cut off filter (sartorious vivaspin 500). The filtrate was analysed by analytical HPLC to determine product conversion.

Analytical high preformance liquid chromatography (HPLC) was conducted using a thermo scientific UltiMate 3000 UHPLC system equipped with chromeleon 7.2 analysis software. Reaction products were analysed by reverse phase chromatography using an Acclaim™ 120 C18 Column (thermofisher), monitored at 260, 230 and 280nm, at a flow rate of 0.25ml/min. The analysis was preformed using a gradient of acetonitrile from 3 to 50% over 25 minutes. The aqueous phase was HPLC grade water 0.1% TFA. The injection volume was 15µl. All analysis was performed at room temperature.

2.11 Mass spectrometry

2.11.1 Electrospray ionization mass spectrometry (ESI-MS)

Electrospray ionization mass spectrometry (ESI-MS) was performed at the UCL chemistry mass spectrometry facility. For the analysis of transaminase and norcoclaurine synthase bi-enzyme reaction products, product fractions collected by analytical HPLC using an UltiMate 3000 UHPLC system as described in the previous section. ESI-MS was conducted using a Waters LCT Premier Q-TOF mass spectrometer in positive ionization mode.

Chapter 3

A DNA polyhedron for the display of biomolecules

3.1 Introduction

Three dimensional polyhedral structures are key architectures in the area of DNA nnotechnology[155–157], which display defined and regular geometries. These structures also make ideal scaffolds for the display of molecules due to the regular spacing of vertices, and the availability of positions for modification across the entire structure. The use of a tile based approach for the construction of three dimensional geometric objects has the advantage of only requiring a single unit, from which a higher order structure can be formed, in contrast to other approaches which require more complex design processes[156]. This chapter describes the design and assembly of a three-armed DNA tile for the formation of polyhedral structures for the immobilization of enzymes or other biomolecules.

3.2 Results

3.2.1 Design of the three-armed tile

The DNA tile consists of three double crossover arms with complementary ends to promote tile to tile joining (figure 3-1). The tile comprises of nine oligonucleotides (table 3-1), three oligonucleotides (A1-A3) form the major portion of the arms, which are held together by internal crossover strands (B1-3) and sticky ends (C1-3). The width of the arm is 4nm (two DNA duplexes in width) and the tile to tile length is 84 bases (28.6nm) - eight full helical turns, which is based on the value of 10.5 bp/turn and a rise of 0.34nm/bp. An integer number of helical turns is thought to promote the formation of a closed structure, as opposed to a lattice, as the connected tiles face the same plane so that the inherent curvature of the tile is amplified[155]. Additionally, the tile features three non-base paired regions between the arms, 3 bases in length, to confer flexibility to the structure. This was also thought to enable closure of the structures by introducing some degree of freedom to the arm structure. The complementary or sticky ends, on the C and A ends of the oligonucleotides are complementary to one another, so that one arm can join any other. A tetrahedron and dodecahedron, are structures, that in theory could be assembled from the three-armed tile (figure 3-1).

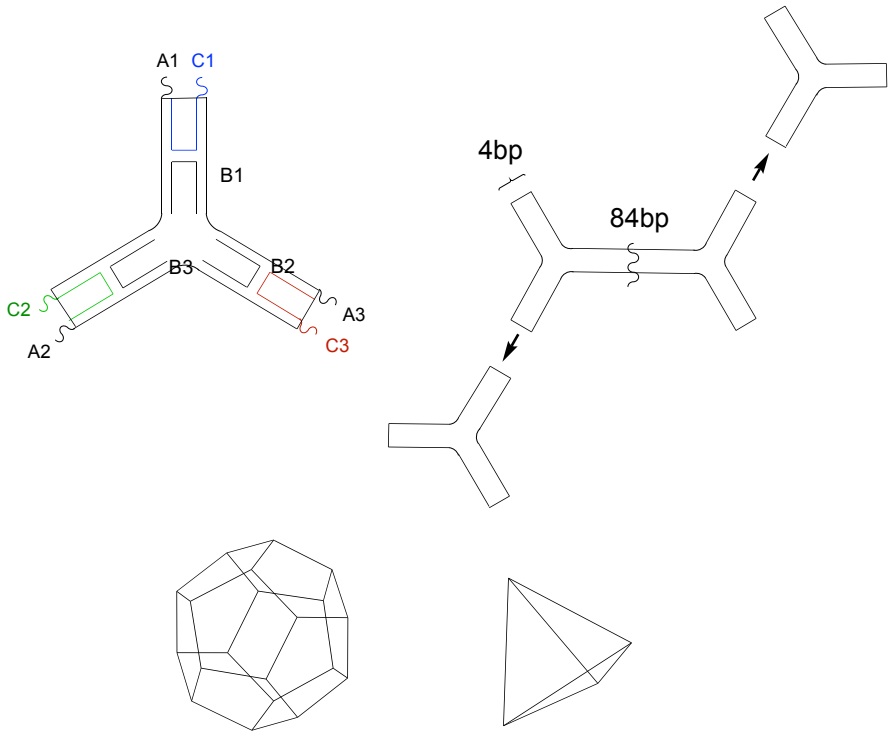

Figure 3-1 Design of the single three-armed tile and proposed joining of two tiles through complementary ends. Top: Shows the three-armed tile with three sequence specific complementary ends to promote hybridization of individual tiles. **Bottom:** hypothesised assembly structures.

Name	Length (nt)	Position
A1, A2, A3	87	'Arms'
B1,B2,B3	54	Internal crossovers/ points of conjugation
C1,C2,C3	30	Crossovers/sticky ends

Table 3-1 A list of the oligonucleotides used for this structure. A single tile is comprised 9 oligonucleotides. The length of complementary ends is 10 bases. The full sequences are listed in appendix C.

It was anticipated that biomolecules could be conjugated at defined positions on the vertices of the assembled structures. Two alternative designs are presented (figure 3-2), where a single internal 'B' is modified with a target biomolecule (depicted as a blue circle), or the modification of all three B strands to incorporate three different target molecules (depicted as green circles).

These modified DNA oligonucleotides could be prepared using a range of covalent chemistries, including the amine to thiol crosslinking procedure used in the preceding chapters for the preparation of enzyme conjugates.

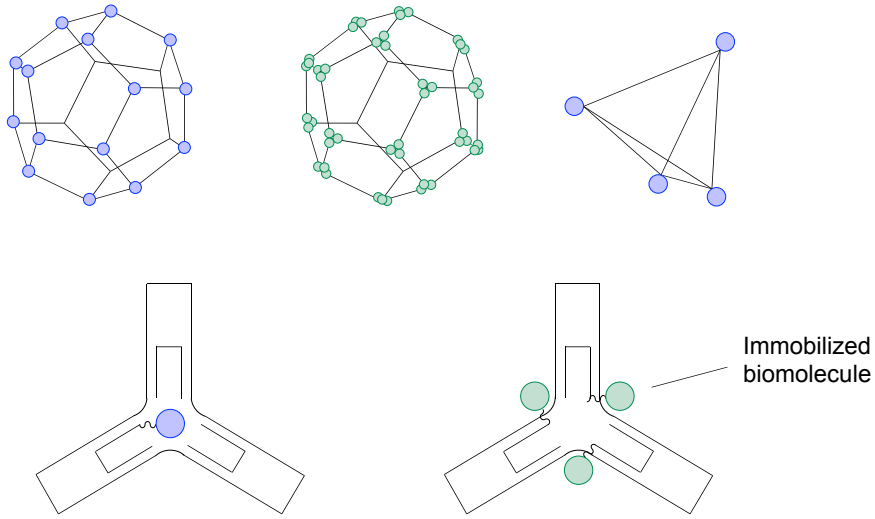

Figure 3-2 Proposed designs for biomolecule display on the three-armed tiles and hypothesized assembly of the tile to form a decorated dodecahedron and tetrahedron. Two potential tile configurations are shown (below), an internal B strand modified with a single biomolecule and (bottom right), and a tile modified with three molecules attached to all three internal B strands.

3.2.2 Assembly of the three-armed tile

DNA tiles were annealed over a slow cooling programme from 95 to 22°C over 8 hours in 1 X TBE buffer, 12mM $MgCl_2$. The sequential addition of oligonucleotides was analysed by agarose gel electrophoresis (figure 3-3) to monitor the assembly process. For all A strand oligos (lane 1), a single band is observed, with the addition of strand B1, three products are produced which correspond to the formation of two further structures (in addition to excess A strands). On addition of strands B2 and B3 (lane 4), a single major product is seen, which corresponds to the single tile unit (without C strand oligos). The addition of the remaining C strand oligonucleotides, to enable the joining of the tiles to one another, produces a product which migrates no further than the well (last lane). The migration of the fully annealed product suggests that aggregation or non-specific assembly occurs between the tile structures. The same assembly process was also analysed using a lower percentage agarose gel (1%) to determine if the products observed in the well for the 3% gel would migrate any further through

the gel. As the higher gel strength could have impeded migration of the products. For the same products electrophoresed on an equivalent 1% gel, an identical pattern of migration was observed (figure 3-3, bottom gel). The fully annealed product (lane 7) migrates no further than the well, which would support the interpretation that the addition of C oligonucleotides promotes the aggregation of tiles. At this percentage (1%), the stepwise addition of A + B oligonucleotides shown in lanes 1-4 remains unresolved.

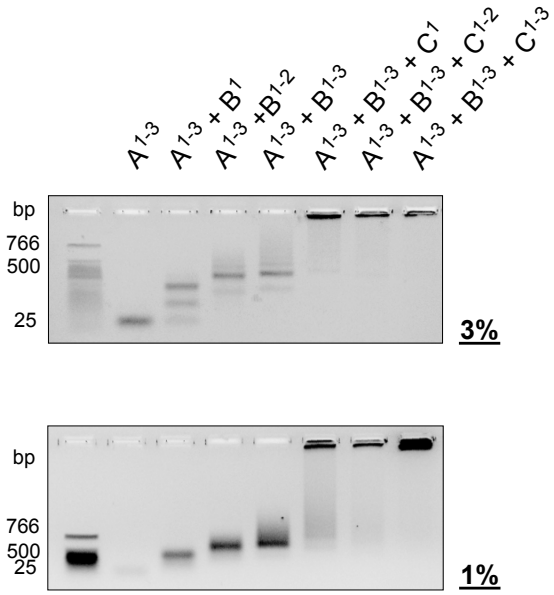

Figure 3-3 Analysis of the assembly of tile-based structure by agarose gel electrophoresis using an 8-hour annealing method. Note gel colour inverted for clarity. Lane 1: A1-3 oligonucleotides only; lane 2: A1-3 + B1; lane 3: oligo A1-3 + B1-2; lane 4: A1-3 + B1-3; lane 7: all oligonucleotides annealed. Gel: 1 X TBE, 1% (top) or 3% (bottom) agarose. Gel running conditions for both gels: 1X TBE running buffer, 12mM $MgCl_2$. Ladder: NEB low molecular weight ladder.

To further investigate the assembly process, two alternative annealing strategies were attempted. (1) A 24-hour annealing method from 95 to 22°C (fully annealed products shown in lane 1, figure 3-4 and (2) a 'partial' annealing process. The 'partial' annealing process involves annealing all A-B oligonucleotides by heating to 95°C for 10 minutes, then cooling to room temperature, followed by the addition of 'sticky end' C1-3 oligonucleotides, to reduce potential aggregation of the structure (lane 3, figure 3-4). Oligonucleotides annealed using 8-hour, 24 hour and 'partial' methods were compared by agarose gel electrophoresis (1% gel) shown in figure 3-4. No difference in migration was observed for the 8 hour and 24 hour annealed products (figure 3-4, lanes 1 and 2). Oligonucleotides annealed using the 'partial' method do

not produce a distinct product, either in the well nor as discrete band further through the gel. Although, some faint staining is visible in the well.

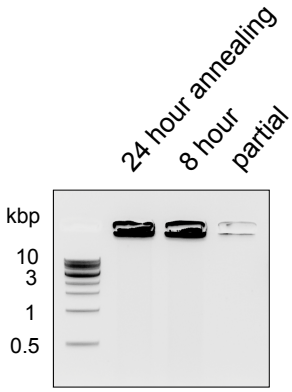

Figure 3-4 Analysis of the effect of alternative annealing procedures. Lane 1: products annealed using a 24-hour annealing method (between 95 to 22°C); lane 2: products annealed using an 8 hour annealing method; lane 3: oligonucleotides annealed using the 'partial' annealing method. Ladder: NEB 1kbp DNA ladder, gel conditions were: 1% gel, 1X TBE. Running buffer, gel: 12mM $MgCl_2$ 1X TBE.

The effect of $MgCl_2$ concentration on the partial annealing process was investigated. The quick annealing method involves a 10-min heating step at 95°C, followed by the addition of 'sticky end' C1-3 oligonucleotides last at room temperature. Three concentrations of $MgCl_2$ were tested, 3-12mM, in 1X TBE buffer. Assembly products at 3, 6 and 12mM $MgCl_2$ were analysed by agarose gel electrophoresis, shown in figure 3-5. The first lane for all three concentrations corresponds to annealed A1-3 + B1-3 oligonucleotides. Each subsequent lane corresponds to the addition of a C oligonucleotide, from C1-3. At 3mM $MgCl_2$, higher order structures fail to assemble, based on the absence of a significant product shift from lanes 1 and 4. In fact, the migration of products in lane 1 strongly suggests that A + B oligonucleotides do not assemble correctly; although, an A/B oligonucleotide-only control was not included in this analysis to confirm this observation. At 6mM $MgCl_2$, annealed A + B oligonucleotides produce a product which migrates significantly higher than the equivalent sample annealed at 3mM $MgCl_2$. The addition of each C oligonucleotides results in the formation of a successively higher mw spread of products. The same pattern of migration is observed at 12mM $MgCl_2$,, but with a more significant upshift of products with the addition of each C oligonucleotide. Annealed products at all concentrations do not yield products which remain in the well. These results demonstrate the importance of $MgCl_2$ concentration on the annealing process in order to promote the assembly of oligonucleotides.

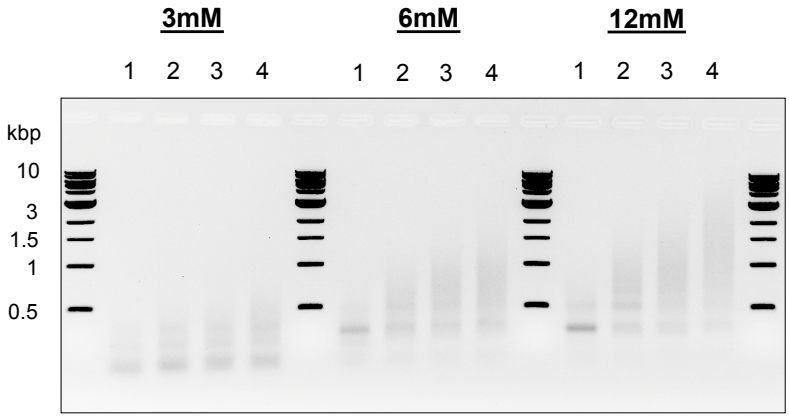

Sample	Annealed oligonucleotides
1	A1-3 + B1-3
2	A1-3 + B1-3 + C1
3	A1-3 + B1-3 + C1-2
4	A1-3 + B1-3 + C1-3

Figure 3-5 Partial annealing procedure performed at 3,6 and 12mM $MgCl_2$. Gel conditions were: 1% agarose gel, 1X TBE. Running buffer: 1 X TBE. The table indicates the sample run in lanes 1-4. Ladder: NEB 1 kbp ladder. Gel colour was inverted for clarity.

3.2.3 Characterisation of annealed products by atomic force microscopy (AFM)

Initially, DNA oligonucleotides (A-C) were assembled using a short annealing method (heated at 95°C for 10 mins, then cooled to room temperature in 1 X TBE buffer, 12mM $MgCl_2$) and analysed by atomic force microscopy (AFM). AFM was conducted in liquid and samples were deposited with the addition of nickel chloride to facilitate interaction of the DNA structures with the mica surface. The results of this analysis are shown in figure 3-6. Visibly aggregated products were observed, with no defined geometries which would suggest the correct assembly of the 3-armed tile structure into defined objects. A selection of particles observed by AFM were analysed to determine their x and y profiles using the Gwyddion SPM software profile extraction function; four profiles are shown in figure 3-6. For these profiles, a maximum height between ~ 4-10nm is observed, and an x dimension of ~ 0.1μm. The average height of particles observed by AFM was 3.6 ± 0.2 nm (s.d.); which is based on the Gaussian fitting to the frequency distribution from the height analysis all particles shown in figure 3-6.

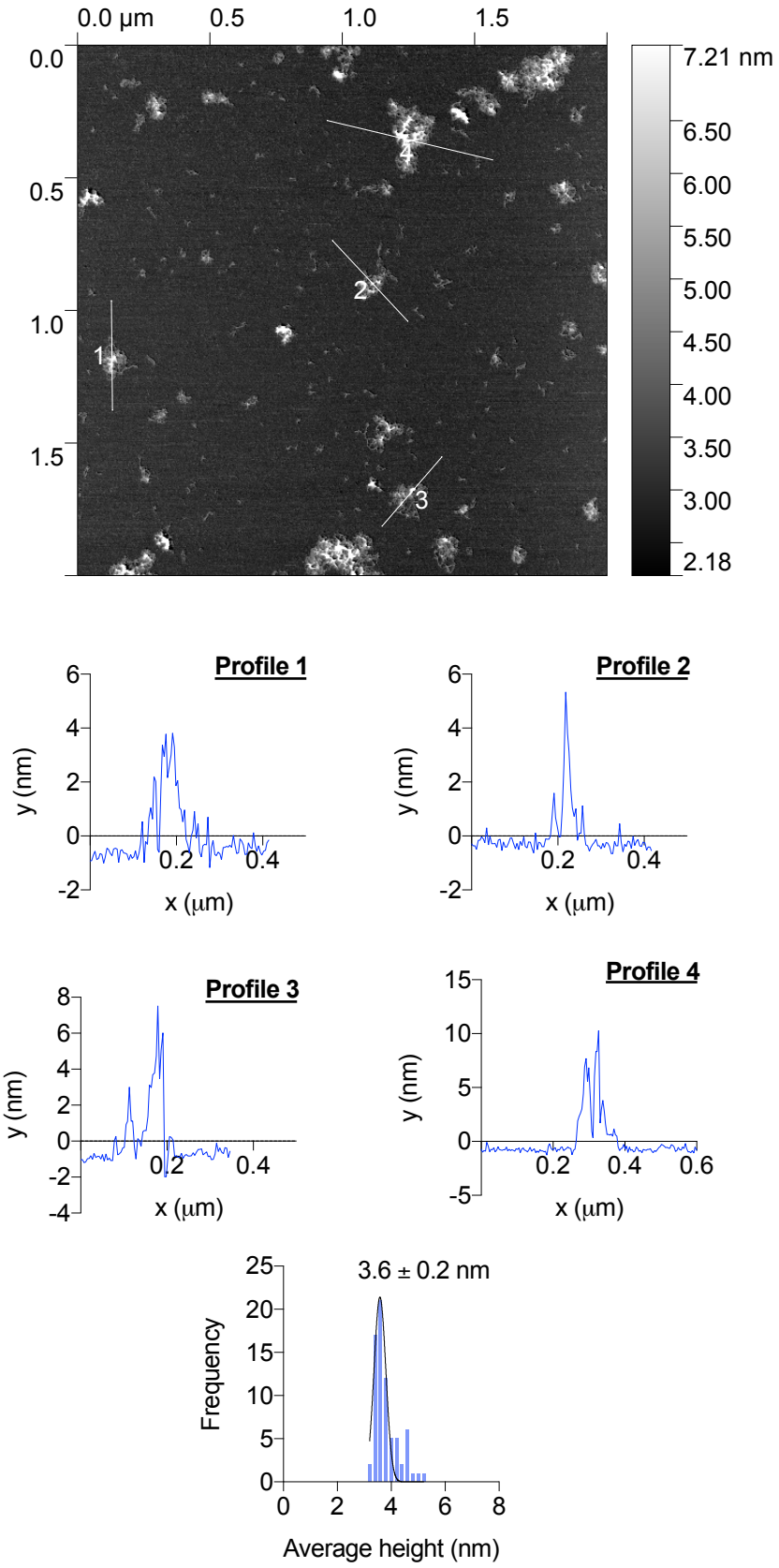

Figure 3-6 Analysis of assembly products (annealed at 95°C for 10 mins, then cooled to room temperature) by atomic force microscopy (AFM). Images were processed using

Gwyddion SPM analysis software. Analysis of profiles for 4 objects and the average height of grains observed by AFM are also shown.

The analysis of 8-hour annealed products by AFM is shown in figure 3-7. Once again, this analysis was conducted in liquid and samples were deposited with the addition of nickel chloride to facilitate interaction of the DNA structures with the mica surface. For the 8-hour assembled products, largely discrete particles are observed by AFM; however, there is variation in the dimensions of particles. A selection of particles displaying defined geometries from the AFM analysis are shown in figure 3-8, the consistent triangular motif suggests correct formation and assembly of the 3-armed DNA tile. A profile analysis of the height and width of the selected particles is also shown in figure 3-8. The profile analysis indicates a consistent height of 2 nm in the y dimension, which corresponds to the height of a single DNA duplex, which would suggest that these particular objects lay flat as opposed to raised. The average width of peaks (x dimension) is ~7nm, which is in agreement with the theoretical width of 4nm, taking into account the overestimation in the lateral dimension. An analysis of all observed grains/particles by AFM (figure 3-9 – analysed grains are highlighted by the mask on the AFM image) demonstrate an average height of 2.6 ± 0.2nm, which again, corresponds to the height of a single DNA duplex.

In addition to the analysis described above, 24 visible edges of particles (from the AFM analysis in figure 3-9) were measured; the average length was found to be 37.7 ± 5.0nm (s.d.). This is slightly greater than the theoretical length of 28.6nm (the tile to tile distance), but still in reasonable agreement given the error and the overestimation in the lateral dimension (which can be introduced by the tip during AFM). Although the majority of particles observed by AFM appear to represent assembled tiles lying flat, which is supported by the height analysis of grains, there is some evidence to support the formation of closed structures, in the form of two apparent tetrahedrons which were observed by AFM (figure 3-10). The highest point measured, in the y dimension for both objects, is ~ 5nm (figure 3-10, bottom profile), the average length of observed edges is 33.7 nm for object 1 and 36.6nm for 2 (table 3-2), which agrees well with theoretical length of the edge (the tile to tile length). The observed height could represent two overlain duplexes, which are collapsed through interaction with the surface or through compression by the tip.

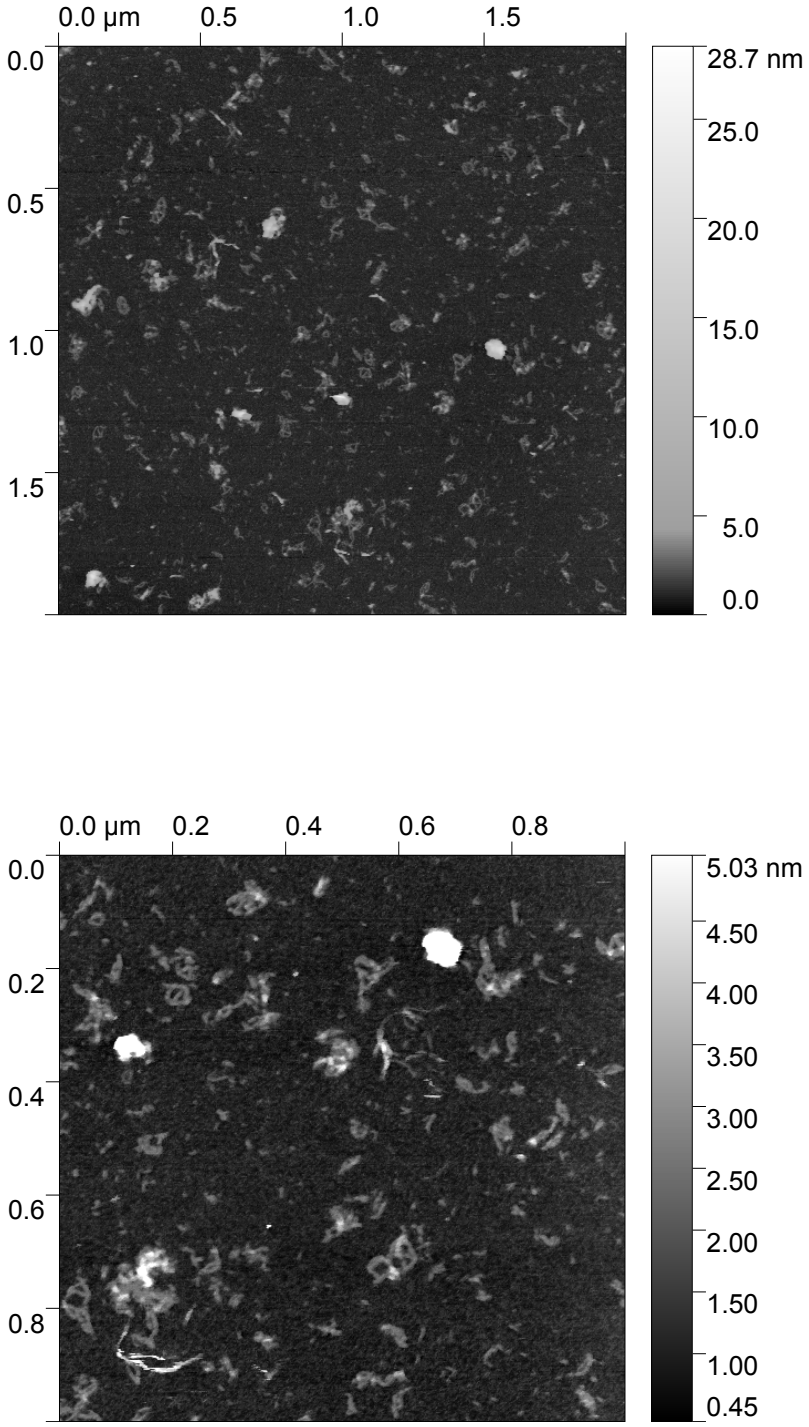

Figure 3-7 Evidence of assembly of the DNA tile by atomic force microscopy (AFM). The sample was annealed over an 8 hour annealing method. Images were processed using Gwyddion SPM software.

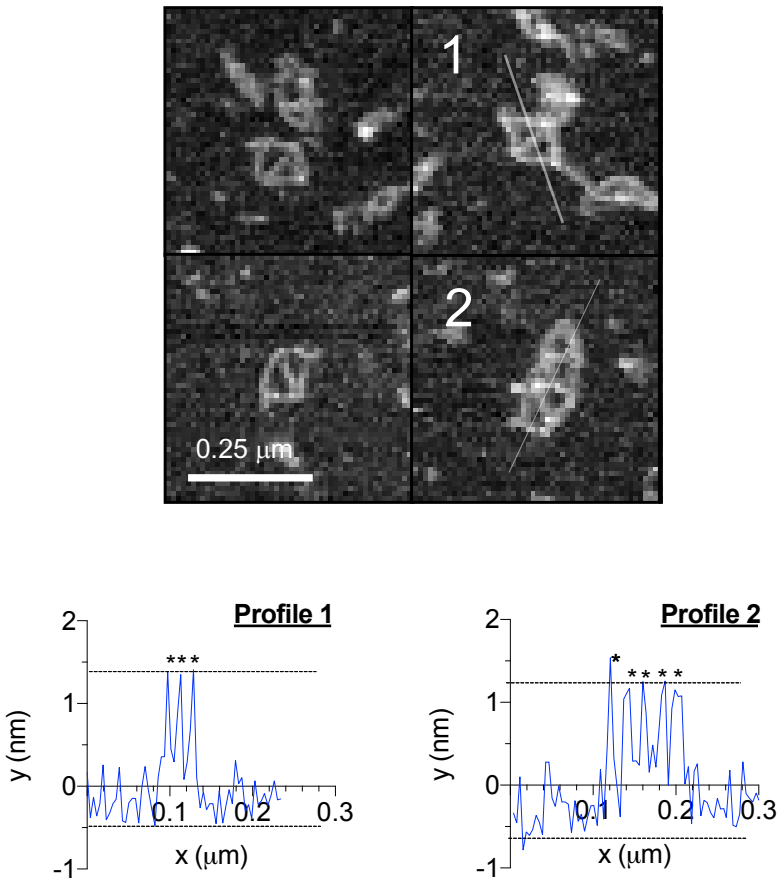

Figure 3-8 Evidence of assembly of the DNA tile by atomic force microscopy (AFM). Images were processed using Gwyddion SPM analysis software. A selection of structures are shown, which appear to demonstrate the assembly of the DNA tile to form consistent 'triangular' units. Below: shows the profile analysis in the x and y dimension for particles labelled 1 and 2. The * indicates the lines crossed. A height of 2nm is observed for these regions.

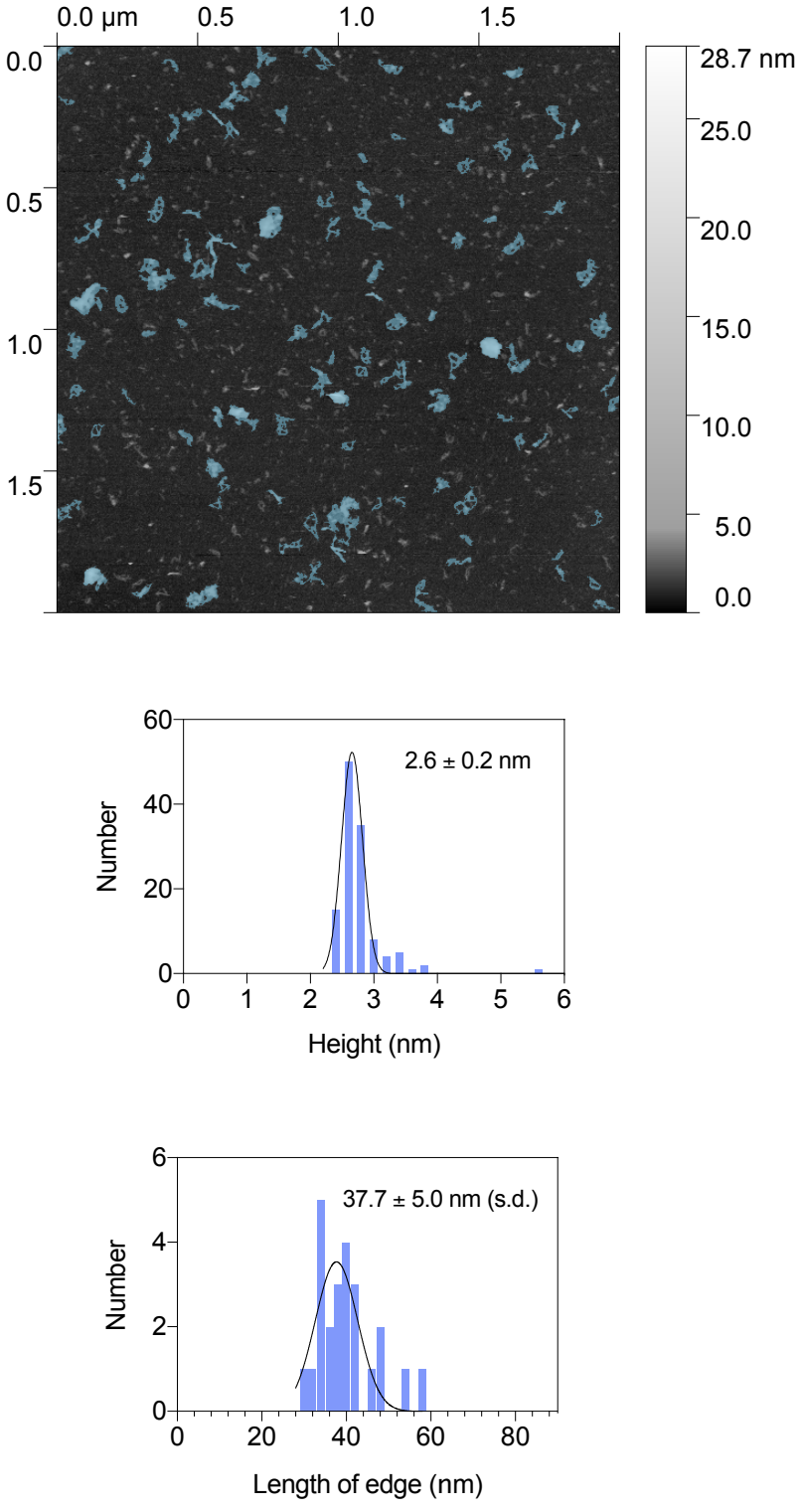

Figure 3-9 Height and edge analysis for masked objects observed by atomic force microscopy. Height of the analysed (masked particles shown in figure 3-7). This is the *Maximum*, the maximum value (height) occurring inside the grain (masked object). The analysis was preformed using the grain analysis function using gwyddion SPM analysis software.

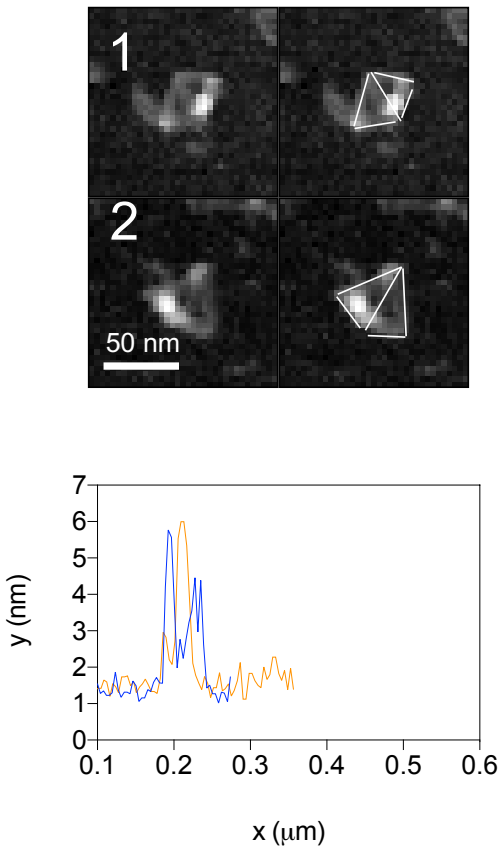

Figure 3-10 Evidence of self-assembly of three armed tiles to form two tetrahedra and corresponding x/y profile analysis for objects 1 (yellow) and 2 (blue).

Object	Average length of 5 edges (nm) (± S.D)
1	33.7 ± 2.3
2	36.6 ± 8.7

Table 3-2 Average length of the observed edges for the two tetrahedron structures.

Based on the analysis of structures observed by AFM in figure 3-10.

3.3 Conclusion

In this section, a tile-based method was used to assemble DNA polyhedral cages for the purpose of arranging biomolecules. It was envisaged that the edges or vertices of the assembled structures could be used to display target molecules. The stepwise assembly processes indicated the correct assembly of the DNA tile structure, however, the assembly of those tiles together appeared to form aggregated structures, based on the migration of the annealed product by agarose gel electrophoresis. The analysis of products by atomic force microscopy, indicated assembly of the three-arm tile structure to produce predominantly flat assemblies. The dimensions of those structures, based on the measured edges and average height of particles, corresponded to the theoretical dimensions for the tile structure. Evidence of closed structures, in the form of two tetrahedra, were also observed by AFM. This particular assembly strategy was not pursued further for the display of molecules, as the yield of correctly assembled structures was considered too low.

One drawback associated with the use of tile or motif to form larger assemblies, is that they are sensitive to the stoichiometry and purity of the constituent oligonucleotides. Although the DNA oligonucleotides used in this chapter were purified by anion exchange chromatography prior to their use, and a good degree of purity is obtained using this method, further purity of the DNA oligonucleotides could be achieved using a gel-based purification approach. The annealing conditions could also be modified, for example by using a slower cooling ramp or the adjustment of the annealing buffer composition. It may also be necessary to alter the design of the tile, for instance, through changes to the loop region, the length of arms, or the connecting region to improve the rigidity of the structure. The height of particles observed by AFM suggest that the assemblies may be collapsed due to adsorption to the surface for imaging, or through interaction or compression by the tip. The requirement for additional divalent cations ($NiCl_2$) for deposition may also affect the integrity of the structures. In the future, alternative characterization techniques could be used, such as transmission electron microscopy (TEM) to better retain the structural integrity of the annealed structure.

Chapter 4

A DNA nanoball for enzyme immobilization

4.1 Introduction

Enzyme immobilization is an important process in the areas of industrial biotechnology and biocatalysis[158,159] and for biomedical purposes, such as in diagnostic devices[160]. Enzyme immobilization facilitates the recovery of catalysts after their use, where they would otherwise be lost[139], or in circumstances where it is necessary that they are bound to a solid support. It also enables the separation of the catalytic species from the bulk environment, and may even improve enzyme stability[161]. The programmability of DNA has made it a highly versatile molecule for the assembly of nanoscale structures, with applications across biotechnology, biomedicine and molecular computation[162]. DNA nanostructures can be used to display biomolecules with nanometer precision[163], including enzymes[113–115,118,120–126,128–133,164–170]. However, the nature of many DNA structures, which often involve the hybridization of numerous DNA oligonucleotides to one another or to a scaffold DNA, prohibits their scale up for use in technological applications. Furthermore, the yield of correctly assembled DNA structures may be low[171], or require extensive assembly times, sometimes in the region of days to promote the correct formation of structures[44]. Alternatively, DNA nanostructures may be generated through enzymatic synthesis, which bypasses many of the limitations associated with the assembly of complex DNA structures, and this may prove to be a critical aspect in their application in the area of biotechnology.

In this chapter, we describe a DNA based display system for the immobilization of enzyme cascades. The structure, the DNA nanoball, is synthesised through phi29 mediated rolling circle amplification (figure 4-1) to generate a concatemeric ssDNA which is designed to self-compact to form a mesh-like 'nanoball'[57,59,172]. Enzymes are recruited to the NB structure through conjugation to carrier DNA oligonucleotides which hybridize to binding sites which constitute the DNA NB structure. A horseradish peroxidase-glucose oxidase enzyme pair was immobilized on DNA NBs as a model bi-enzyme system to investigate the effect of sequestration by the DNA scaffold. The glucose oxidase/peroxidase system is a stable bi-enzyme system which demonstrates Michaelis-Menten kinetics[173]. Glucose oxidase (EC 1.1.3.4) is a FAD-dependent oxidoreductase which catalyses the oxidation of glucose to yield gluconic acid and hydrogen peroxide. HRP (EC 1.11.1.7) reduces H_2O_2 through an electron

donor, such as the chromogenic substrate 2,2′-Azino-bis(3-ethylbenzothiazoline-6-sulfonic acid), ABTS, whose oxidation can be monitored spectrophotometrically at 405nm.

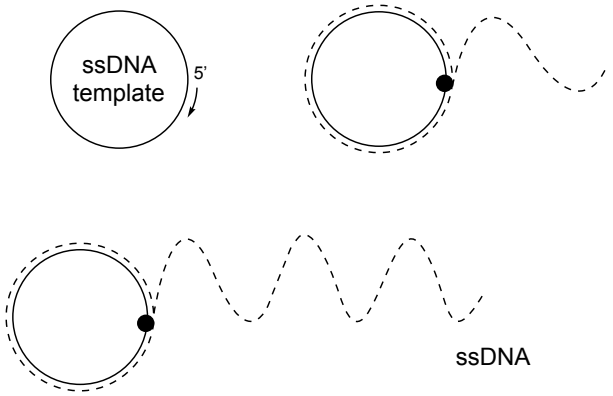

Figure 4-1 Schematic of rolling circle amplification. Illustrating the principle of strand displacement. RCA is initiated from a primed ssDNA or RNA starting template (the polymerase, phi29, is indicated by a black dot), the synthesised complement DNA is displaced by the polymerase, which enables it to continue extension in a 'rolling' fashion along the circularised template.

Almost all other examples of enzymes arranged on DNA nanostructures involve their interspacing on the nanometre range in defined positions. According to many of these reports, spatial proximity between enzymes is thought to improve the activity of the cascade. Similar effects have also been shown for enzymes immobilized on protein scaffolds[174,175], as well as on other nanoparticles[98]. However, it is not clear if these effects are the result of 'proximity channelling', or due to the altered conditions conferred by the DNA scaffold (or other structures on which they are immobilized), or through changes to the specificity of the target enzymes[137,138]. Conversely, the NB configuration aims to sequester or co-cluster target enzymes or enzyme cascades in a way that is analogous to an 'agglomerate' or aggregate. It has been suggested that clustering multiple copies of enzymes belonging to a reaction cascade in this form can improve the processing of intermediates[176] - the premise being that an intermediate has increased probability of being processed by many copies of an enzyme within the co-clustered unit, than it would do by an individual enzyme alone.

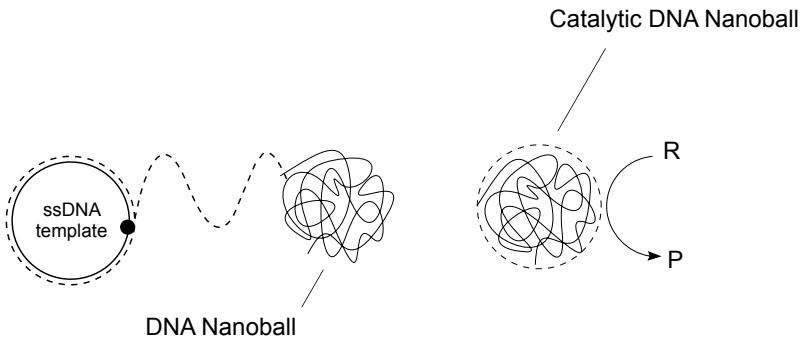

Figure 4-2 Overall outline of the synthesis of DNA nanoballs and their use as a catalytic particle.

4.2 Results

4.2.1 Design of DNA nanoballs for enzyme compartmentalization or concentration

DNA 'nanoballs' are enzymatically synthesized by phi29 rolling circle amplification of a primed circular 200nt ssDNA template[177]. Rolling circle amplification (RCA) refers to the isothermal DNA amplification of a circular ssDNA or RNA template by phi29 DNA polymerase[178]. Phi29 possess strand displacement activity, which allows it to replicate continually through synthesized dsDNA or secondary structure on a circular ssDNA or RNA template (in a 'rolling' fashion) to generate a concatemeric ssDNA. Here, DNA nanoballs are synthesized from a 200nt circular ssDNA which incorporates three unique binding regions and three self-complementary stem loop structures (figure 4-3). The stem loop structures were incorporated to promote compaction of the synthesized ssDNA by self-annealing to form discrete mesh-like nanoscale particles, each derived from a single starting ssDNA template. The binding sites (denoted b1-3) serve as hybridization points for the incorporation of up to three orthogonal oligonucleotide-enzyme conjugates, as a way of capturing enzyme, or other biomolecules, to the DNA nanoball structure. In this way multiple copies of a single DNA-enzyme conjugate may be incorporated to the DNA structure. In this particular design, up to three unique enzyme-DNA conjugates may be recruited. However, the starting ssDNA templates could be modified to accommodate more unique sites.

DNA oligonucleotide-enzyme conjugates may be prepared using a number of chemistries to create a covalent linkage between a target biomolecule and a carrier DNA oligonucleotide. One approach involves crosslinking between a thiol group (which is introduced at the 5' or 3' end of a target DNA oligonucleotide during solid phase phosphoramidite oligonucleotide synthesis) to a primary or secondary amine group, which are available in the form of ε-amino groups of

accessible lysine side chains or α-amine groups at the N-terminus on the target protein of interest.

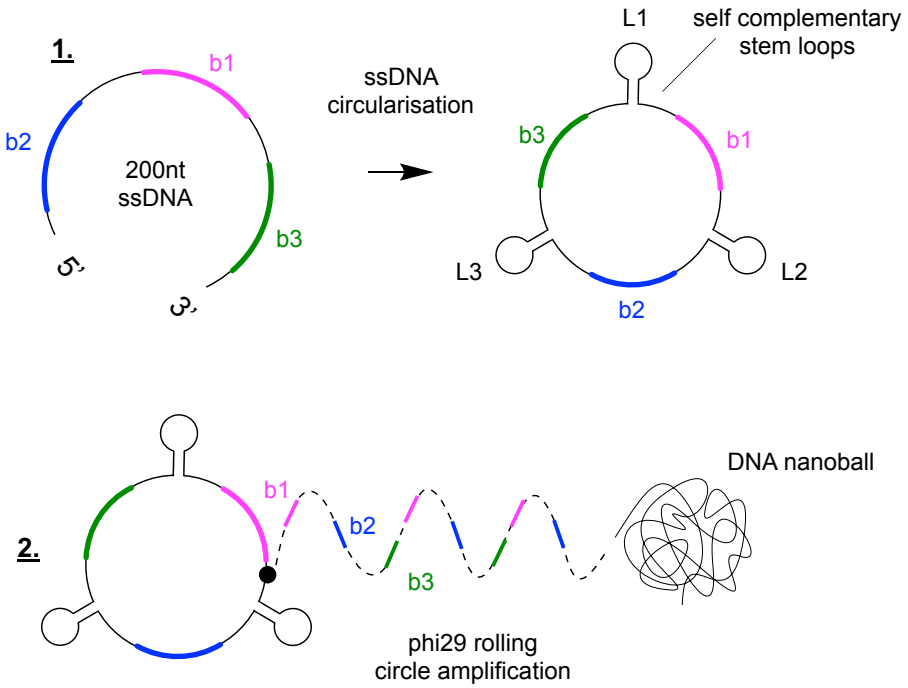

Figure 4-3 Illustration of the design of the starting 200nt ssDNA template and its amplification by phi29 mediated rolling circle amplification (RCA). **(1)** The 200nt ssDNA is circularised using a 'splint' primer to join the 5' and 3' end which is subsequently ligated to circularise the template. The starting ssDNA substrate comprises hairpin loops (L1-L3 20b in length) which are self-complementary, these structures are hypothesised to promote compaction of the synthesized DNA through self-annealing to form discrete DNA mesh structures. Binding sites (b1-3) serve as regions to which complementary DNA-enzyme may hybridize as a way of incorporating bio molecules to the DNA nanoball structure. **(2)** The primed ssDNA templated is amplified by phi29 mediated rolling circle amplification to generate a concatemeric ssDNA, which self-compacts to form the DNA nanoball structure.

Here, the heterobifunctional crosslinker sulfo-SMCC was selected for the conjugation of carrier DNA oligonucleotides to target enzymes through amine to thiol crosslinking. It was chosen for its characteristics of water solubility, linker length, and for its ability to form non-reversible covalent linkages[179]. Sulfo-SMCC, sulfosuccinimidyl-4-(*N*-maleimidomethyl)cyclohexane-1-carboxylate, is a heterobifunctional crosslinker, which comprises of two reactive groups, an NHS-ester and maleimide, which are linked by an 8.3 angstrom cyclohexane spacer arm. The NHS ester portion reacts with primary and secondary amine groups, to form a stable amide or

imide bond respectively. The maleimide moiety couples to sulfhydryls between pH 6.5 to 7.5 to form a thioether linkage[179,180] (figure 4-4). DNA-enzyme conjugates prepared in this way may then be hybridized to the DNA nanoball through the available hybridization sites on the synthesized ssDNA. Using the 200-mer starting template, up to three separate protein-DNA conjugates may be incorporated. The outline of the conjugation procedure, and incorporation of conjugates to the DNA nanoball is depicted in figure 4-4 below.

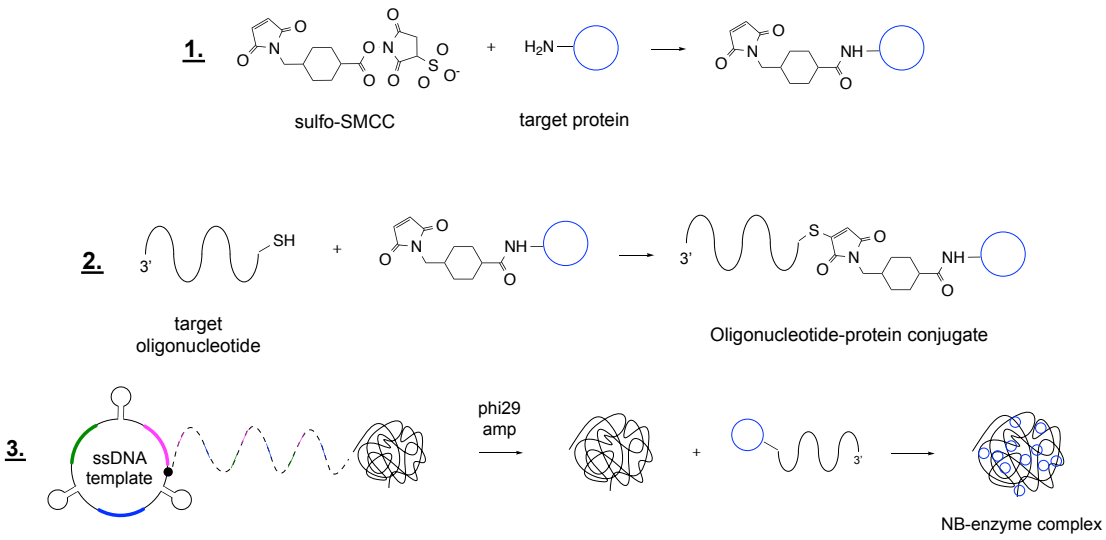

Figure 4-4 Outline of the conjugation procedure between a 5' thiol modified DNA oligonucleotide and target protein molecule using the heterobifunctional crosslinker sulfo-SMCC. (1) The first step involves activation of a target protein (depicted as a blue circle) through the NHS ester portion of the crosslinker. **(2)** The maleimide portion of the crosslinker couples to the thiol group introduced on the target DNA oligonucleotide to form a thioether linkage. This reaction proceeds between pH 6.5 to 7.5. **(3)** Conjugates are hybridized to the DNA NB structure as a way of incorporating target biomolecules.

4.2.2 Synthesis of DNA nanoballs by ϕ29 rolling circle amplification (RCA)

DNA Nanoball structures were synthesized by rolling circle amplification of a 200-mer ssDNA circular template. The circularized template was prepared by annealing a 'bridging' 25nt oligonucleotide to the linear 200nt ssDNA in order to close the 5' and 3' ends. The annealed product was assessed by non-denaturing polyacrylamide gel electrophoresis (PAGE) to confirm the circularisation of the linear ssDNA (figure 4-5), which is indicated by the up-shift in migration of the annealed product, in lane 3. The linear 200-mer ssDNA and 25nt 'bridging' primer, in lanes 1 and 2 respectively, were run separately for comparison. The circularized

product was ligated to covalently close the 5’ and 3’ ends and was amplified isothermally by phi29 rolling circle amplification (RCA); where extension occurs from the 3' end of the annealed bridge primer. The amplification products at one, two and three hour time points were analysed by agarose gel electrophoresis (figure 4-6) to assess the nature of the synthesized products and the effect of incubation time on the formation of the RCA product.

Figure 4-5 Circularisation of the 200-mer ssDNA template. This starting template serves as the substrate for Φ29 rolling circle amplification and for the synthesis of DNA nanoballs. Comparison of the linear template and annealed product. Analysed by 10%, 1 X TBE polyacrylamide gel electrophoresis. Lane 1: 25nt primer, Lane 2: 200nt linear ssDNA, Lane 3: annealed 200nt template.

The amplified products at all time points, do not migrate further than the well, and their intensity increases with incubation time. A fainter lower MW product (figure 4-6), is also observed at one and two hour time points but less so at three hours (above the 10kbp marker, indicated by the arrow). The impeded migration of the products suggests that the ssDNA is compacted through self-annealing, or that it is the result of interactions between discrete amplified ssDNA products. A progressive increase in the length of the RCA products is not observed by agarose gel electrophoresis, which further supports the view that intramolecular annealing occurs on the synthesized ssDNA.

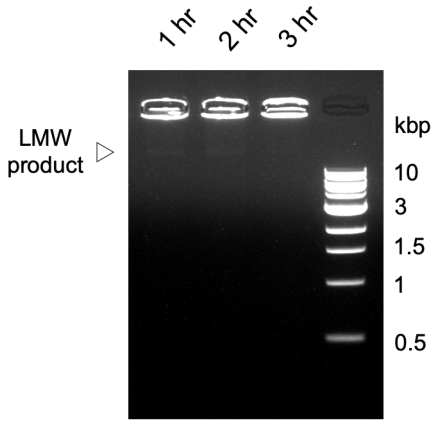

Figure 4-6 Analysis of RCA reaction products by agarose gel electrophoresis. Amplification of the circular ssDNA template was monitored by agarose gel electrophoresis (0.8% 1X TBE) at 1,2, and 3 hours, stained with EtBr. Lane 1: 1 hour incubation, lane 2: 2 hours incubation, lane 3: 3 hours. Increased product intensity is observed over time. In addition to the product within the well, a fainter lower molecular weight product is also observed between the well and the 10kbp marker (indicated by the arrow).

4.2.3 Characterization of synthesized DNA nanoballs by atomic force microscopy (AFM)

Phi29 amplified products were analysed by AFM to probe the structural nature of the synthesized nanoballs and to determine the level of compaction of the ssDNA through self-annealing. RCA reactions were quenched with EDTA, to inhibit synthesis by phi29 and to prevent denaturation of the enzyme, which could otherwise interact and/or effect the structural integrity of amplified DNA nanoballs. Initially, a blank sample containing phi29 enzyme only (with no DNA template), was analysed by AFM (figure 4-7). Three profiles across a selection of particles is also shown. The maximum height observed for these profiles is ~2 nm.

The AFM analysis of the EDTA quenched 200nt RCA products is shown in figure 4-8. Clusters of ssDNA are observed based on the morphology and height analysis of particles, which are consistent with those of ssDNA and dsDNA (figures 4-9 and 4-10). The maximum height of clusters was 2 nm, and the lowest 1 nm, which correspond to dsDNA and ssDNA respectively. The presence of dsDNA which would indicate self-hybridization of the synthesized ssDNA. Note, the presence of multiple spheres/dots can be explained by the presence of the DNA polymerase (phi29). This interpretation is also supported by the AFM analysis of the blank enzyme sample shown in figure 4-7, and the profile analysis for the particles observed.

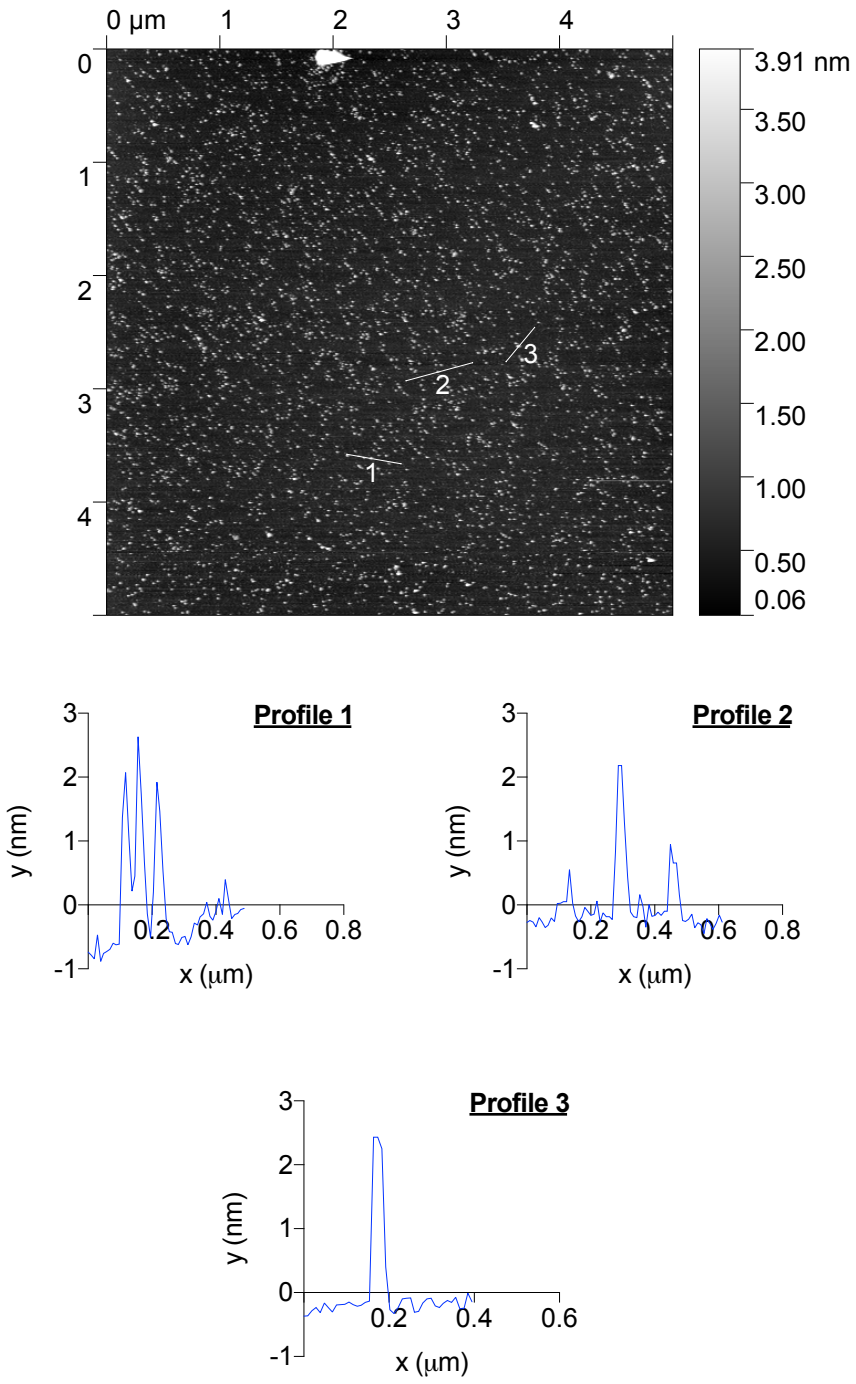

Figure 4-7 Analysis of a blank sample containing phi29 enzyme only (with no DNA template) by AFM. Data were flattened using Gwyddion SPM analysis software, with no further manipulation. X and y profiles across a series of particles are shown, which correspond to the lines depicted on the AFM micrograph.

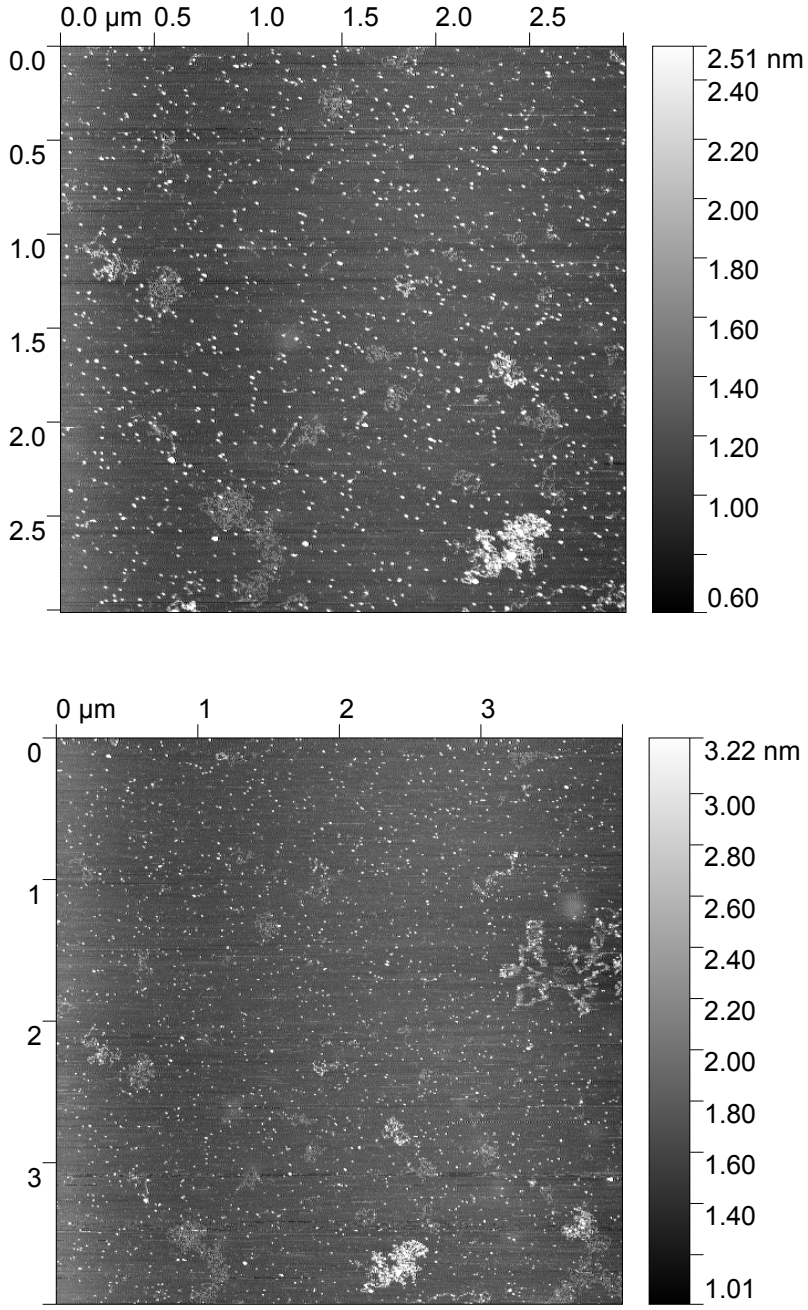

Figure 4-8 Pre-clean up - analysis of phi29 RCA products by atomic force microscopy. Data were flattened using gwyddion SPM analysis software, with no further manipulation. The RCA reaction process was quenched with EDTA prior to analysis. Multiple spheres/dots correspond to the polymerase, phi29, based on their height and diameter.

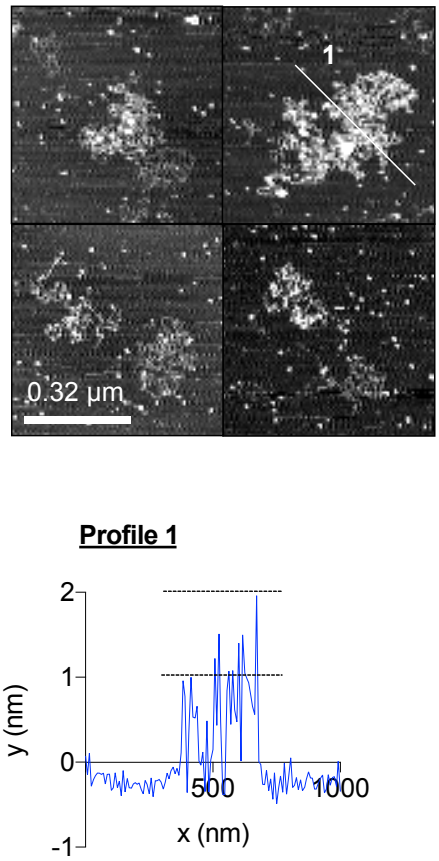

Figure 4-9 Pre-clean up - analysis of phi29 RCA products by atomic force microscopy. Profile analysis for one of the objects observed by AFM is also shown. Data were flattened using gwyddion SPM analysis software, with no further manipulation.

Further analysis of the EDTA quenched amplification products is shown in figure 4-10. Profiles 1-3 extend over single dots/spheres. The maximum height observed for profiles 1-3 is ~2-2.5 nm. These dimensions correspond to those obtained for the enzyme only (blank) control, and strongly indicate that these dots/spheres represent the phi29 enzyme. Based on their heights and morphology, profiles 4-6 correspond to synthesized ssDNA. For profiles 3 and 4, a maximum height of ~2 nm is observed, which correspond to the height of dsDNA, with lower peaks at ~ 1 nm, which agree with that of a ssDNA. Profile 6 demonstrates a maximum peak height of 1nm.

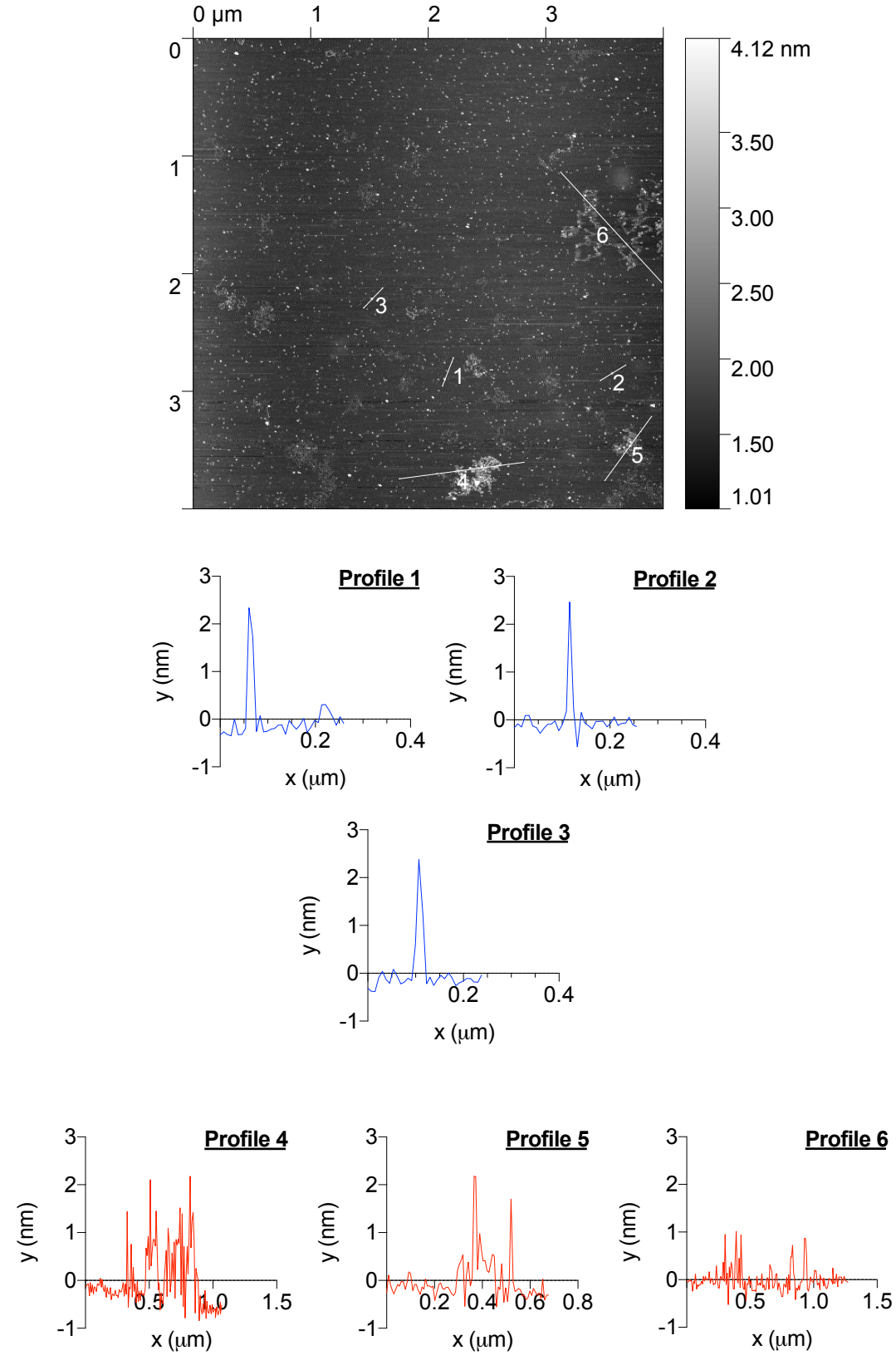

Figure 4-10 Pre-clean up - analysis of phi29 RCA products by atomic force microscopy (AFM). Profiles 1-3 are for three spherical particles which correspond to the phi29 enzyme. Profiles 4-6 correspond to synthesized ssDNA/dsDNA structures.

After quenching the reaction mixture, the synthesized products were purified using a protein binding resin (to remove the polymerase) and reconstituted in $MgCl_2$. The purified products were analysed by AFM (figure 4-11). Particles are mostly discrete/compact in appearance, rather than diffuse, as was observed for the EDTA quenched reaction products. The structural nature of the purified products suggests that compaction of the ssDNA, through self-complementary stem loop structures, does occurs. Although there is variability in the structures observed, a selection of particles (figure 4-11, bottom) demonstrate a degree of consistency in morphology and dimensions, which would support the view that the starting ssDNA template and incubation time can, to a degree, determine the dimensions of the synthesized nanoball structure.

Particles in figure 4-11 were analysed to determine the mean height and radius of the RCA reaction products. The blue mask over particles indicates the structures analysed (figure 4-12). An average maximum height (the maximum height occurring within the masked grain) of 6.6nm, and an average circumcircle radius of 75.3nm (figure 4-13) were found. The mean values were determined by Gaussian fittings to the frequency distributions derived from the analysed grains. This analysis was preformed using the grain selection function using gwyddion SPM analysis software[153]. There is greater consistency in the height of particles, than for the diameter, which can be explained by the process of sample deposition onto the mica surface. This process relies on Ni^{2+} to bridge the interaction between DNA and negatively charged surface (mica). The process of adsorption onto the mica surface can also result in the flattening of structures, which may also explain why the average diameter of particles (75.3 ± 22.9 nm) is approximately 10 X greater than the average height (6.6 ± 1.8 nm).

A selection of grains were analysed using the x and y profile extraction function (figure 4-12, profiles 1,2 and 3). The majority of particles demonstrate a higher central region compared to the edge, which would suggest a spherical object, in line with the proposed ball or mesh like structure. Once again, there is good agreement between the height of all profiles. An average of ~5-6 nm is observed across all particles. There is greater variability in the x dimension (the width) for all three profiles (1,2 and 3). Based on the AFM analysis alone, it is not possible to determine if particles are the product of synthesis from as single ssDNA template (clonal), or if they are the result of interactions between multiple synthesized ssDNA. As described here, there is no way to distinguish between the two possibilities. Given the distribution of particle diameter observed by AFM, and the self-complementary nature of the synthesized ssDNA, it is highly probable that interactions between separately synthesized ssDNA does occur. Since the DNA nanoballs are proposed for the display of biomolecules and the sequestration of enzymatic cascades, this is not thought to present a significant problem.

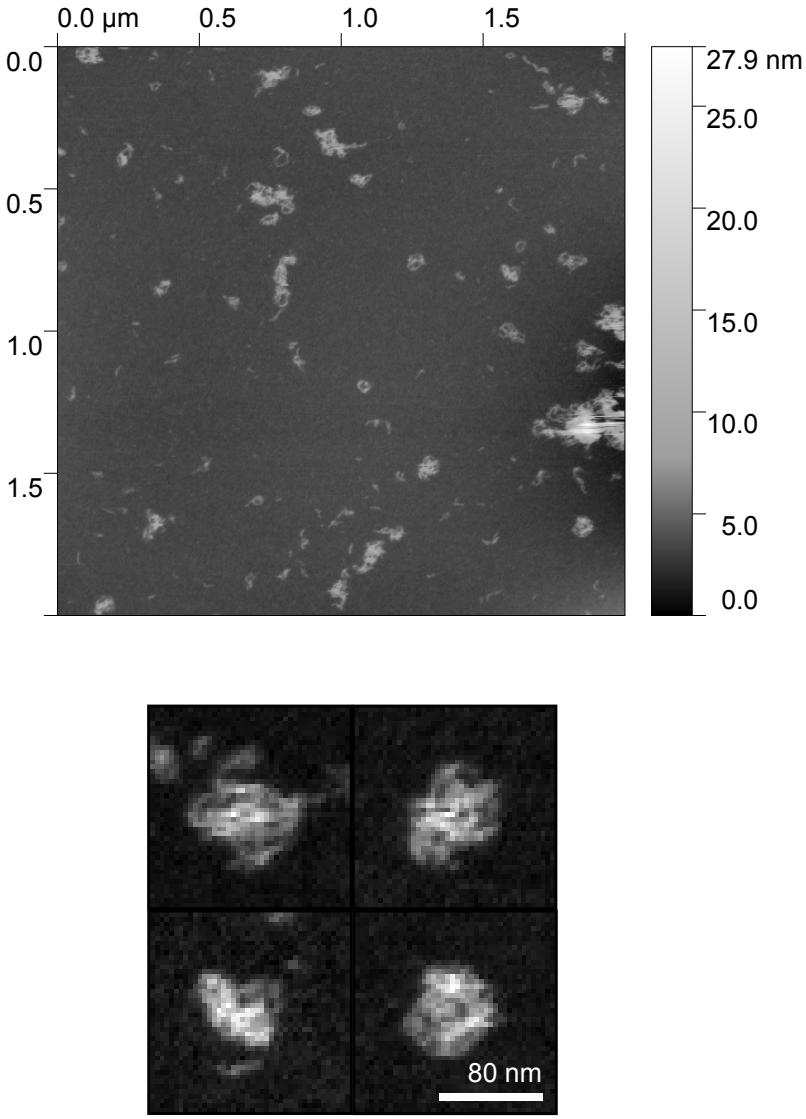

Figure 4-11 Atomic force microscopy analysis (AFM) of ϕ29 RCA synthesised DNA nanoballs after purification and reconstitution in buffer. Top: Post clean-up of DNA to remove phi29 DNA polymerase. Images were flattened, and horizontal scarring removed using Gywddion SPM analysis software and subject to no further manipulation. **Bottom:** A selection of objects observed by AFM.

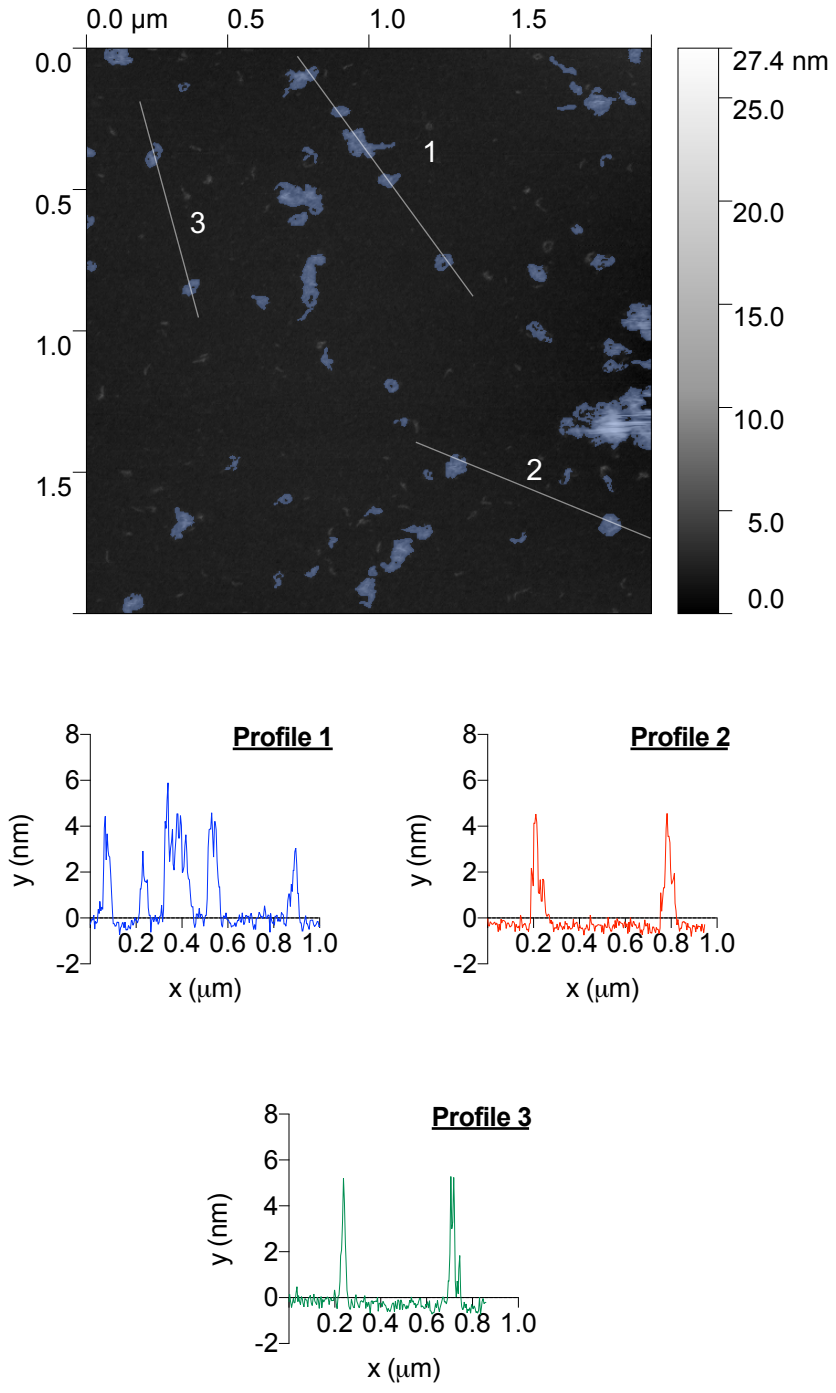

Figure 4-12 Profile analysis for a selection of sampled grains observed by atomic force microscopy. The three profiles, 1, 2 and 3 correspond to particles labelled on the AFM micrograph. The blue mask indicates the grains analysed to determine the average height and circumcircle radius for the frequency distributions displayed in figure 4-13.

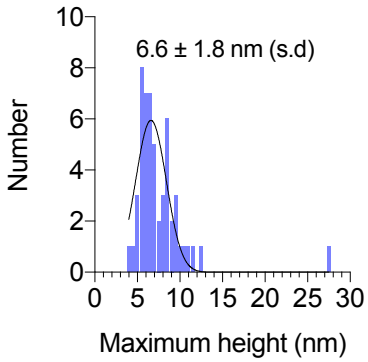

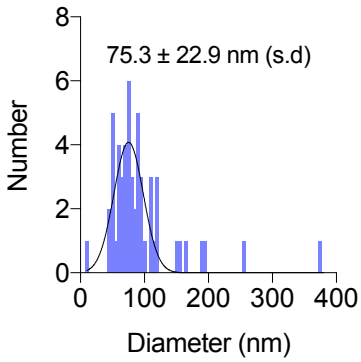

Number sampled	Maximum Height ± SD (nm)	Diameter based on circumcircle radius ± SD (nm)
54	6.6 ± 1.8	75.3 ± 22.9

Figure 4-13 Analysis of masked particles observed by AFM. The analysis of the maximum height and diameter are based on the highlighted grains shown in figure 4-12 above.

In addition to AFM, RCA products were charecterized by nanoparticle tracking analysis (NTA) to determine the hydrodynamic diameter of DNA nanoballs (figure 4-14). This technique determines the hydrodynamic radius of particles based on their visualization (the particles in suspension scatter laser light) and tracking in solution. A mean diameter of 104.7 ± 53.7 nm for the NBs (incubation time: 1 hour) is observed based on the guassian fitting to the frequency distribution, which is a higher than that derived from the particle analysis of structures by AFM (diameter = 75.3 ± 22.9 nm). This discrepancy can be explained by the limited sample size for the AFM analysis (50 particles), and differences between the measurements techniques. AFM relies on the adsorption of structures onto a surface (in this case, mica), whereas NTA measurements are conducted in solution, and does not effect the integrity of structures.

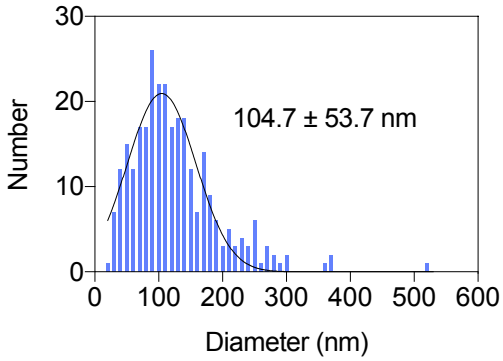

Figure 4-14 Analysis of the hydrodynamic diameter of DNA nanoballs by nanoparticle tracking analysis (NTA). The histogram was fitted with a Gaussian distribution - the average diameter observed is 104.7 ± 53.7nm s.d. (The RCA samples analysed were incubated for one hour.)

The diameter of NB structures was also monitored as a function of rolling circle amplification (RCA) incubation time using dynamic light scattering (DLS). The amplification products at 1,2 and 3 hours were analysed by DLS and are shown in figure 4-15. The hydrodynamic diameter of reaction products increases linearly with incubation time. Error bars at each time point represent the standard deviation of the mean. For amplification products at 1 hour, the mean hydrodynamic diameter is 196 ± 82 nm, based on the Gaussian fitting to the intensity distribution. This value is in greater agreement with the NTA sizing analysis, than for the diameter derived from the AFM grain analysis described in 4-12. At 2 hours, an almost 2 X increase in hydrodynamic diameter is observed, 409 ± 35 nm. At 3 hours a diameter of 1232 ± 460 nm was found, although, with quite a significant error (s.d.), given the large distribution of sizes found. DLS sizing at longer time points is particularly problematic, given the level of polydispersity expected for this sample.

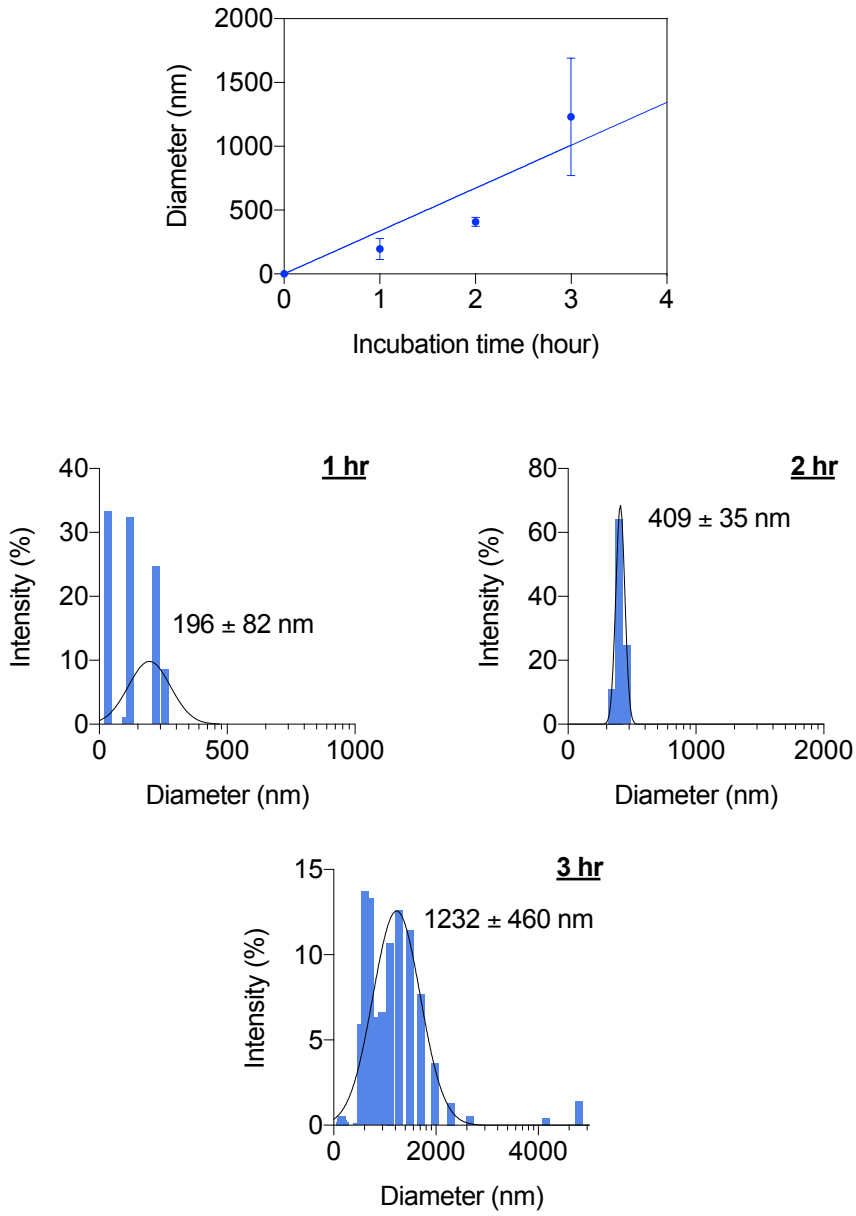

Figure 4-15 Relationship between rolling circle amplification (RCA) incubation time and the diameter of DNA nanoballs determined by dynamic light scattering (DLS). RCA reaction products at 1,2 and 3 hour time points were analysed. Errors and error bars represent the standard deviation (s.d.).

4.2.4 Conjugation of horseradish peroxidase and glucose oxidase to DNA oligonucleotide

Complementary tagged probes (cy3 and cy5 modified oligonucleotides) were hybridized to DNA NBs to determine the accessibility of the structure to complementary DNA

oligonucleotides. To prevent disruption of the DNA NB structure, the fluorescent probes were annealed isothermally at 37°C for the duration of 2 hours, to determine if immobilization at a lower T°C was feasible. This was also important in order to avoid denaturation of target enzyme-DNA conjugate at higher temperatures. Visualisation of the annealed products indicate that cy5 and cy3 labelled probes co-localise to the NB structure by the agarose gel electrophoresis (figure 4-16).

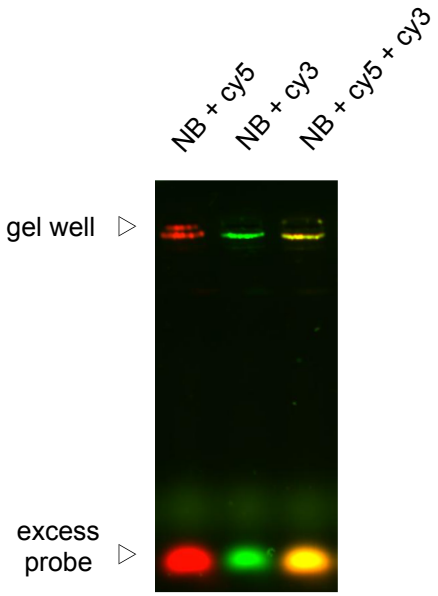

Figure 4-16 Incorporation of fluorescent cy5 and cy3 labelled DNA oligonucleotide probes to the DNA NB structure. Lane 1: Incorporation of a cy5-dna oligonucleotide only, Lane 2: Incorporation of a cy3-DNA oligonucleotide only and Lane 3: incorporation of both cy5 and cy3 labelled DNA oligonucleotides to the DNA nanoball. Running conditions: 1% agarose gel, 1 X TBE buffer.

The probes, both independently and together, are visualised within the well - this is the extent of NB migration and indicates their incorporation (excess oligonucleotide probes are visualised at the base of the well). The basis of enzyme sequestration by the DNA NB structure is through the hybridization of complementary DNA-oligonucleotides which are conjugated to a target enzyme. It is anticipated that the concatemeric nature of NB will enable the hybridization of many copies of target DNA-enzyme conjugates to form a concentrated assembly of target molecules. HRP and GOx conjugates were covalently crosslinked to a thiol modified DNA oligonucleotide (200 SH 3'TAMRA or 200 SH 3'FAM) using the heterobifunctional crosslinker sulfo-SMCC. To facilitate the identification of the conjugation products, and their hybridization to the DNA NB, the thiolated oligonucleotides were additionally modified with

a fluorescent moiety at the 3' end of the target DNA oligonucleotide (either a TAMRA-dT or Fluorescein-dT modification). The reaction products were analysed by denaturing Tris-Glycine-SDS gel electrophoresis to assess the formation of conjugated product and their migration relative to the native enzymes. Fluorescence analysis of gel separated products was also conducted, alongside the Coomassie (protein staining), to verify the addition of the fluorophore modified target oligonucleotide to the enzymes.

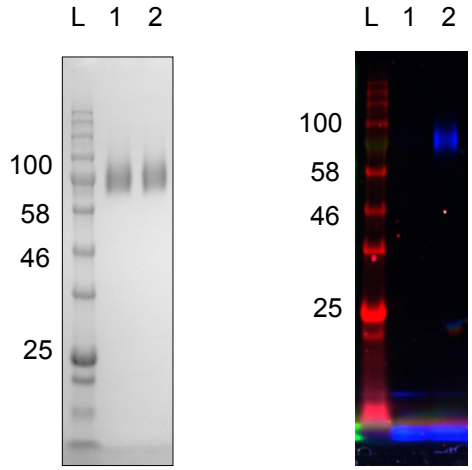

Figure 4-17 Conjugation of glucose oxidase (GOx) to a 5' thiol and FAM-dT modified DNA oligonucleotide. Analysed by 15% Tris-Glycine-SDS gel electrophoresis. Left gel: Coomassie stained gel, lane 1: unreacted GOx enzyme -crosslinker, lane 2: reacted GOx enzyme +crosslinker. Right gel: Fluorescence visualisation of the same gel, lane 1: unreacted GOx enzyme -crosslinker, lane 2: reacted GOx enzyme +crosslinker. Ladder: NEB Colour Prestained Protein Standard, Broad Range (11–245 kDa). Values for the annotated ladder are given in kDa.

For the conjugation of glucose oxidase to the thiol modified DNA oligoncleotide (200 SH 3'FAM), an upshift in migration for the enzyme is not observed by polyacrylamide gel electrophoresis, compared to the unreacted enzyme in the absence of the crosslinker (coomassie stained left gel figure 4-17). The native enzyme migrates at approximately 80kDa, which corresponds to the monomer (GOx is a dimer with a total mw of 160kDa). When visualised by coomassie protein staining (instant blue staining), no difference in migration was seen for the reacted enzyme compared to the unreacted control. However, fluorescence analysis of the reaction products indicates that the dual modified SH-fluorescent oligonucleotide is indeed coupled to the enzyme monomer (right gel figure 4-17). The degree of migration of this band (figure 4-17, right gel, lane 2) relative to the protein ladder, suggests that a single DNA

oligonucleotide is added to the GOx monomer which corresponds to the addition of approximately 7kDa, although, based on this analysis, it is not clear if the GOx enzyme is still a dimer.

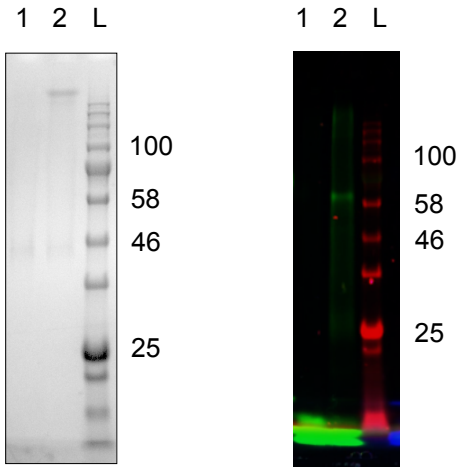

Figure 4-18 Conjugation of HRP to a 5' thiol and 3' TAMRA-dT modified DNA oligonucleotide. Products were analysed by 15% denaturing Tris-Glycine-SDS gel electrophoresis. Left gel: Coomassie stained gel, Lane 1: HRP + DNA oligonucleotide in the absence of sulfo-SMCC crosslinker. Lane 2: +crosslinker. Right gel: Fluorescence visualisation of the same gel. Ladder: NEB Colour Prestained Protein Standard, Broad Range (11–245 kDa).

A single major product is observed for the conjugation of HRP to the DNA oligonucleotide, by coomassie protein staining (figure 4-18, left gel). The native enzyme (in lane 1) migrates in line with its theoretical mass of approximately 44kDa. The molecular weight of the conjugation product suggests that it is an aggregate, as it is unlikely represent a single enzyme to which >15 target olionuleotides are covalently attached. Fluorescence visualisation of the same gel (figure 4-18, right gel), shows an additional conjugation product (right gel, lane 2 which was not apparent in the coomassie stained gel), which migrates at approximately 60kDa, adjacent to the 58kDa reference. This product corresponds to the addition two target DNA oligonucleotides to the HRP enzyme, an increase of ~14kDa in mass. The discrepancy between the fluorescence visualisation and the coomassie based staining could be explained by the mode of binding of the coomassie dye. Coomassie dyes bind proteins through ionic interactions between the sulfonic acid groups of the dye with positively charged amine groups of basic amino acids. The modification of surface accessible lysine residues with sulfo-SMCC and conjugation to the

DNA oligonucleotide, may explain the absence of this product when stained with the coomassie based dye.

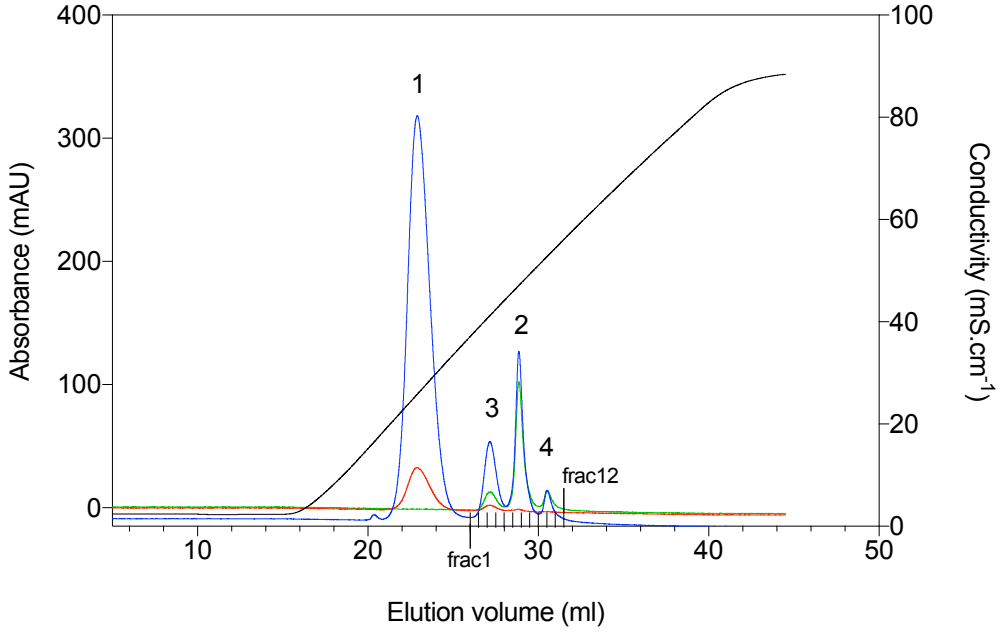

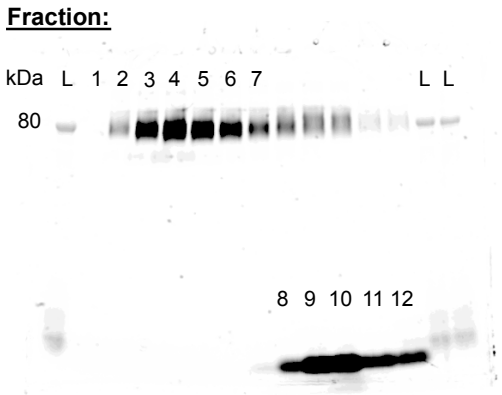

Conductivity at elution (mS/cm)	Peak identity
44.2	(1) Free GOx enzyme
49.5	(2) GOx -DNA Conjugate
49.0	(3) Free DNA oligonucleotide (reduced form)
53.0	(4) Free DNA oligonucleotide

Figure 4-19 Purification of glucose oxidase-DNA oligonucleotide conjugation products by anion exchange chromatography (AEC). Conductivity is indicated in mS/cm (black

line). Monitored at 280nm (blue line), 450nm (red), 490nm for fluorescein (green line). A total of 12 fractions were collected and analysed, fraction collection points are indicated as lines between 'frac1' and 'frac12'. Fractions were separated using a 15% tris-glycine-SDS denaturing PAGE gel. The gel shows the fluorescence visualisation of fractions. Ladder: NEB Colour Prestained Protein Standard, Broad Range (11–245 kDa).

The GOx-DNA conjugate was purified by anion exchange chromatography to remove unreacted enzyme and excess DNA oligonucleotide (figure 4-19). Anion exchange chromatography (AEC) involves the separation of molecules based on their charge, where more negatively charged species are eluted from the positively charged column under higher ionic strength. The first product (peak 1) corresponds to the native enzyme, based its absorbance at 450nm and 280nm. (The flavin adenine cofactor (FAD) of glucose oxidase absorbs at 450nm). The unreacted DNA oligonucleotide (peaks 3 and 4) correspond to the reduced and oxidised form of the thiolated target DNA oligonucleotide, based on their absorbance at 490nm for the fluorescein fluorophore. The conjugate (peak 2) is eluted between the unreacted enzyme (peak 1) and DNA oligonculeotide, due to its increase in negative charge relative to the unreacted enzyme, and absorbance at both 490nm (for fluorescein) and 450nm, which correspond to the FAD cofactor. The presence of a single peak corresponding to the DNA-enzyme conjugate, suggests that a sole product is formed for the conjugation reaction. Peak identities are summarised in the corresponding table in figure 4-19. This assignment of is also supported by the fluorescence analysis of fractions shown in figure 4-19. HRP-DNA conjugates could not be separated by anion exchange chromatorgraphy, due to the isolectric point of the HRP subtype used (pI = 8.8-9). As a result, the reaction products were serparated on the basis of their mass using a centrifugal spin filter with a MW cut off of 100 kDa with multiple salt washes, in order to retain the higher molecular weight conjugate. Alternatively cation exchange could be preformed, however, this was not attempted here.

4.2.5 Incorporation of HRP/GOx-DNA conjugates to the DNA nanoball

Enzyme conjugates were incubated in molar excess to the NB structure according to the procedure described in the previous section 2.2.3, chapter 2. The hybridization of the enzyme conjugated to the NB structure was assessed by fluorescence visualisation of the DNA nanoball by agarose gel electrophoresis (figure 4-20). Fluorescence signal co-localises to the NB structure which indicates hybridization of the HRP and GOx enzyme-DNA conjugates.

Figure 4-20 Analysis of the incorporation of fluorescently tagged DNA-enzyme conjugates to the DNA nanoball. Analysed by 1% 1 X TBE agarose gel electrophoresis. Lane 1: Both conjugates hybridized to the DNA NB. Lane 2: DNA nanoball only.

4.2.6 Activity analysis of immobilized HRP/GOx-DNA nanoballs

The reaction progress of the NB immobilized GOx/HRP conjugates was compared to free conjugates, and free enzymes, using the reduction donor ABTS, 2,2'-azino-bis(3-ethylbenzothiazoline-6-sulphonic acid). The reaction scheme is depicted in figure 4-21. The first step involves the oxidation of beta-D-glucose by glucose oxidase to yield hydrogen peroxide and gluconolactone. Gluconolactone spontaneously hydrolyses in water to produce gluconic acid. In the second step, horseradish peroxidase catalyses the oxidation of ABTS by H_2O_2. The oxidation of ABTS**,** to form the radical cation, $ABTS^{+\bullet}$, can be monitored spectrophotometrically at 405nm. The reaction rate was monitored for different starting concentrations of ABTS, at 5, 1 and 0.5mM (figure 4-22). Enzyme concentrations and reaction conditions were as described in section 2.10.1, chapter 2. The concentrations of enzyme-conjugates were determined by absorbance at 280nm, factoring the extinction coefficient of the conjugated oligonucleotide. For the comparison between conjugates +/- DNA nanoballs, this did not present a problem as the final concentration of conjugated enzymes was always equivalent. However, the conjugates could not be accurately equalized with the free enzymes. For this reason, comparisons between the free enzymes and conjugated enzymes were not made.

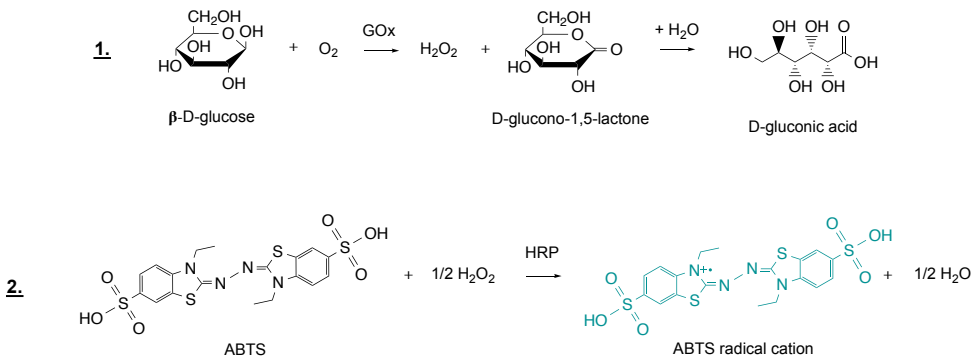

Figure 4-21 Reaction scheme for the reduction of ABTS by the GOx/HRP bi-enzyme system (1) Oxidation of β-D-glucose by glucose oxidase (GOx) to yield D-glucono-1,5-lactone and hydrogen peroxide. D-gluconolactone spontaneously hydrolyses to form D-gluconic acid **(2)** The reduction of ABTS by hydrogen peroxide, catalysed by horseradish peroxidase (HRP) to yield the $ABTS^{+\bullet}$ radical cation; which can be monitored spectrophotometrically at 405nm.

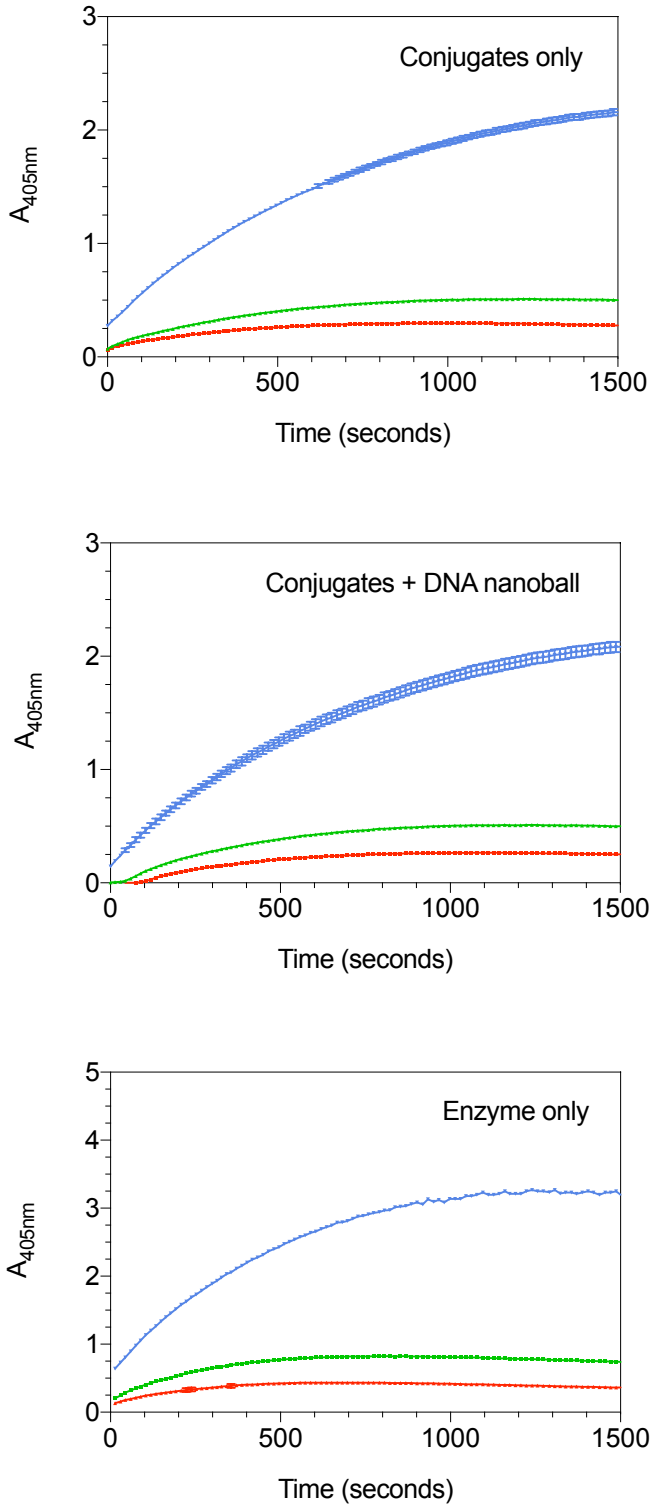

Figure 4-22 Reaction progress curves for conjugates +/- DNA NB, and free enzymes. ABTS starting concentrations: blue: 5mM, green: 1mM, red: 0.5mM. Error bars represent the standard deviation (n=3). Some error bars are too small to be seen. Reactions were conducted in 0.1M β-D-glucose, 0.1M sodium phosphate, 0.15M NaCl, pH 7.2, with ABTS at 0.5, 1 or 5mM. Data were not normalized.

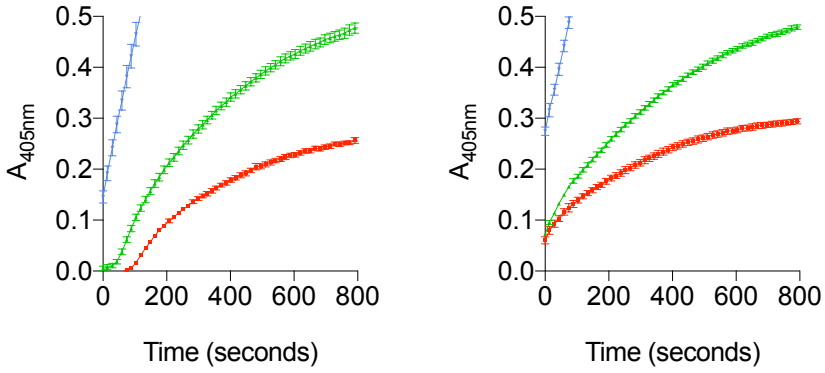

Figure 4-23 Comparison of the reaction progress between 0-800 seconds for conjugates +/- DNA nanoballs (from the reaction progress curves shown in figure 4-21 above). Each line represents a different starting ABTS concentration. Blue: 5mM, green: 1mM, red: 0.5mM.

Sequestration of the GOx/HRP cascade by the DNA nanoball does not alter the reaction progress compared to the equivalent free conjugated enzyme in the absence of the DNA nanoball structure (figure 4-22). However, a lag phase is observed for the scaffolded enzyme conjugates, but not the equivalent free conjugates or for the free enzymes. The lag phase is not observed at 5mM ABTS, however, is present at 1 and 0.5mM ABTS concentrations (figure 4-23). The duration of the lag phase is proportional to the starting ABTS concentration. At 0.5mM, the lag phase last for the duration of 88 seconds, and 43 seconds at 1mM ABTS (figure 4-23). The lag phase is a pre steady state process which could be a feature of the immobilized reaction process, or the result of other factors, such as improper mixing, inhibition of the enzymes (possibly by the DNA structure which is then relieved), or due to the time taken to reach a set reaction temperature[181]. The presence of a lag period could also suggest that the production of the intermediate (H_2O_2) by GOx, or the oxidation of ABTS by HRP, is delayed through some form of interaction with the DNA nanoball structure. Alternatively, it could be due to the time taken for substrates to diffuse into the DNA-nanoball structure, and this would suggest that the enzymes conjugates are located within the DNA structure, as opposed to being externally displayed. When comparing the initial reaction rate (figure 4-24), the DNA NB structure has no significant effect on the reaction rate for the conjugated enzymes, compared to the free conjugated enzymes (-nanoball).

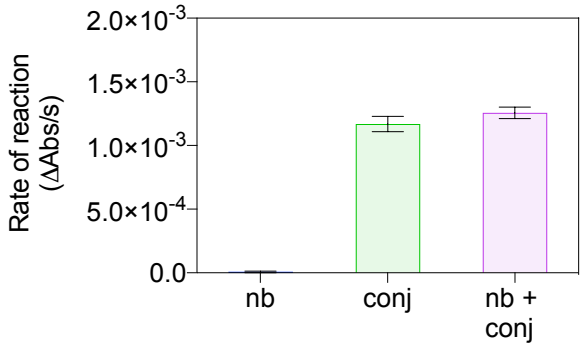

Figure 4-24 Comparison of the initial rate of reaction for conjugates +/- DNA nanoballs. NB: DNA nanoball only, conj: HRP and GOx conjugates only, nb + conj: DNA nanoball + immobilized HRP and GOx conjugates. The initial rate was determined from the tangent to the reaction progress curve extrapolated back to zero time (at 1mM ABTS). For the nb + conj configuration, the tangent to curve was determined after the duration of the lag phase. Error bars represent the standard error of the mean of the fitted initial rate to the reaction curve.

4.2.7 Probing the effect of the DNA nanoball structure on free HRP and GOx through electrostatic interactions alone

Horseradish peroxidase exists as several isozymes, whose isoelectric points range from 3-9.0[182,183]. The particular type used here, type VI, is predominantly composed of the type C isozyme which has a pI of ~9[184] (table 4-1). During the purification process, it was observed that the HRP enzyme interacts particularly strongly with the DNA oligonucleotide under non-denaturing conditions, such as during AEC. Given the pI of the isoform used, and the pH at which the reaction assays are conducted, 7.2 (well below the reported isoelectric point for HRP), it is reasonable to assume that favourable electrostatic interactions occur through the opposite charges of the enzyme and the nanoball DNA structure. For this reason, the effect of the DNA NB on the reaction catalysed by unconjugated HRP/GOx enzymes was investigated. Enzyme concentrations and reaction conditions were as described in section 2.10.1, chapter 2.

Enzyme	Molecular weight (kDa)	Isoelectric point (pI)
Glucose oxidase from *Aspergillus niger*	160 (Dimer)	4.2[185]
Peroxidase from horseradish	~44	8.8[186,187], 9[188]

Table 4-1 Properties of horseradish peroxidase and Glucose oxidase. *Horseradish peroxidase has several isoenzymes (isoenzyme catalyse the same reaction but have different amino acid sequences).

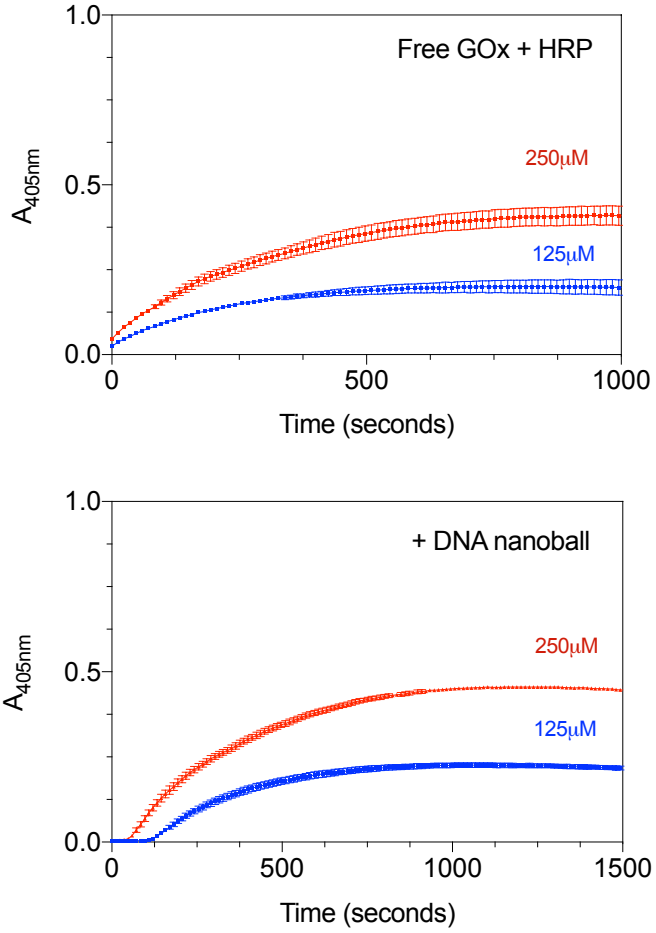

Figure 4-25 Reaction progress curves for free HRP/GOx enzymes and HRP/GOx incubated with DNA nanoballs. Two starting concentrations of ABTS are shown: red 250μM and blue 125μM. Error bars represent the standard deviation (n=3). Reactions were conducted in 0.1M β-D-glucose, 0.1M sodium phosphate, 0.15M NaCl, pH 7.2, with a starting concentration of ABTS at either 250μM and 125μM. Data were not normalized.

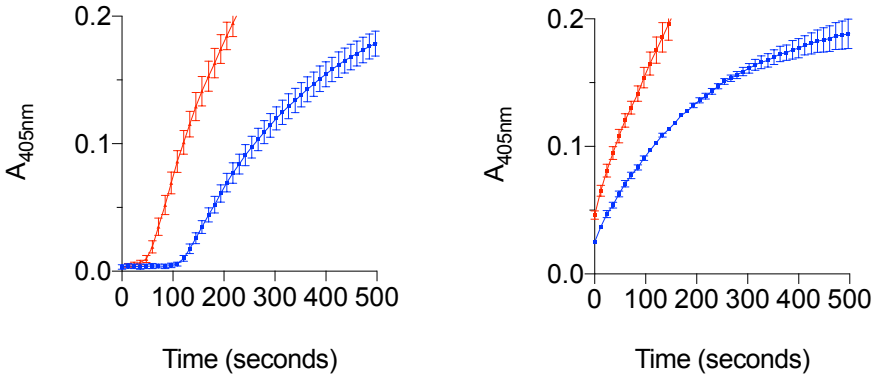

Figure 4-26 Comparison of the reaction progress between 0-500 seconds for enzymes +/- DNA nanoballs (from the reaction progress curves shown in figure 4-25 above). Red line: 250µM ABTS and blue: 125µM. Error bars represent the standard deviation (n=3).

Although the reaction progress curve and initial rate of reaction is unchanged by the presence of the DNA NB (figures 4-25 and 4-27), a lag period is observed for the reaction +NB, at both ABTS concentrations tested (figure 4-26). As observed for the conjugated forms of the enzymes, the duration of the lag period is proportional to the starting ABTS concentration, at 125µM it is ~ 50 seconds, and ~ 100 seconds at 250µM (figure 4-26). Once again, the origin of the lag phase is unclear, however, it appears to be a general feature imparted by the DNA nanoball on the HRP/GOx reaction cascade, independent of the particular immobilization method used.

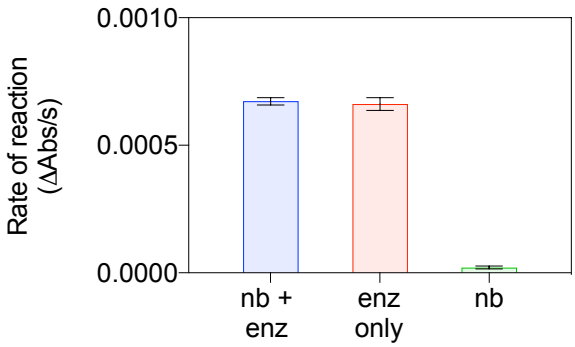

Figure 4-27 Comparison of the initial rate of reaction for HRP/GOx +/- DNA nanoballs. The initial rate was determined from the tangent to the reaction progress curve extrapolated back to zero time. For the + NB configuration, the tangent to curve was determined after the duration of the lag phase. Error bars represent the standard error of the mean of the fitted initial rate to the reaction curve.

4.3 Discussion

In this chapter, a DNA nanoball structure was investigated as a platform for the immobilization of the HRP/GOx bi-enzyme system. The NB structure was synthesised and evidenced by AFM analysis and sizing conducted by DLS and NTA, which supported the formation of compacted mesh like products. The properties of the DNA nanoball or mesh could be altered by defining secondary structure and length parameters of the starting ssDNA circular template. For example, the number of different enzymes and the extent of DNA compaction could be customised. To investigate the feasibility of enzyme immobilization, the horseradish peroxidase-glucose oxidase enzyme pair was immobilized on DNA NBs. While the conjugated forms of the HRP and GOx enzyme were prepared and incorporated on the DNA NB structure, no improvement in throughput or the initial rate of reaction was observed for the conjugated enzyme pairs + DNA NB, compared to the free conjugates. The premise of the DNA NB system was that an aggregated structural configuration could improve the processing of reaction intermediates; however, it was found that the DNA NB introduced a pre-steady state lag period, which was not observed for the equivalent enzyme conjugates in the absence of the DNA nanoball structure.

In biotechnology, it has sometimes been viewed that the immobilization of enzymes can lead to substrate channelling in a sequential cascade, and this has previously been shown for enzyme pairs displayed on DNA nanostructures, and specifically for the HRP/GOx bi-enzyme cascade. Here, the presence of a lag period (for the DNA NB + conjugates) strongly suggests that the DNA NB imparts some hindrance to the diffusion of substrates into the structure, and that the (conjugated) enzymes are located internally within the DNA-enzyme complex. Alternatively, the NB structure could prevent sufficient mixing, or result in the inhibition of either enzyme; these explanations could also account for the presence of a lag phase compared to the equivalent conjugates in the absence of the DNA NB. In future, other conjugation strategies could be explored to better prepare and purify the DNA-enzyme conjugates. One aspect of the immobilized system which was not investigated here, is the stability of the enzyme-DNA NB structure. As it would be interesting to understand if the NB system confers longer-term stability to the immobilized cascade compared to the equivalent free enzymes or enzyme conjugates.

Chapter 5

A bi-enzyme cascade immobilized on DNA nanoballs for the synthesis of benzylisoquinoline alkaloid precursors

5.1 Introduction

Benzylisoquinoline alkaloids (BIAs) are a diverse group of secondary metabolites which are predominantly synthesised by plants[189]. These compounds are used in range of medicinal applications due to their potent pharmacological and biological activities. They include the morphinan analgesics, codeine, morphine and their derivatives[190]; antimicrobial agents such as sanguinarine; and antitussives, such as gluacine[191]. Other BIA's have been implicated in the treatment of cancer, such as noscapine - an antitumor alkaloid[192], and berberine for HIV[191]. Despite their structural diversity[10] (figure 5-1), all BIAs are synthesized through a series of enzymatic conversions that share a common upstream biosynthetic pathway. In plants, all BIAs are derived from the condensation of two tyrosine derivatives, dopamine and 4-hydroxyphenylacetaldehyde, to yield (S)-norcoclaurine by norcoclaurine synthase[189]. (S)-norcoclaurine is the central precursor for the synthesis of all BIAs in plants, where it is converted to (S)-reticuline, a key intermediate which is shared by most converging BIA subgroups[189]. Ten enzyme families are involved in the biosynthesis of BIAs, including the oxidoreductase, methyltransferase, lyase (Pictet–Spenglerase) and cytochrome P450 families[189].

In plants, BIAs tend not to accumulate to high enough levels to allow for their large-scale production. Although some BIAs can be chemically synthesised[193–195], the total chemical synthesis of BIAs is commercially unfeasible due to their molecular complexity and presence of multiple stereocentres[196,197]. For instance, the opium poppy remains the only commercial source for the production of narcotic analgesics (e.g morphine, codeine)[198]. An alternative to chemical synthesis is the use of biocatalysis or the reconstitution of BIA pathways in microbial hosts, such as *E. coli,* or yeast. Enzymatic approaches for the synthesis of BIAs have the advantage of being scalable, chemo- and enantio-selective, and are considered to be environmentally friendly as reactions are typically performed under milder conditions compared to chemical synthesis[199]. The elucidation of BIA pathways in plants have enabled their reconstitution in *E. coli*[199–202] and *S. cervisiea*[203–206]. However, enzymes belonging to BIA

pathways demonstrate a broad substrate range, and as a result, the generation of unwanted side products and low product yields[207] *in vivo* presents a major challenge to the development of BIA pathways using microbial platforms[208].

For BIA pathways reconstituted in microbial hosts, the metabolic flux through a desired pathway can be improved through a number of approaches[209,210211], such as increasing gene copy number, engineering promoter and/or ribosome binding site (RBS) strength and the temporal control of enzyme expression, to minimize the formation of non-specific products. Alternatively, pathways could be spatially arranged or compartmentalized to minimize the loss of intermediates and to reduce the interaction between competing pathways[208]. In plants, BIA enzyme pathways are highly organized with respect to their cellular and subcellular localization[212]. For instance, the transcription and localisation of BIA synthesis pathways are separated across the three cell types of the phloem for the biosynthesis of morphine in the opium poppy (*Papaver somniferum*)[212]. Similarly, the biosynthetic enzymes for the synthesis of sanguinarine, an antimicrobial alkaloid, are associated with the endoplasmic reticulum in the opium poppy[207].

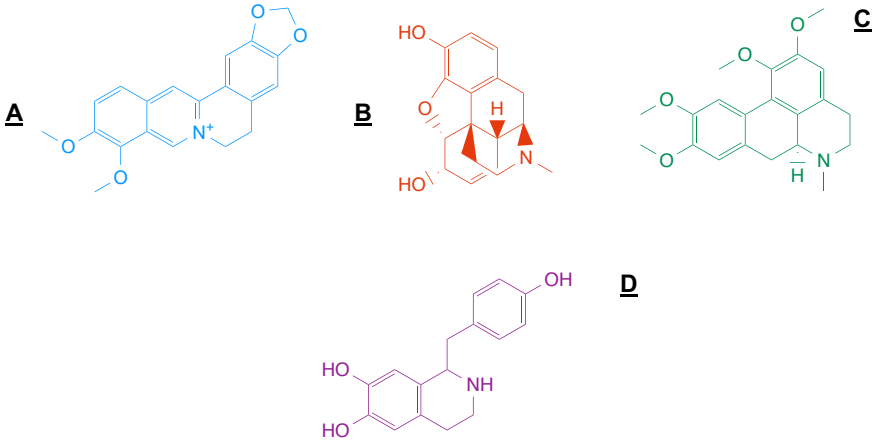

Figure 5-1 The structural diversity of benzylisoquinoline alkaloids (BIAs). Four examples of benzylisoquinoline alkaloids are shown. (A) Berberine (belonging to the protoberberine subgroup), has general antimicrobial properties. (B) morphine (morphinan subgroup). (C) Glaucine (Aporphine alkaloids), which exhibits antagonistic effects. (D) norcoclaurine (benzylisoquinoline subgroup). Over ~2500 BIA structures have been identified[189].

Scaffolding BIA pathways through the use of nanoscale structures, outside a microbial host, represents an alternative approach to the reengineering of BIA pathways, and could be employed in ways that are analogous to the specialized arrangements of BIA pathways in plants. This approach could bypass drawbacks associated with the expression and control of

biosynthetic pathways in yeast or *E. coli*. Furthermore, defined quantities or stoichiometries of target enzymes of interest could be immobilized on biomolecular systems/scaffolds directly, without concern over their temporal expression. Purification and processing steps are significantly simplified, as products can be removed directly from the physically localised or entrapped enzymes, without the need for downstream processing. This chapter describes the application of the DNA nanoball system (described in chapter 4) for the immobilization of a bi-enzyme cascade for the synthesis of benzylisoquinoline alkaloid (BIAs) precursors from a single starting product using the enzymes norcoclaurine synthase (Δ29TfNCS) and transaminase CV2025. The display of an NCS/TAm enzyme pair on a DNA nanostructure represents a novel approach to the reengineering of BIA pathways for the production of pharmaceutically products, which has so far been unexplored.

5.1.1 A transaminase and norcoclaurine synthase bi-enzyme cascade immobilized on DNA nanoballs

In this chapter, the DNA nanoball structure (described in chapter 4) was used to immobilize a bi-enzyme cascade for the synthesis of biotechnologically relevant benzylisoquionoline precursors. Here the transaminase, CV2025 (TAm) from *Chromobacterium violaceum*[213], and Δ29TfNCS norcoclaurine synthase (NCS), derived from *Thalictrum flavum* (codon optimised for expression in *E. coli*)[151], were used based on their development elsewhere[150].

The reaction cascade involves two steps (figure 5-2). First, the deamination of the starting phenethylamine substrate, either dopamine (1a) or 3-hydroxyphenethylamine (1b), by the transaminase (TAm) to form a reactive aldehyde species (2a or 2b). Pyruvate acts as the amine acceptor to yield alanine. The transaminase catalyses the transfer of an α-amino group to the alpha position of an alpha oxo-acid. In the second step, norcoclaurine synthase, a Pictet-Spenglerase, catalyses the condensation of the starting substrate (1a/b) and product (2a/b) from reaction 1 to yield product 3a/b. In this way, the reaction proceeds via a 'triangular' mechanism, in that the starting substrate and product for the first reaction are both used as substrates for the second reaction catalysed norococlaurine synthase. For the substrates dopamine and 3,4 dihydroxyphenacetylaldehyde (3-HPA), the products norlaudanosoline (3a) and 3b, are produced respectively. The reaction is depicted in figure 5-2. Norlaudanosoline is a versatile precursor for the synthesis of various BIAs[199,201,202,204,214], including endogenous morphine in mammalian cells[215–217]. Through three subsequent enzymatic conversions it can be converted to (S)-reticuline, the key branch point precursor for the synthesis of most BIA subgroups, by the enzymes 6OMT, norcoclaurine 6-O-methyltransferase, CNMT, coclaurine N-methyltransferase and 40OMT, 30-hydroxy-N- methylcoclaurine 40-O-methyltransferase.

While almost all other reports of DNA-enzyme structures describe the display of a handful of model systems (most commonly the HRP/GOx and glucose-6-phosphate dehydrogenase/malate dehydrogenase pairs) there are few examples of enzyme cascades of biotechnological relevance displayed on rationally designed DNA based structures. The complexity and range of synthesized products make BIA biosynthesis pathways interesting targets for the display, organization and control of product conversion using rationally designed DNA structures. More complex BIA synthesis cascades could, in principle, be immobilized on DNA nanoballs through the use of multiple orthogonal enzyme-DNA conjugates to localise cascades on NB structures.

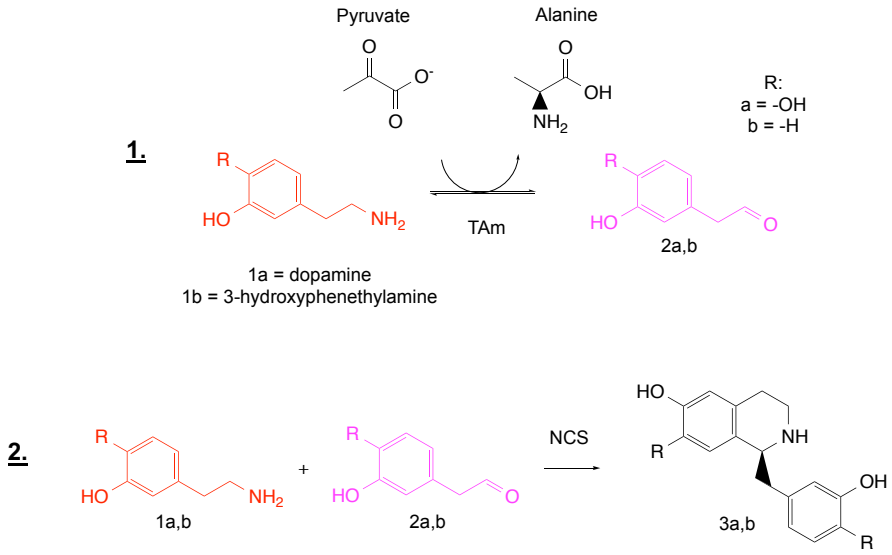

Figure 5-2 Outline of the transaminase and norcoclaurine synthase bi-enzyme cascade. **(1)** Depicts the conversion of 1b or 1a to 3,4-dihydroxyphenylacetaldehyde (2a) or 2(3-hydroxyphenyl)ethylamine (2b), with the amination of pyruvate to alanine. **(2)** The condensation of 1a + 1b or 2a + 2b by norcoclaurine synthase (NCS). The reaction proceeds via a 'triangular' mechanism, since the starting substrate and product from reaction 1 are both used as substrates for the subsequent reaction catalysed by NCS in step 2. 3a = norlaudanosoline, 3b = 1-(3-hydroxybenzyl)-1,2,3,4-tetrahydroisoquinolin-6-ol.

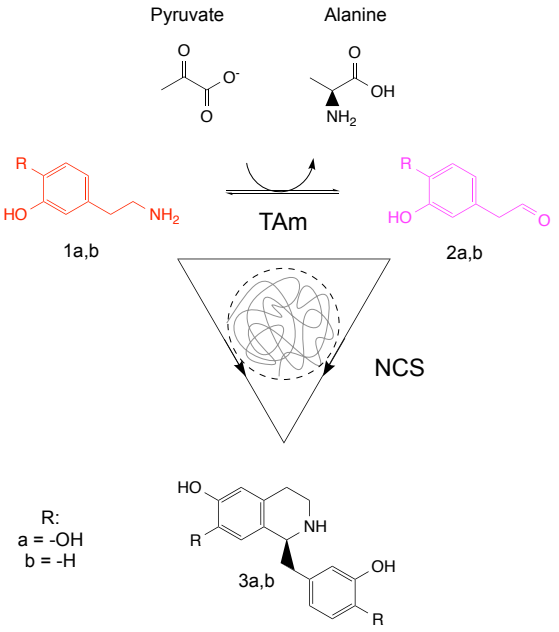

Figure 5-3 Outline of the transaminase and norcoclaurine synthase bi-enzyme cascade immobilized on a DNA nanoball. Depicts the TAm and NCS triangular cascade starting with dopamine (1a) or 3 -hydroxyphenethylamine (1b) to yield product 3a, norlaudanosoline or 3b.

5.2 Results

5.2.1 Expression of Transaminase CV2025 and Δ29TfNCS norcoclaurine synthase

His-tagged transaminase CV2025 and Δ29TfNCS norcoclaurine synthase were recombinantly expressed in *E. coli* strain BL21 (DE3) by IPTG induction. The properties of both enzymes and the expression vectors in which they were cloned are summarised in table 5-1. The his-tagged enzymes were extracted using detergent based lysis and purified by immobilized metal affinity chromatography (IMAC) using a gravity flow his-tag capture column. The purification products were electrophoresed by denaturing Tris-glycine-SDS PAGE and coomassie based (instant blue) staining to assess their molecular weight and purity (figure 5-4). Both purified enzymes migrate in line with their expected theoretical molecular weight, 21181.33 Da and 51213.42 Da for norococlaurine Δ29TfNCS and transaminase CV2025 respectively. The absence of additional products for the purification of both enzymes, suggests that a good degree of purity is obtained, which is also essential for their subsequent conjugation to carrier DNA oligonucleotides.

Enzyme	Theoretical MW (Da)	Expression vector	Origin/refs
Transaminase CV2025	51213.42	pET29a	*Chromobacterium violaceum*[213]
Δ29TfNCS Norcoclaurine synthase	21181.33	pJ411	*Thalictrum flavum*[151]

Table 5-1 Summary of the properties of transaminase CV2025 (TAm) and Δ29TfNCS norococlaurine synthase (NCS) enzymes used in this chapter.

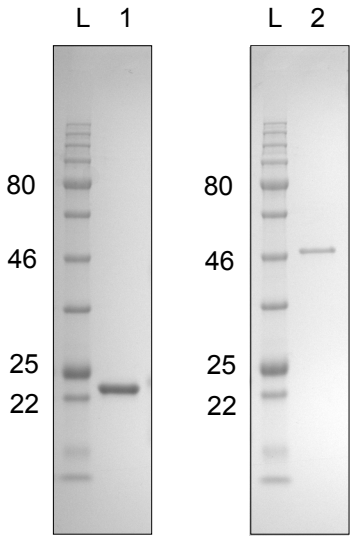

Figure 5-4 Analysis of purified norcoclaurine synthase and transaminase enzymes by denaturing Tris-glycine-SDS PAGE. Left gel Lane 1: Purified Δ29TfNCS Norcoclaurine synthase. Right gel Lane 2: purified transaminase CV2025 TAm. Ladder: NEB Colour Prestained Protein Standard, Broad Range (11–245 kDa) for both gels.

5.2.2 Conjugation of TAm and NCS enzymes to carrier DNA oligonucleotides

Both enzymes were covalently conjugated to a carrier DNA oligonucleotide (200 SH Cy5, MW: 7166 Da) through a thiol to amine coupling strategy using the heterobifunctional crosslinker sulfo-SMCC (as outlined in the previous chapter). The analysis of the conjugation products for TAm and NCS by denaturing SDS-PAGE, is shown in figures 5-5 and 5-6 respectively. For the conjugation of TAm (figure 5-5) multiple higher molecular weight

products are observed for the reacted sample (+crosslinker, lane 2) which indicate covalent conjugation to the carrier oligonucleotide (200 SH Cy5, MW: 7166 Da). A major product at ~ 50kDa which migrates above the native enzyme, corresponds to the addition of a single DNA oligonucleotide to TAm. Three further products, which migrate at approximately 100, 150 and 200 kDa, are also observed. The molecular weight of these products suggests that they are multimers of a single DNA-enzyme conjugate unit (forming a dimer, trimer and tetramer), potentially through non-covalent interactions between the DNA component.

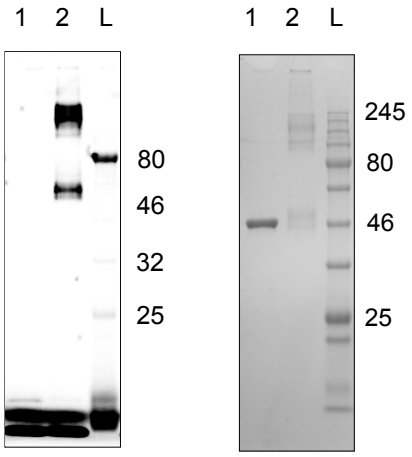

Figure 5-5 Conjugation of TAm enzymes to carrier nanoball DNA oligonucleotides, analysed by denaturing tris-glycine-SDS gel electrophoresis. Left gel: fluorescence visualisation of reaction products. Lane 1: Transaminase CV2025 (TAm) -crosslinker; Lane 2: TAm-DNA conjugation reaction products. **Right gel:** coomassie staining. Lane 1: Transaminase CV2025 (TAm) -crosslinker; Lane 2: TAm - DNA conjugation reaction products. Ladder: NEB Colour Prestained Protein Standard, Broad Range (11–245 kDa). The values given for the annotated ladder are in kDa.

It is unlikely that these higher mw products represent a single enzyme multiply modified with the target DNA oligonucleotide, as it would require the addition of >15 DNA oligonucleotides to a single TAm enzyme. Given TAm comprises of a total of 14 lysine residues (based on its amino acid sequence) a multiply modified product with a mw > 100kDa is unlikely to be formed, particularly as some of these residues may not be accessible for modification. Equally, lower MW products which correspond to the addition of more than a single DNA oligonucleotide, for example the addition of two or three oligonucleotides to the enzyme, are not observed which supports the view that the higher MW products (>100kDa) represent interaction or aggregation between discrete DNA-enzyme units. The oligonucleotide to which

the enzymes were conjugated was modified with a cy5 fluorophore at the 3' position to simplify identification of the reaction products. For the fluorescence visualised gel, the conjugation products display the same pattern of migration compared to the coomassie stained gel, and further supports the formation of covalent DNA oligonucleotide-TAm conjugates.

The conjugation of norcoclaurine synthase to the DNA oligonucleotide is shown in figure 5-6. Based on the coomassie stained gel (figure 5-6, right gel), the lowest molecular weight product migrates above the native enzyme (beneath the 25kDa marker). This product is thought to correspond to the addition of a single DNA oligonucleotide. A second major product between 46 and 32kDa markers, at approximately 40kDa, broadly corresponds to the addition of three DNA oligonucleotides to the enzyme. A spread of higher molecular weight products >100 kDa are observed, which are most likely aggregates, as they would otherwise represent an enzyme multiply conjugated with >20 oligonucleotides, which, based on the availability of surface lysine residues (14 in total based on the amino acid sequence of NCS), would not be possible.

For the same gel visualised by fluorescence imaging (figure 5-6, left gel), an additional product at approximately 30kDa is observed, which is not visualised when stained with coomassie blue (instant blue) stain. The remaining products for the conjugation of NCS are identical to those observed by coomassie staining. The additional band, observed under fluorescence visualisation of the gel, migrates in agreement with the addition of at least two DNA oligonucleotides to the enzyme (the band migrates at approximately 30 kDa) and represents the majority of the products formed based on its intensity. The discrepancy between the fluorescence visualisation and coomassie staining of the conjugation products by denaturing PAGE, could be explained by the mode of binding of the coomassie dye. Coomassie dyes bind proteins through ionic interactions between sulfonic acid groups of the dye with positively charged amine groups of basic amino acids (primarily arginine, lysine and histidine). The modification of the amine group of surface accessible lysine residues, through the reaction with sulfo-SMCC and conjugation to the DNA oligonucleotide, may explain the absence of this product when stained with the coomassie based dye. Alternatively, this band could represent a DNA-DNA conjugated product, which could account for its greater fluorescence intensity compared to the coomassie staining. To further probe the identity of this band, the conjugation products could be stained with alternative dyes, such as for DNA (e.g. EtBr or SYBR) or using a multipurpose dye such as stains-all (which stains both protein and DNA), but this was not attempted here.

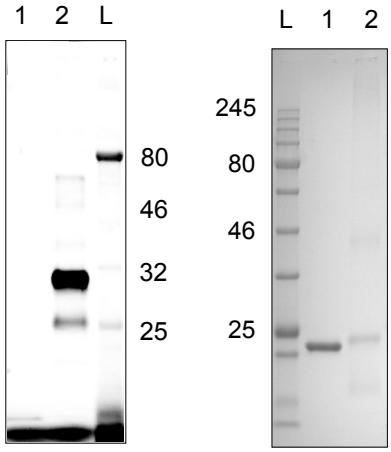

Figure 5-6 Analysis of NCS-DNA conjugation reaction products by denaturing tris-glycine-SDS gel electrophoresis. Left gel: fluorescence visualisation. Lane 1: NCS enzyme unconjugated; lane 2: NCS-DNA oligonucleotide conjugation products. **Right gel:** coomassie staining. Lane 1: NCS enzyme unconjugated; lane 2: NCS-DNA oligonucleotide conjugation products. Electrophoresed on a 15% pre-cast bio rad gel, tris glycine running buffer. Ladder: NEB Colour Prestained Protein Standard, Broad Range (11–245 kDa). The values given for the annotated ladder are in kDa.

5.2.3 Analysis and purification of TAm and NCS enzyme-DNA oligonucleotide conjugates by anion exchange chromatography

Transaminase and norcoclaurine synthase DNA conjugates were purified by anion exchange chromatography (figures 5-7 and 5-8). For the separation of TAm reaction products, four major peaks are observed (Figure 5-7). Excess target oligonucleotide elutes as the last two peaks (peaks 3 and 4), this assignment is based on the 260:280nm ratio of these peaks and their point of elution (they elute last). Also, these products are eluted at identical conductivities for both TAm/NCS enzymes chromatograms. The presence of two, rather than a single peak corresponding to the DNA oligonucleotide, can be attributed to the presence of both the reduced and oxidised forms of the thiolated DNA oligonucleotide. The unreacted protein corresponds with the 280:260nm absorbance ratio of peak 1. The additional peak (peak 3) corresponds to the enzyme-DNA conjugate based on its increased retention time relative to the unreacted enzyme (which indicates a greater overall negative charge) and the 260:280nm absorbance ratio of almost 1:1, which is consistent with that of the DNA-enzyme conjugate.

Fractions collected from the AEC separation were electrophoresed by denaturing polyacrylamide gel electrophoresis and visualised by fluorescence imaging (this allows

identification of both the DNA oligonucleotide and conjugation products on the same gel). The analysis of fractions by PAGE are consistent with the assignments made for the chromatogram peaks (given in the table in figure 5-7). For the conjugation product (peak 2) all products observed for the conjugate are eluted within this single peak, with no separation between higher and lower molecular weight products. The elution of products is consistent with the view that the higher molecular weight products represent multimers of the DNA-enzyme conjugate, rather than a multiply modified enzyme. Fractions 3 and 4 correspond to the unreacted DNA oligonucleotide which migrate at the base of the gel beneath the bromophenol blue dye front. The unreacted enzyme (peak 1) is absent as it does not incorporate the fluorophore (located on the target DNA molecule).

For the separation of the NCS-DNA oligonucleotide conjugates, four products are observed by AEC (figure 5-7). Excess unconjugated enzyme is resolved as two peaks (peak 1),and is supported by the 280:260nm absorbance ratio of this peak which is consistent with that of a pure protein. Peaks 3 and 4 correspond to the unreacted oligonucleotide and elute at the same conductivity as that seen for the separation of the TAm-DNA conjugates. A further product (peak 2), corresponds to the conjugated NCS enzyme, which is also supported by the analysis of this fraction by denaturing polyacrylamide gel electrophoresis and the increased retention time of the product relative to the unreacted protein. Similarly, for the conjugation of TAm, the entire range of conjugation products (at all molecular weights) elute within the same fractions. Again, this observation supports the view that these higher molecular weight products (>100 kDa) represent multimers of the main conjugated product, rather than an enzyme multiply modified with the target DNA oligonucleotide.

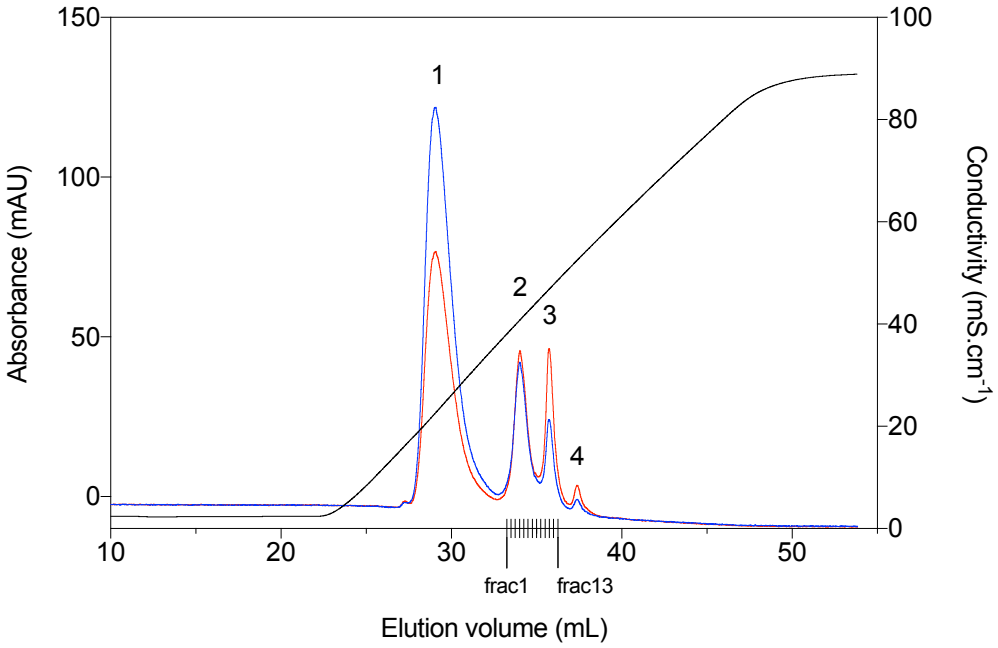

Fraction:

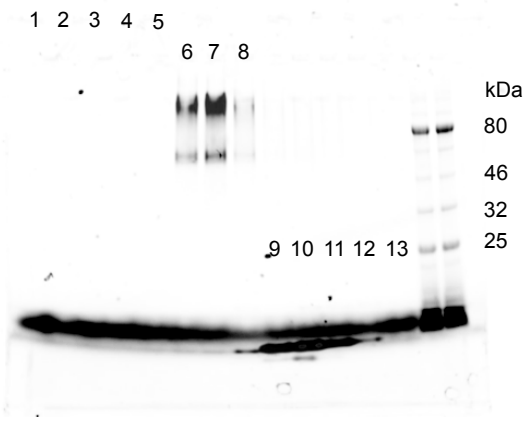

Conductivity atelution (mS/cm)	Peak identity
26.4	(1) Free TAm enzyme
43.4	(2) Tam-DNA conjugate
49.5	(3) Free DNA (reduced form)
53.1	(4) Free DNA

Figure 5-7 Separation of TAm-DNA oligonucleotide conjugation products by anion exchange chromatography (AEC). For the AEC chromatogram, blue line: absorbance at 280nm, Red line: Absorbance at 260nm, black line: conductivity (mS/cm). The gel shows the analysis of fractions 1-13 (15% tris-glycine-SDS denaturing PAGE). Ladder: NEB Colour Prestained Protein Standard, Broad Range (11–245 kDa).

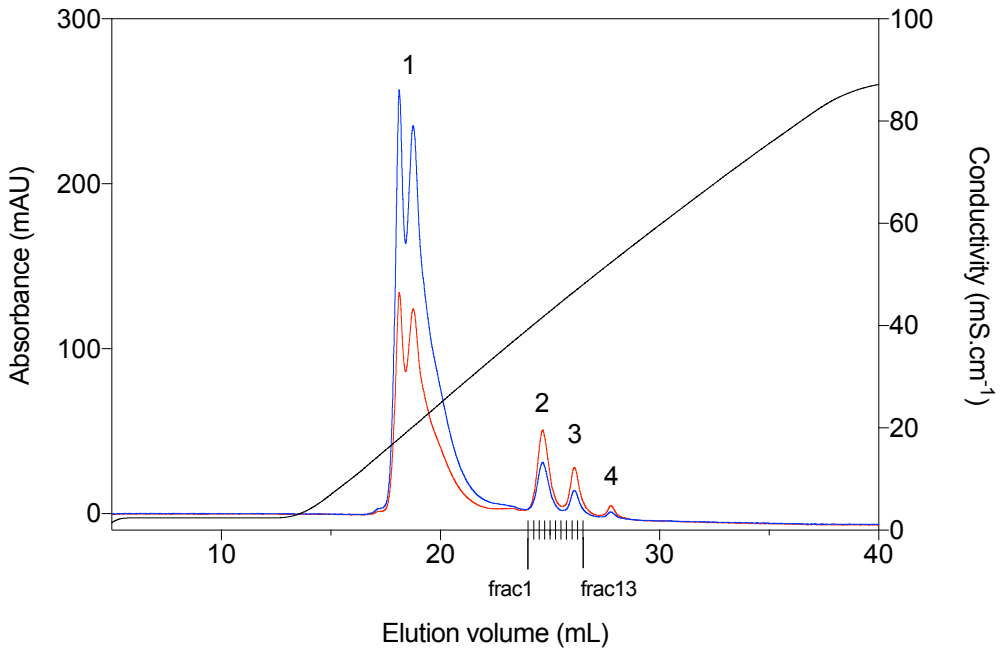

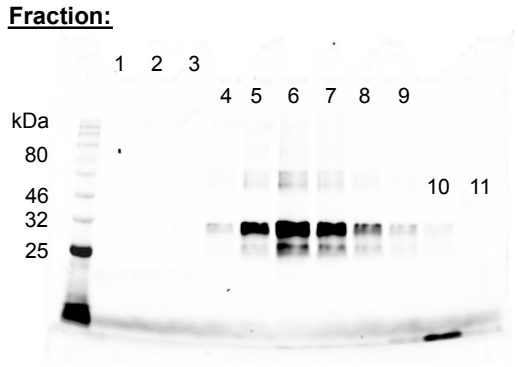

Conductivity at elution (mS/cm)	Peak identity
44.2	(1) Free NCS enzyme
49.5	(2) NCS-DNA conjugates
49.5	(3) Free DNA (reduced form)
53.0	(4) Free DNA

Figure 5-8 Separation of norococlaurine synthase-DNA conjugation reaction products by anion exchange chromatography. Analysis of norcoclaurine oligonucleotide conjugation reaction products by anion exchange chromatography. Blue line: absorbance at 280nm. Red line: 260nm. black is the measured conductivity (mS/cm), from 2.4 to 88.8 (0-100% Elution buffer). The gel shows the analysis of fractions 1-13 by 15% tris-glycine-SDS denaturing PAGE. Ladder: NEB Colour Prestained Protein Standard, Broad Range (11–245 kDa).

5.2.4 Preparation of DNA nanoballs for the immobilization of TAm and NCS enzymes

The scaffold structure used to immobilize the TAm/NCS cascade was prepared as outlined in chapter 4, by phi29 rolling circle amplification. The 200-mer starting template, comprising of the same hybridization regions for the capture of DNA-enzyme conjugates was used. As outlined in the previous chapter, the DNA nanoball and purified transaminase and norcoclaurine synthase enzyme conjugates were incubated together isothermally to promote hybridization of the conjugates to the NB structure. A single DNA oligonucleotide (200 SH Cy5, MW: 7166 Da for a single binding site) was conjugated to both enzymes, in order to simplify the process of characterizing both TAm and NCS DNA conjugates. Note, two separate carrier oligonucleotides were used in chapter 4 for the HRP/GOx pair (which would hybridize to two separate sites on the concatemeric DNA NB structure).

5.2.5 Conversion of dopamine and 3-hydroxyphenethylamine by TAm/NCS enzymes immobilized on DNA nanoballs

The conversion of dopamine (1a) and 3-hydroxphenethylamine (1b), by the NB-TAm/NCS complex was compared with the free conjugates, to assess the effect of sequestration of the enzyme pair on reaction throughput and to determine if enzyme activity is retained after conjugation to the carrier DNA oligonucleotides. Product conversion was analysed by reverse phase HPLC. For the conversion of dopamine (1a), shown in figure 5-9, the product (3a) is eluted at 10 minutes (peak 3); a further two peaks, 1 and 2, correspond to the preservative ascorbic acid and starting substrate dopamine respectively. Product conversion by conjugates immobilized on the DNA nanoball is comparable to that of the free conjugates (in the absence of the NB structure) based on the depletion of the starting substrate (table 5-2). Equally, for the second starting substrate investigated, 3-hydroxyphenethylamine (1b) shown in figure 5-10, no appreciable difference in product yield is observed for the TAm and NCS conjugates sequestered on the DNA nanoball compared to the free conjugates. The product 3b (peak 3), elutes at approximately 15.2 minutes and the starting substrate 3-HPA at 4.9 minutes (peak 2).

Product conversion for the free enzymes was also analysed (green line in both figures 5-9 and 5-10), although the quantities of enzymes could not be accurately equalized with the conjugated enzyme pairs. Under these reaction conditions, product conversion by the free enzymes was markedly greater for dopamine than for 3-HPA, based on the depletion of the starting substrate (table 5-2). However, for the scaffolded conjugated enzymes (+DNA nanoball), greater product conversion was observed for 3-HPA than for dopamine. For the free conjugates only, the % conversion for both starting substrates is broadly equivalent.

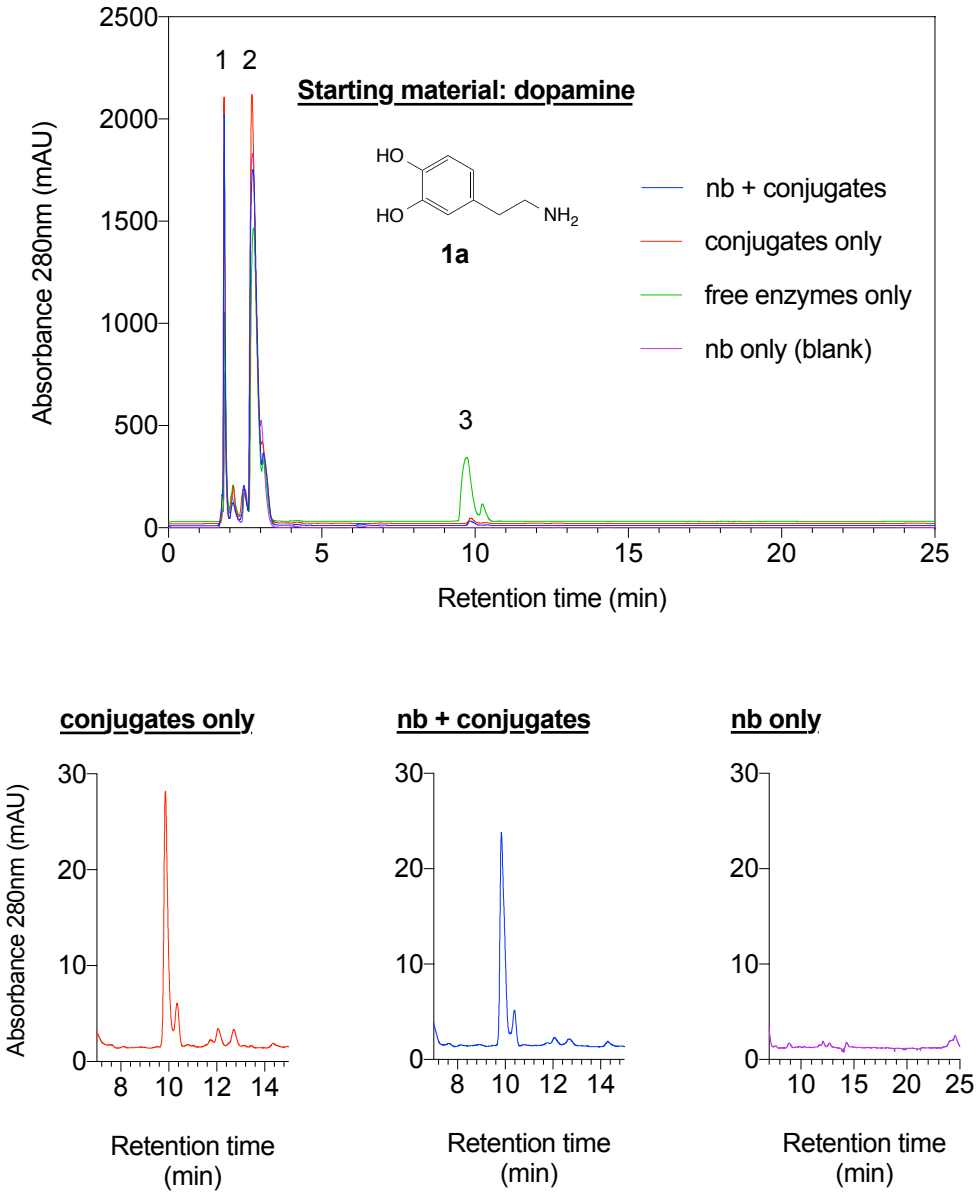

Figure 5-9 Analysis of product conversion by RP-HPLC, starting substrate: dopamine (1a). Showing the reaction products for the free transaminase and norcoclaurine synthase enzymes (green), conjugated enzymes only (red), conjugated enzymes + DNA nanoball (blue) and nanoball DNA only (purple). Comparisons of the product peak (3) are shown below for the conjugates +/- nanoballs and nanoballs only.

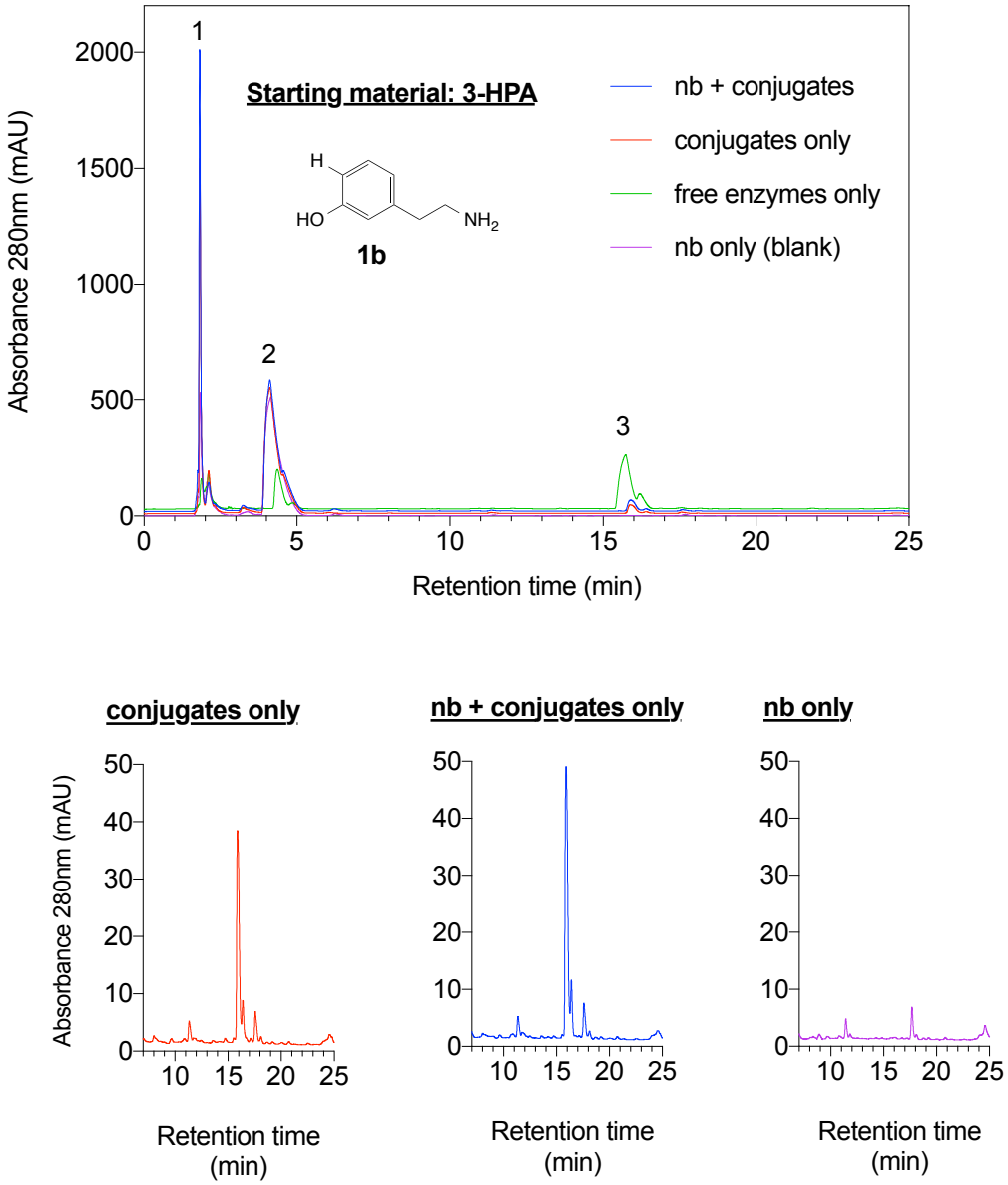

Figure 5-10 Analysis of product conversion by RP-HPLC, starting substrate: 3-hydroxyphenethylamine (1b). Showing the reaction products for the free transaminase and norcoclaurine synthase enzymes (green), conjugated enzymes only (red), conjugated enzymes + DNA nanoball (blue) and nanoball DNA only (purple). Comparisons of the product peak (3) are shown below for the conjugates +/- nanoballs and nanoballs only.

Configuration	% Conversion (Starting material Dopamine)	% Conversion (Starting material 3-HPA)
Free TAm & NCS	82.8	32.7
Conjugate TAm & NCS only	9.5	8.5
Conjugates + DNA nanoball	5.6	10.5
Nanoball scaffold only (blank)	0	0

Table 5-2 Analysis of % product conversion based on the depletion of starting material (dopamine or 3-hydroxyphenethylamine). Product conversion was calculated based on the reduction in the area of the starting substrate peak. The area of peaks (mAU*min) was calculated using the Chromeleon 7.2 chromatographic software. The values shown in the table were derived from the HPLC chromatograms shown in figures 5-9 and 5-10, for dopamine and 3-HPA respectively.

5.2.6 Verification of products by electrospray ionization mass spectrometry

The identity of products from both starting substrates was confirmed by electrospray ionization mass spectrometry (ESI-MS) (figure 5-11). Both products, for dopamine and 3-HPA conversions, match the theoretical masses for the expected products, norlaudanosoline (3a) and 1-(3-hydroxybenzyl)-1,2,3,4-tetrahydroisoquinolin-6-ol (3b). For dopamine, the expected product norlaudanosline is observed across all reactions in agreement with its expected mass (theoretical: 288.12, observed: 288.124). For the conversion of 3-HPA, an additional product (mass: 238.1 Da) is also found by ESI MS, in addition to the expected product 3b (theoretical: 256.13 Da, experimental: 256.13). The difference in mass (16 Da) may represent the substitution of a hydroxyl group -OH for -H.

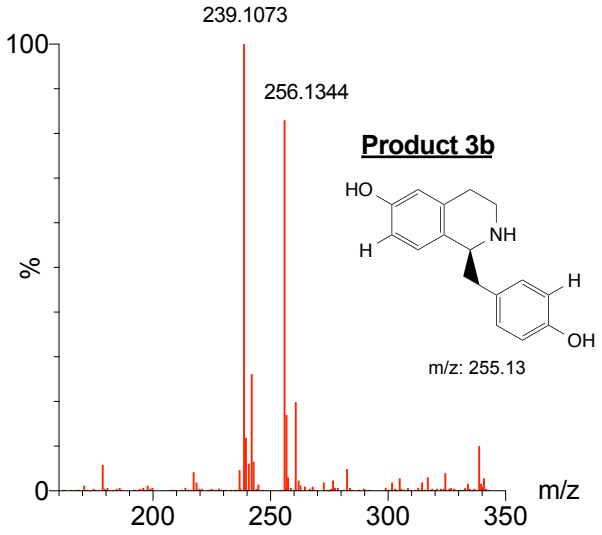

Expected theoretical mass $(m/z + H)^+$	256.1338
Experimental $(m/z + H)^+$	256.1344,239.1073

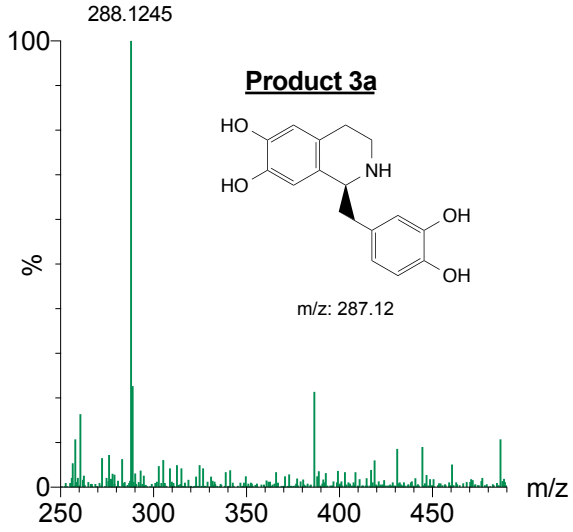

Expected theoretical mass $(m/z + H)^+$	288.12
Experimental $(m/z + H)^+$	288.124

Figure 5-11 Verification of TAm/NCS products by electrospray ionization mass spectrometry (ESI-MS) for starting substrates: 3-hydroxyphenethylamine (top) and dopamine (bottom). Theoretical and expected masses for both products are given in the corresponding tables.

5.3 Discussion

In this chapter, DNA NBs were investigated for the immobilization of a transaminase and norcoclaurine synthase bi-enzyme cascade for the synthesis of biotechnologically relevant benzylisoqunioline alkaloid precursors (products 3a and 3b). Conjugated TAm and NCS enzymes were constructed, characterized and immobilized on DNA nanoball structures, which is evidence of the applicability of this system to a range of enzyme cascades. Based on RP-HPLC analysis of product conversion, the immobilization of TAm and NCS conjugates to the NB structure was not found to significantly effect substrate conversion compared to the equivalent free conjugates, for both starting substrates (dopamine and 3-HPA). For the free enzymes, the % conversion for dopamine was found to be greater than 3-HPA based on the depletion of the starting substrate by RP-HPLC. However, for the conjugated enzymes (+/- DNA NB) the % conversion for 3-HPA compared to dopamine was more equal. This observation could suggest that the covalent modification of the enzyme pair to the carrier DNA oligonucleotide, confers changes to their substrate specificities.

A key challenge in this chapter was the preparation of DNA enzyme conjugates. As discussed, the identities of the conjugation reaction products were not always clear, and this was particularly true for the NCS enzyme (figure 5-6). Several alternative coupling approaches could be used for the preparation of enzyme conjugates, with more predictable stoichiometries and higher product yield. For example, through genetic fusions, such as the SNAP-tag system. This particular approach involves the fusion of 20kDa mutant of the DNA repair protein O^6-alkylguanine-DNA alkyltransferase to a target protein, which reacts specifically with a benzylguanine derivative (which can be introduced on the target DNA oligonucleotide). Alternatively, non-covalent interactions between the NB structure and target protein could be used to circumvent covalent modification of the protein. One approach involves the nitrilotriacetic acid (NTA)-poly histidine interaction. For example, it has been shown that three or four NTA moieties (tris- and tetrakis-NTA) demonstrate sufficiently high affinity towards hexahistidine tagged proteins[76]. Coupled with the concatemeric nature of the NB, the concentration of multiple NTA moieties on a single NB particle could represent a viable strategy for the capture and display of target poly histidine tagged proteins. While it has been shown that complementary DNA oligonucleotides and DNA-enzyme conjugates can hybridize to the DNA NB structure, based on the fluorescence analysis of reporter probes and conjugates, the extent of their incorporation was not investigated in detail. Since the premise for the use of the NB structure is that it enables the sequestration of target protein molecules, further analysis is necessary to understand the nature of the interaction between the NB structure and target

conjugate molecules. Analysis by atomic force microscopy, for instance, could give a clearer indication of the uptake and display of the conjugate molecules to the NB structure.

Chapter 6

A DNA structure powered by enzymatic catalysis

6.1 Introduction

6.1.1 Motion on the nanoscale

The control of motion on the nanoscale and the design of autonomous nano or micromotors are emerging research areas in the nanosciences[218,219], driven by applications in directed transport and in nanomedicine[218–221]. Molecular motion is an essential feature of biological systems for intracellular transport and response to external stimuli. On the molecular level, mechanochemical enzymes, such as the motor proteins and rotary biomotors, transform chemical energy into mechanical work or directional movement[222]. The dynamics of motion on the nano or microscales differs from that on the macroscale[223], for micro and nanoscale objects, viscous rather than inertial forces dominate - these objects are said to be subject to forces at the low Reynolds number regime (the Reynolds number is a dimensionless parameter which is used to describe the ratio of inertial to viscous forces). The viscous force refers to a fluid's ability to resist flow, whereas inertia refers to the property of matter that causes it to resist any change in its motion [224].

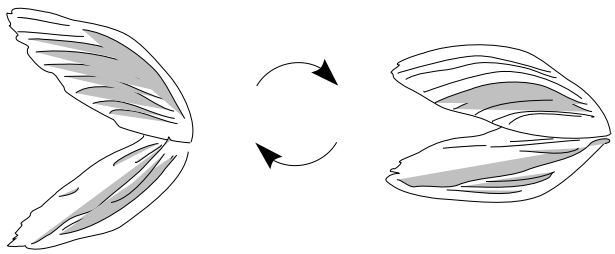

Figure 6-1 Schematic representation of the scallop theorem[223]. According to the scallop theorem, geometrically reciprocal motion cannot lead to net displacement at the nanoscale in Newtonian fluids. Reciprocal motion, like that demonstrated by the closing and opening of a scallop, as shown above, is symmetrical as it appears the same when viewed forwards or backwards in time.

To achieve propulsion or locomotion on the nanoscale, a 'swimmer' must deform in a way which is not invariant under time reversal. In other words, the movement must be non-reversible or non-symmetrical. This principle is described by the 'scallop theorem'[223], which states that to achieve propulsion at low Reynolds numbers in simple fluid (i.e Newtonian), motion must be non-symmetrical to overcome viscous drag forces. 'Symmetry' may refer to a number of different properties of the system, for example, the particle composition, shape or the distribution of the catalysing surface reactions[225]. For instance, a back and forth displacement with time, such as that of the opening and closing of a scallop (figure 6-1), cannot achieve directed motion at low Reynolds number[226]. Microorganisms employ this principle to achieve locomotion or taxis at the microscale, through the use of non-reciprocal movements. For example, the bacterial flagella is propelled by an asymmetrical rotating helical motion [227,228], as well as cillia, which demonstrate an asymmetric back and forth displacement (figure 6-2). Achieving directed motion on the nanoscale is further complicated by inherent forces such as Brownian motion (the random movement of molecules in solution due to thermally driven collisions with surrounding solvent molecules) and other surface phenomena[229]. To date, several synthetic micro or nanoscale motors have been described[148]. Broadly, these devices rely on two major approaches to achieve directed motion, or enhanced diffusive motion. First, motion that is powered by external fields, such that they are externally powered propellers[230,231], or through the asymmetric catalytic conversion of a substrate (chemically powered nanomotors) - which could involve an enzymatic[144,146] or a metallic catalyst [145,148,229].

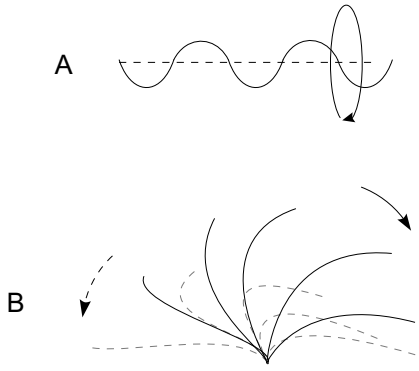

Figure 6-2 Motility at low Reynolds numbers - biological molecular motors. Demonstrate non-reciprocal motion. (A) The cork screw like motion of a bacterial flagellum. The flagella, comprising of helical filaments, undergoes a screw like motion to propagate a helical wave. The flagellum is a biological rotary motor driven by the flow of charged ions across the plasma membrane in response to environmental signals. (B) the beating pattern of cillia, the dashed represents the recovery stroke and the black line, the effective stroke. Cilia filaments move back and forth asymmetrically. This mode of

movement is employed by the protozoa *Paramecium* to achieve motion at low Reynolds numbers.

6.1.2 Biomolecular motors on the nanoscale

In biological systems, biomolecular motors involve chemical-mechanical coupling to transform chemical energy into directed mechanical movement or rotary motion. The three classes of motor protein, myosin, kinesin and dyeins covert chemical energy in the form of ATP hydrolysis into mechanical work, a process known as chemical-mechanical coupling. The motor proteins are responsible for many essential cellular processes, including the transport of subcellular cargo, such as mitochondria, golgi sacks, and membrane vesicles a across networks of polymeric microfilament tracks[232]. Other motor proteins function to induce force through the alignment or 'sliding' of cytoskeletal filaments against one another - during the process of muscle contraction (muscle myosin) and the positioning of the mitotic spindle during cell division. The motor proteins possess a catalytic domain, the 'head', which is shared among all members of the motor proteins, it possesses an ATP binding site in addition to a binding site for the association to its corresponding cytoskeletal filament. The sequential binding and hydrolysis of ATP is coupled to structural changes in the catalytic domain which enable the association and dissociation of the head domain from a corresponding microfilament track[233]. In this way, Brownian motion and viscous forces are overcome to achieve processive and directed motion through mechano-chemical cycling (figure 6-3).

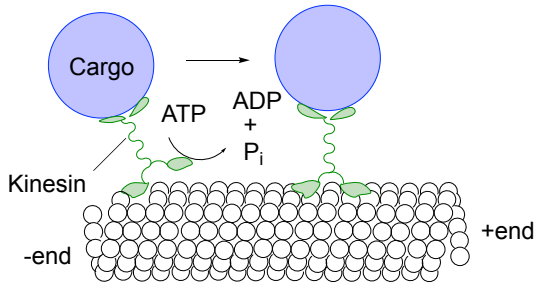

Figure 6-3 Biomolecular motors - the movement of kinesin along a microtubule. The motion of kinesin along microtubule polymer tracks for the transport of cargo intracellularly. Movement occurs through the binding and release of head domains to the microtubule filament through successive cycles of ATP hydrolysis. Motor proteins, mechanochemical enzymes, convert chemical energy, in the form of ATP hydrolysis to actuate motion along polarised cytoskeletal filaments[234].

Rotary biomotors, such as the F_0F_1-ATP synthase, are another class of mechanochemical enzymes which convert chemical energy into motion, specifically rotary movement. F_0F_1-ATP synthase is composed of two mechanical rotary motors, F_0 and F_1, which couple the electrochemical potential of a proton gradient, across the mitochondrial, chloroplast or bacterial membranes, to the synthesis of ATP from adenosine diphosphate (ADP) and inorganic phosphate (Pi) [148]. Similarly, the bacterial flagellum, which is composed of one or more long helical filaments, is driven by a membrane embedded rotary motor through the flow of Na^+ or H^+ ions across the cytoplasmic membrane[235].

6.1.3 DNA based molecular motors

DNA walkers are a form synthetic DNA nanomotor which display directed motion along a DNA or RNA track in a stepwise or 'walking' fashion. DNA based molecular motors are inspired by their natural protein analogues[236], and there are a number of mechanisms by which they achieve uni or bi directional movement[237]. The energy for this process is usually derived through a strand exchange reaction, or enzymatic modification of the DNA backbone through hydrolysis[238–241]. The processivity of the DNA walker is based on the design of biased system states[236]. Typically, the walker is hybridized to a 'track' through complementary base pairing to anchor strands. The interaction is designed such that the walker achieves a lower free energy state by hybridizing to neighbouring anchor strands, for example, through partial hybridization or toehold-mediated strand displacement[242–244]. This interaction can be disrupted with the addition of complementary oligonucleotides to the anchor strands to return the walker to its original (higher) energy state. Cycling through higher to lower energy states, achieves directed motion along a track. This has been demonstrated for a DNA walker with two feet that walks along a DNA track composed of four different anchorages[245] and other variations, such as a bi pedal walker on a DX DNA tile track[246]. Other notable examples of enzymatic driven DNA walkers or motors include a 'rolling' nanomotor (a DNA modified particle) whose motion is powered by RNase H cleavage of the DNA/RNA hybridization between the DNA-particle and an RNA modified track [247]. DNA walkers are also exploited for the directional transport of tethered cargo in ways that are analogous to the transport of molecular cargo intracellularly[248]. Although the majority of DNA based nanodevices for purpose of directed motion are in the form of DNA walkers whose movement is confined to a DNA/RNA track, it has also been shown that the motion of DNA nanodevices can be powered by external fields. For example, directed motion driven by an electric field - for the rotation of DNA six-helix bundle on an origami plate[230], and the propulsion of DNA-flagellated magnetic particles in a magnetic field[231].

6.1.4 Enzyme catalysis to power nanomachines

Recently, It has been shown that certain enzymes display enhanced diffusivity in the presence of their substrates[141–146], specifically this has been shown for the enzymes glucose oxidase, urease, catalase and alkaline phosphatase enzymes[148]. Elsewhere, it is reported that the enhanced diffusive motion of enzymes in the presence of their substrates can contribute to the assembly of enzyme cascades into metabolons (non-covalent assemblies), through chemotaxis towards their substrate[249]. This was demonstrated for the first four enzymes belonging the glycolysis cascade - hexokinase, phosphoglucose isomerase, phosphofructokinase and aldolase[249]. Presently, the basis for the enhanced diffusivity through enzyme catalysis remains unclear. Several mechanisms have been proposed, including heat generation which is thought to perturb the structure of the enzyme (chemoacoustic model)[250], through collective heating[251], stochastic swimming through conformational changes during the catalysis[252], or through self-electrophoresis, in which the enzyme moves in a self-generated electric field due to the asymmetric distribution of ions[253].

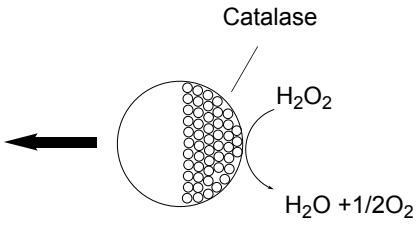

Figure 6-4 An enzyme powered Janus (mesoporous silica) nanomotor functionalized with catalase enzyme on one face[145].

By extension, it has also been shown that enzymatic catalysis can power the motion of nanoscale structures to which they are attached, as demonstrated for enzyme modified Janus inorganic particles[144,145,147] (figure 6-4), enzyme encapsulated polymersomes[254] and polymeric stomatocytes[255]. These nanodevices rely on the asymmetric distribution of catalytic conversion, which could involve the asymmetric immobilization of the target enzyme, for instance on a single face of the structure, or through an asymmetric structural design. The enzymes glucose oxidase, catalase and urease, are the most commonly described enzymes for this application, and they rely on the availability of an external substrate, the 'fuel', through the environment in which they are present. Several studies indicate that diffusivity is affected in a concentration dependent manner until saturation, and that the enhancement of diffusivity can be correlated to enzyme activity[148]. As well as approaches which rely on enzymatic catalysis, nano and micro

particles can also be driven by metallic based catalysis on nanoparticles[145]. For example, Au–Pt bimetallic 'striped' particles in hydrogen peroxide solution demonstrate directed motion, which occurs due to the asymmetric generation of protons at one end of the particle, the Pt end, which results in the movement of the negative particle in a self-generated electric field (self-electrophoresis)[256]. A similar process is also shown for Au-Pt and Au-Ni bimetallic nanorods[257].

6.1.5 Measuring the motion of nanostructures by nanoparticle tracking analysis (NTA)

In this chapter, particle motion is measured using nanoparticle tracking analysis (NTA). NTA is a method for visualising and tracking particles in solution through laser illumination (figure 6-5). Laser light is scattered by particles in solution so that they appear as point scatters moving under Brownian motion. This allows those particles to be visualised using a sCMOS camera. The motion of scattering particles is captured and recorded in order to obtain individual particle trajectories, from which the diffusion coefficient and hydrodynamic diameter of those particles can be derived[258]. Unlike dynamic light scattering (photon correlation spectroscopy), which involves the measurement of average fluctuations of scattered light over the entire sample to produce an intensity weighted distribution[259,260], NTA derives the hydrodynamic radius individually for all tracked particles to produce a high resolution number weighted distribution.

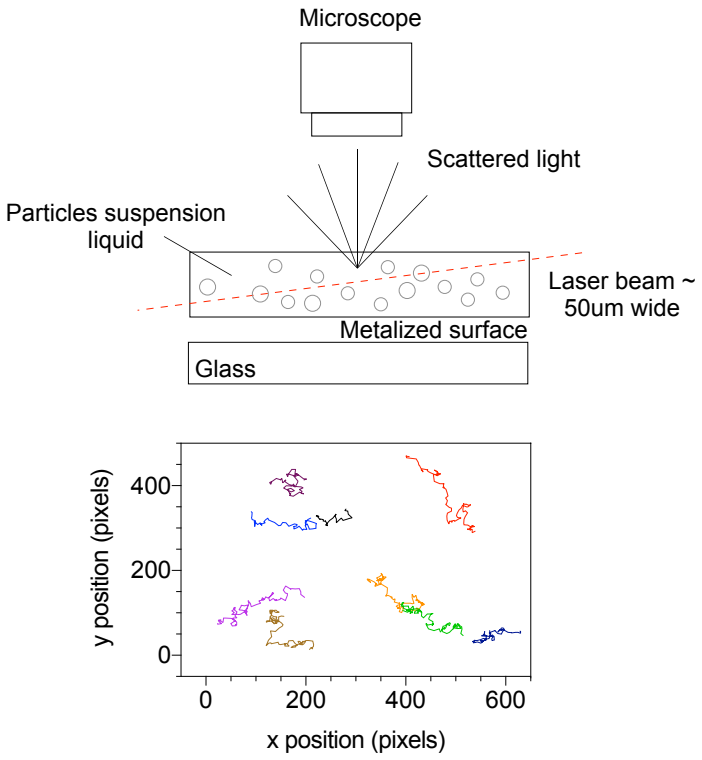

Figure 6-5 Schematic representation of nanoparticle tracking analysis (NTA). The process depicts the method for visualizing particles in liquid through laser illumination. Laser

light is scattered by particles in solution which allows those particles to be visualised using a sCMOS camera. Particle motion is recorded as a trajectory in the x and y dimensions, from which the diffusion coefficient and in turn the hydrodynamic diameter of particles can be derived through the Stokes- Einstein equation.

To determine the hydrodynamic radius or diffusion coefficient of particles, a video is captured for a specified duration, typically several seconds, during which particle trajectories by are tracked in the x and y dimension. The rate of movement is affected only by the viscosity and temperature of the liquid, and not by particle density or refractive index as is the case with DLS. The mean squared displacement (MSD) is the average distance displaced over a specified lag time. By calculating the mean squared displacement of an individual particle trajectory, the diffusion coefficient for that particle can be derived. The calculation of the mean square displacement is described by equation 1.

$$MSD\ (\tau)\ = < \Delta r(\tau)^2 > = < [r(t+\tau)\ -\ r(t)]^2 >$$

Equation 1 Mean square displacement.

For Equation 1, r(*t*) is the position (x,y) of the particle at time *t*. τ is the lag time (delta t) between the two positions of the particle used to calculate the displacement. < > represents a time-average over *t* and/or an average over several trajectories (ensemble average). For molecules undergoing simple Brownian motion, a linear relationship between the MSD and τ (the lag time) is observed. The slope of the curve is related to the diffusion coefficient through equation 2[261].

$$MSD\ (\tau)\ =\ 4D\Delta t$$

Equation 2 Relationship between the mean square displacement and the diffusion coefficient for molecules undergoing simple Brownian motion[261].

$$D = \frac{k_B T}{6\pi\eta R}$$

Equation 3 The Stokes Einstein equation. Where k_B is the Boltzmann constant, T is the temperature in K, η is the viscosity of the solution and R is the sphere equivalent radius of the particle.

The sphere equivalent hydrodynamic radius is related to the diffusion coefficient of a particle through the stokes Einstein relationship, given in equation 3[258] - this is basis of NTA for particle sizing. In this chapter, NTA is used to determine the diffusion coefficient for individually tracked particles, rather than for the purpose of sizing, to determine the effect of substrate concentration on the motion of the DNA-enzyme particle.

6.2 Results

6.2.1 Design of the DNA-lysine decarboxylase structure

The aim of this chapter is to investigate the use of enzymatic catalysis as a means of affecting the motion of a DNA nanostructure. A test DNA scaffold is outlined, which is attached to several molecules of an enzyme, lysine decarboxylase, positioned at one end of the structure in order to introduce asymmetry in the localisation of catalytic conversion. Lysine decarboxylase (L-lysine carboxy-lyase, E.C. 4.1.1.18) is a pyridoxal 5'-phosphate PLP dependent enzyme which catalyses the conversion of L-lysine to cadaverine and carbon dioxide.

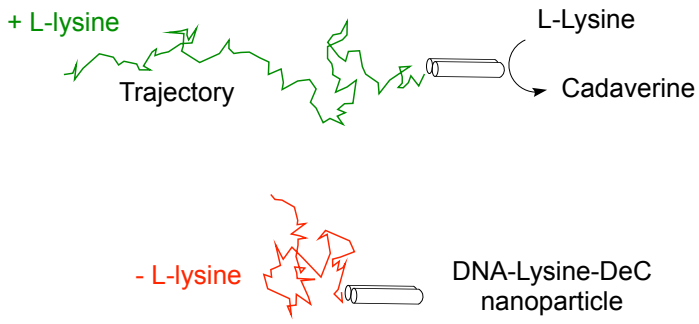

Figure 6-6 Schematic representation of the lysine decarboxylase powered DNA structure undergoing enhanced motion in the presence of its substrate L-Lysine. The enzyme-DNA particle is depicted as a duplex structure, catalysing the conversion of L-lysine to yield cadaverine and CO_2. The trajectory for the structure in the presence of substrate (+lysine) demonstrates enhanced motion and/or a directed movement due the reaction catalysed by lysine decarboxylase (in green). In the absence of substrate, the trajectory is depicted in red.

The lysine decarboxylase-DNA structure is assembled using a ssDNA scaffold which is folded to form a duplex structure using a series of double crossovers along the length of the ssDNA (figure 6-7). The docking loop, to which conjugates are annealed, remains unstructured to maintain an asymmetric localisation of catalytic conversion. The scaffold ssDNA is derived from the phagemid pBluescript II SK (-). Multiple enzyme molecules are incorporated at one

end of the structure through DNA-enzyme conjugates of lysine decarboxylase, which are recruited to the through sequence specific hybridization to the to capture DNA oligos (a total of 14) located on the ssDNA docking loop ~ 300b in length (figure 6-7). In this way a single DNA-enzyme conjugates can be multiply hybridized to the structure. The DNA oligonucleotide, to which the enzyme was conjugated, was additionally modified with a cy5 fluorophore at the 3' end (oligonucleotide: 200 SH cy5, mw: 7166), as a way of verifying the incorporation of the DNA-enzyme conjugate to the target DNA structure. The pBluescript DNA sequence and crossover strands are listed in fully in appendix B. The diffusivity or motion of the particle is indicated by the apparent diffusion coefficient, which can be derived through techniques such as DLS, particle tracking methods as NTA nanoparticle tracking analysis, or other techniques which could be used for this purpose, such as fluorescence correlation spectroscopy (FCS) and optical microscopy (for larger particles). In this chapter, nanoparticle tracking analysis (NTA) and dynamic light scattering (DLS) were used to determine the effect of L-lysine concentration on the diffusive motion of the DNA-enzyme structure.

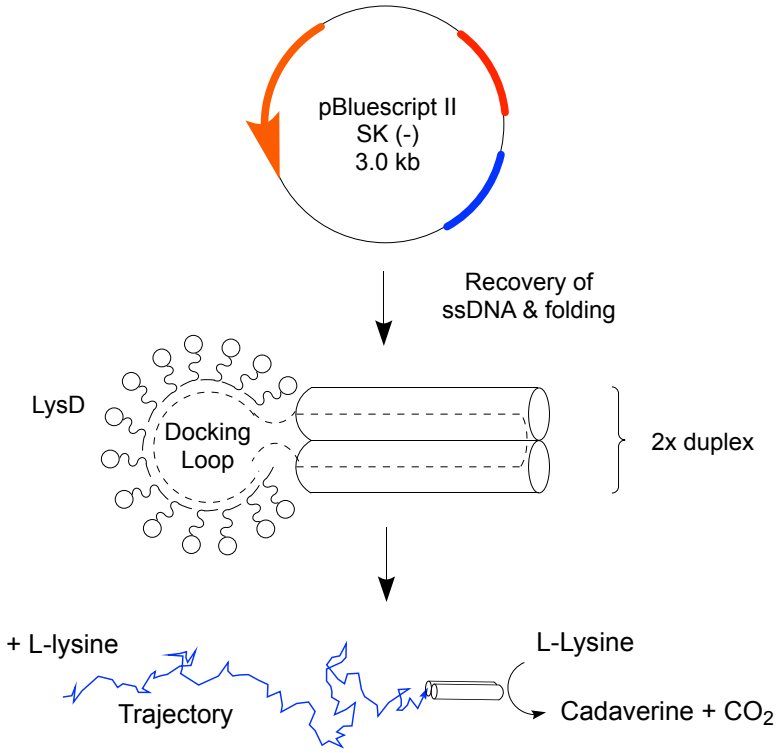

Figure 6-7 Schematic representation of the lysine decarboxylase modified DNA structure. Lysine decarboxylase is tethered to a single end of a folded ssDNA scaffold strand (pBluescript II SK (-)) The enzyme is indicated as a sphere. For future work, the ssDNA based scaffold structure has the potential to be folded into a range of other two or three dimensional structures.

6.2.2 Expression and purification of lysine decarboxylase (deC 87095)

Lysine decarboxylase (deC 87095 cloned in a pET29 vector) was recombinantly expressed in *E. coli* strain BL21. The histidine tagged enzyme (his tag located at the c-terminus) was extracted using detergent based lysis and purified by immobilized metal affinity chromatography (IMAC) using a gravity flow his-tag capture column. The purified enzyme was assessed by denaturing polyacrylamide gel electrophoresis (figure 6-8 left gel). The purified product migrates in reasonable agreement with the theoretical mw of the enzyme (18819.3Da), although slightly greater by approximately 4kDa. However, its migration is in line with the analysis of the purified enzyme by denaturing PAGE elsewhere (unpublished data). An outline of the expression vector and theoretical properties of the enzyme are summarised in table 5-1. To confirm the activity of the enzyme, it was assayed with L-lysine and pH changes were measured to confirm the activity of the enzyme (results not shown).

Theoretical molecular weight (kDa)	Theoretical pI	Expression vector
18819.3	4.87	pET29a(+)

Table 6-1 Properties of Lysine decarboxylase deC_ 87095.

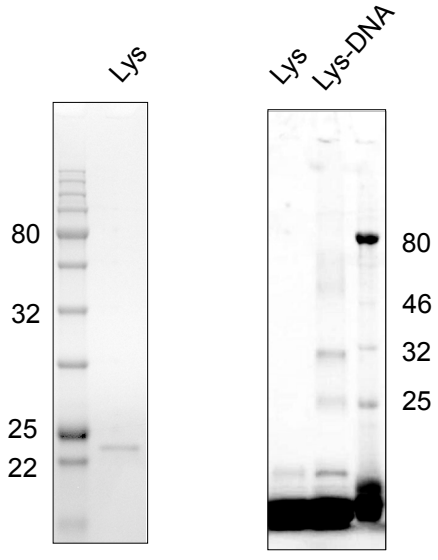

Figure 6-8 Analysis of purified lysine decarboxylase (deC 87095) and analysis of DNA-LysDeC conjugation products by 15% denaturing Tris glycine SDS PAGE.
Left gel: Analysis of purified lysine decarboxylase (deC 87095) enzyme after his tag purification (immobilized metal affinity chromatography). **Right gel:** Fluorescence

visualisation of the conjugation reaction products between lysine decarboxylase and the target DNA oligonucleotide (200 SH cy5). Lane 1: Lysine decarboxylase + DNA -crosslinker. Lane 2: Crosslinked enzyme +crosslinker. Ladder: NEB Colour Prestained Protein Standard, Broad Range (11–245 kDa).

Lysine decarboxylase was conjugated to the target DNA oligonucleotide (200 SH cy5, mw: 7166), using the heterobifunctional crosslinker sulfo-SMCC, as outlined in chapter 4. The conjugation between LysDeC and the target oligonucleotide (figure 6-8, right gel, lane 2) yields a series of products, which correspond to the addition of one and two DNA oligonucleotides (adjacent to the 25 and 32kDa markers) to the enzyme. Additional products, slightly broader and less intense, migrate between 58kDa and 50kDa, are believed to represent multimeric structures. A control reaction, without the addition of cross linker (right gel, lane 1), was included for comparison and shows no product formation which excludes the formation of DNA-enzyme species through non-covalent interactions. Unreacted Cy5 thiol modified DNA oligonucleotide is observed at the bottom of both lanes. The DNA enzyme conjugates were purified using a centrifugal filtration column with a molecular weight cut off of 30kDa with a series of washes to remove excess DNA oligonucleotide from the reaction mixture, as also described in chapter 4.

6.2.3 Preparation of the ssDNA scaffold and folded structure

To prepare the DNA structure, the ssDNA scaffold was derived using a phagemid/helper phage system. The target phagemid pBluescript II SK(-) (2961 bp in length), was transformed in *E. coli* and recovered in single stranded form by infection with the helper phage VCM13. The ssDNA products (figure 6-9 lane 2) were purified by agarose gel extraction and spin column purification to remove co-packaged helper phage VCM13 genome (the additional bands above the major product in lane 2).

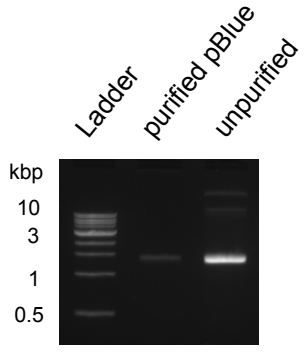

Figure 6-9 Purification of pBluescript SK(-) ssDNA scaffold for the preparation of the Lysine decarboxylase modified DNA structure. Ladder: NEB Quick-Load® 1 kb DNA Ladder, gel: 1% 1 X TBE agarose gel.

The DNA structure was prepared by annealing the staple strands and enzyme conjugate capture strands (a total of 28 DNA oligos) to the ssDNA structure in 2X molar excess. The product shows enhanced migration compared to the ssDNA only (figure 6-10 lane 1 compared to lane 2) which indicates compaction of the structure in line with the hybridization of the oligonucleotides to the ssDNA. The DNA-lysine conjugates were hybridized in excess to the DNA structure by incubation at 37°C, to promote hybridization of the conjugates to the captures strands on the ssDNA structure and to prevent denaturation of the enzyme at higher temperatures. The upshift in migration observed for the annealed products (lane 3 figure 6-10) indicates incorporation of the DNA-enzyme conjugates, and this was also verified by fluorescence visualisation of the gel (right gel figure 6-10) which also supports the incorporation of the DNA-enzyme to the ssDNA

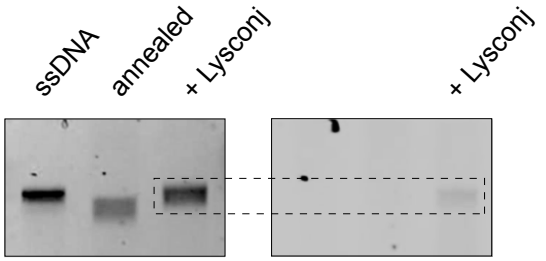

Figure 6-10 Preparation of the lysine decarboxylase functionalized DNA structure, analysed by agarose gel electrophoresis. Annealing of template and incorporation of Lysine Decarboxylase conjugate. Left: visualization of the agarose gel showing under the green channel (SYBR green). Right: red channel, the band on the third lane indicates hybridization of the cy5 labelled LysD-DNA conjugate.

6.2.4 Particle sizing and diffusion coefficient analysis by dynamic light scattering (DLS)

The hydrodynamic diameter of the annealed DNA-lysine decarboxylase structure was determined by dynamic light scattering DLS (figure 6-11), and an apparent hydrodynamic radius of 146.5 ± 26.3nm (mean ± standard deviation) was observed. The diffusive motion of the DNA-enzyme structure was measured in the presence of increasing substrate concentration,

by DLS to determine the effect of enzyme catalysis on the motion of a DNA structure at 1, 5 and 10mM L-lysine concentrations (figure 6-12). In the absence of L-lysine, an apparent diffusion coefficient of 4.83 ± 0.01 $\mu m^2/s$ (mean ± standard error of the mean) was observed at 37°C. With the addition of L-lysine, to a final concentration of 1mM, the measured diffusion coefficient was 7.45 ± 0.02 $\mu m^2/s$, and for 5mM L-lysine, 7.55 ± 0.08 $\mu m^2/s$, which represents an enhancement of 1.6 X compared to the DNA-enzyme structure in the absence of the substrate. At 10mM L-lysine, a further increase in the apparent diffusion coefficient was not observed for the DNA-enzyme structure, rather, a reduction was seen, to 6.06 ± 0.02 $\mu m^2/s$, which could be the result of substrate inhibition. All values represent the mean ± standard error of the mean (s.e.m) of the Gaussian fitting to the intensity distributions (figure 6-12). Based on the DLS analysis, the measured diffusion coefficient appears to increase in a concentration dependent manner, with the exception of the measurement at 10mM L-lysine. The analysis also suggests that the system is saturated at 1mM L-lysine, as a further increase in the apparent diffusion coefficient is not observed beyond 5mM. Interestingly, two species are apparent at 1mM, which suggests that the enhancement is not observed across all species at that concentration. It is unclear why a reduction in the diffusion coefficient is seen at 10mM L-lysine, although it is still greater by 1.25 X compared to the DNA-enzyme structure in the absence of L-lysine.

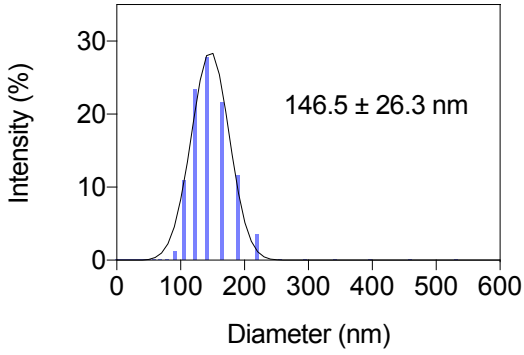

Figure 6-11 Dynamic light scattering (DLS) sizing analysis of DNA-Lysine decarboxylase structure (no addition of substrate). A mean of 146.5 ± 26.3nm is observed based on the Gaussian fitting (mean ± standard deviation). The measurement was conducted at 37°C, in 0.1M HEPES, 5mM $MgCl_2$, pH 7.5.

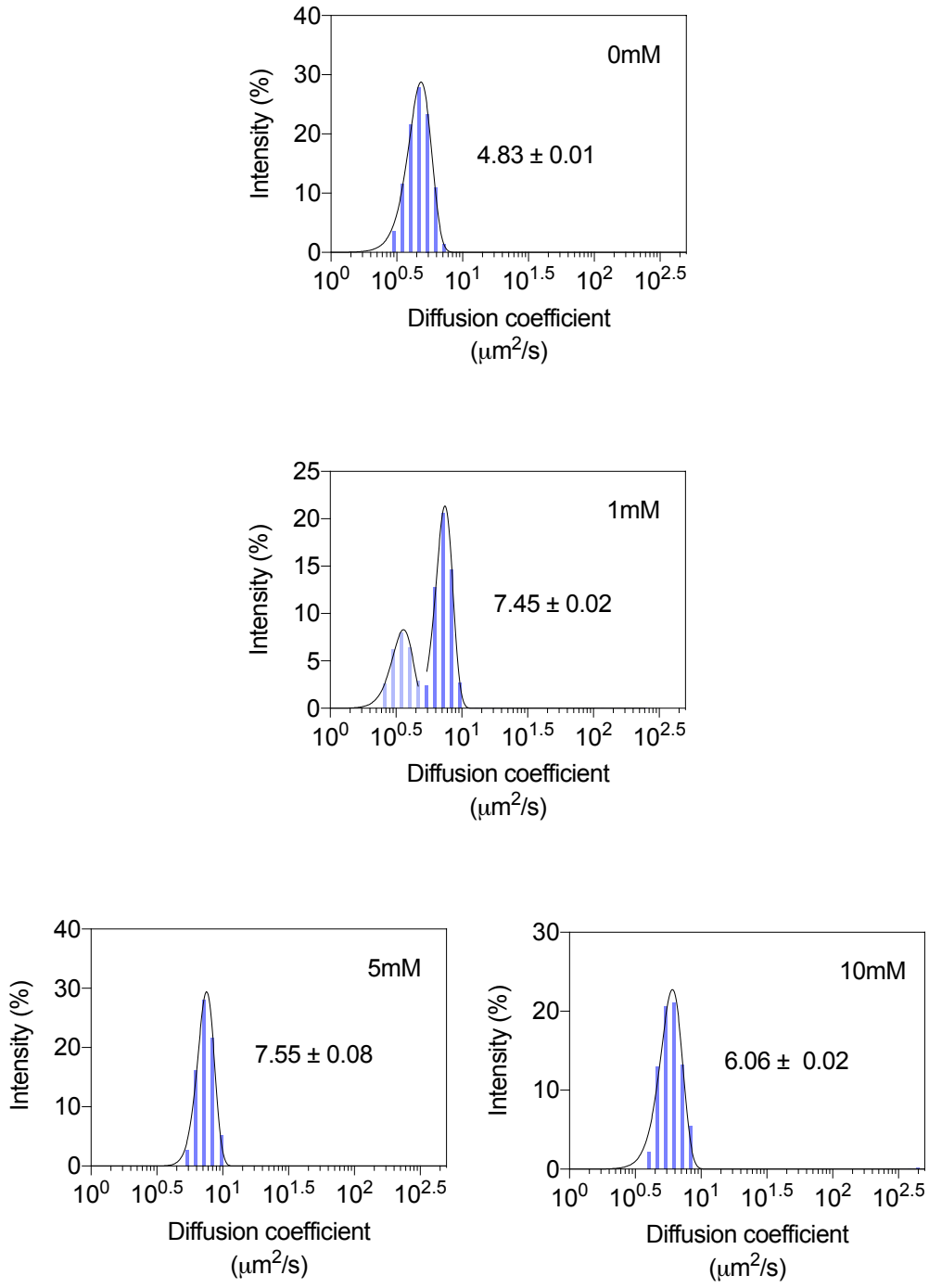

Figure 6-12 Measured diffusion coefficient for the Lysine-decarboxylase-DNA structure at 1-10mM L-lysine substrate, determined by dynamic light scattering. Measurements were performed at 37°C, in 0.1M HEPES, 5mM $MgCl_2$, pH 7.5. Errors represent the standard error of the mean (s.e.m) of the Gaussian fitting to the intensity distributions.

6.2.5 Nanoparticle tracking analysis of Lysine decarboxylase modified DNA structure

In addition to DLS, nanoparticle tracking analysis (NTA) was used to investigate the effect of L-lysine on the diffusivity of the DNA-enzyme structure. Unlike DLS, NTA involves the visualisation and tracking of particles in solution to obtain individual trajectories over the duration of several seconds. Four sample particle trajectories (figure 6-13), typify the traces obtained by NTA. To calculate the diffusion coefficient of those particles, the mean square displacement is plotted as a function of lag time (figure 6-14 showing the corresponding MSD curves for the sample particles displayed in figure 6-13), which can be derived from the slope of a fitted line to the MSD curve. For example, for objects undergoing simple Brownian motion this relationship is expressed by Equation 2. The MSD curve can also give an indication of the type of motion that is experienced by the particle, for instance, it can indicate 'confined' motion, in which the profile of the MSD curve plateaus at greater lag times, or 'super diffusivity' which is indicated by an upward inflection of the curve. For a freely diffusing particle, the change in MSD is linear with time.

The diffusion coefficient for all particles at each concentration are displayed as a frequency distribution fitted with a Gaussian distribution to obtain an average diffusion coefficient for each condition (figure 6-15). In the absence of L-lysine an apparent diffusion coefficient of 5.94 ± 0.13 $\mu m^2/s$ (mean ± standard error of the mean) is observed for the DNA-enzyme structure, which is greater by a factor of 1.2 compared to the value obtained by DLS. With the addition of L-lysine at 1, 5 and 10mM concentrations, a positive trend is observed between L-lysine concentration and the apparent diffusion coefficient (figure 6-16). For the DNA-enzyme structure in the presence of 1mM L-lysine, an apparent diffusion coefficient of 5.36 ± 0.06 $\mu m^2/s$ is observed, which is a slight reduction on the native DNA-enzyme structure in the absence of L-lysine. A value of 6.58 ± 0.09 $\mu m^2/s$ is observed for 5mM L-lysine, and 7.34 ± 0.08 $\mu m^2/s$ for 10mM L-lysine. All values represent the mean ± standard error of the mean (s.e.m) of the Gaussian fitting to the frequency distributions (figure 6-15).

The maximum values obtained for both DLS and NTA analysis are 7.55 and 7.34 $\mu m^2/s$ respectively, which are in good agreement. Although for DLS the apparent diffusion coefficient peaks at 1mM L-lysine, rather than 10mM, for NTA. While a linear relationship is observed between the diffusion coefficient and L-lysine concentration by NTA, for DLS, the enhancement appears to plateau rather than increase with higher substrate concentrations (figure 6-16). This discrepancy can be explained by the difference in how the diffusion coefficient is derived by NTA and DLS. It is also known that DLS suffers from intensity bias towards larger particles, since they scatter light more intensely than those which are smaller.

This could explain the greater apparent diffusion coefficients observed with the addition of lysine by DLS, compared to those obtained under the equivalent conditions by NTA.

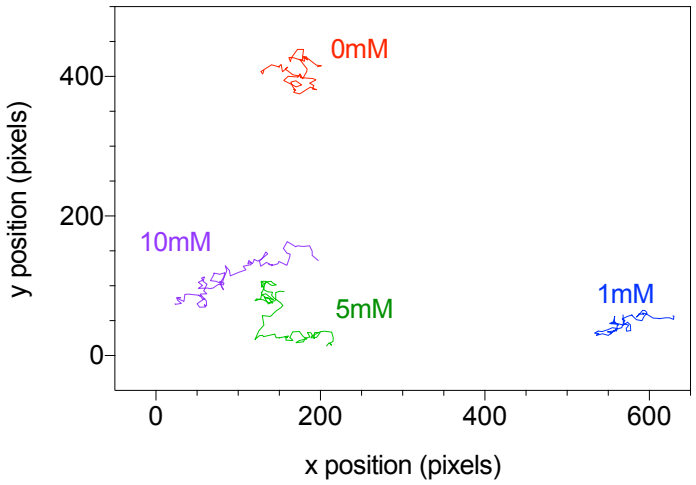

Figure 6-13 Sample particle trajectories for the DNA-Lysine decarboxylase structure at 1,5 and 10mM L-Lysine substrate concentrations and in the absence of L-lysine. The sample trajectories were obtained by nanoparticle tracking analysis (NTA) and represent the tracked motion of individual particles in x and y position.

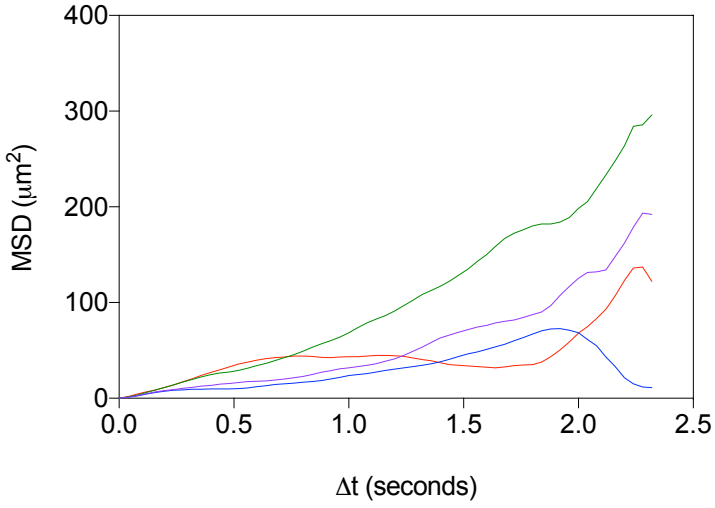

Figure 6-14 Mean square displacement vs lag time (Δt) for four sample tracks shown in figure 6-13. The MSD curve can give an indication of the type of motion that a particle undergoes, these particular particles, with 5 and 10mM L-lysine, demonstrate enhanced diffusion (green and purple lines), as observed from the analysis of MSD curve above. Green line: + 5mM L-lysine, red: - Lysine, blue: 1mM lysine, purple: 10mM.

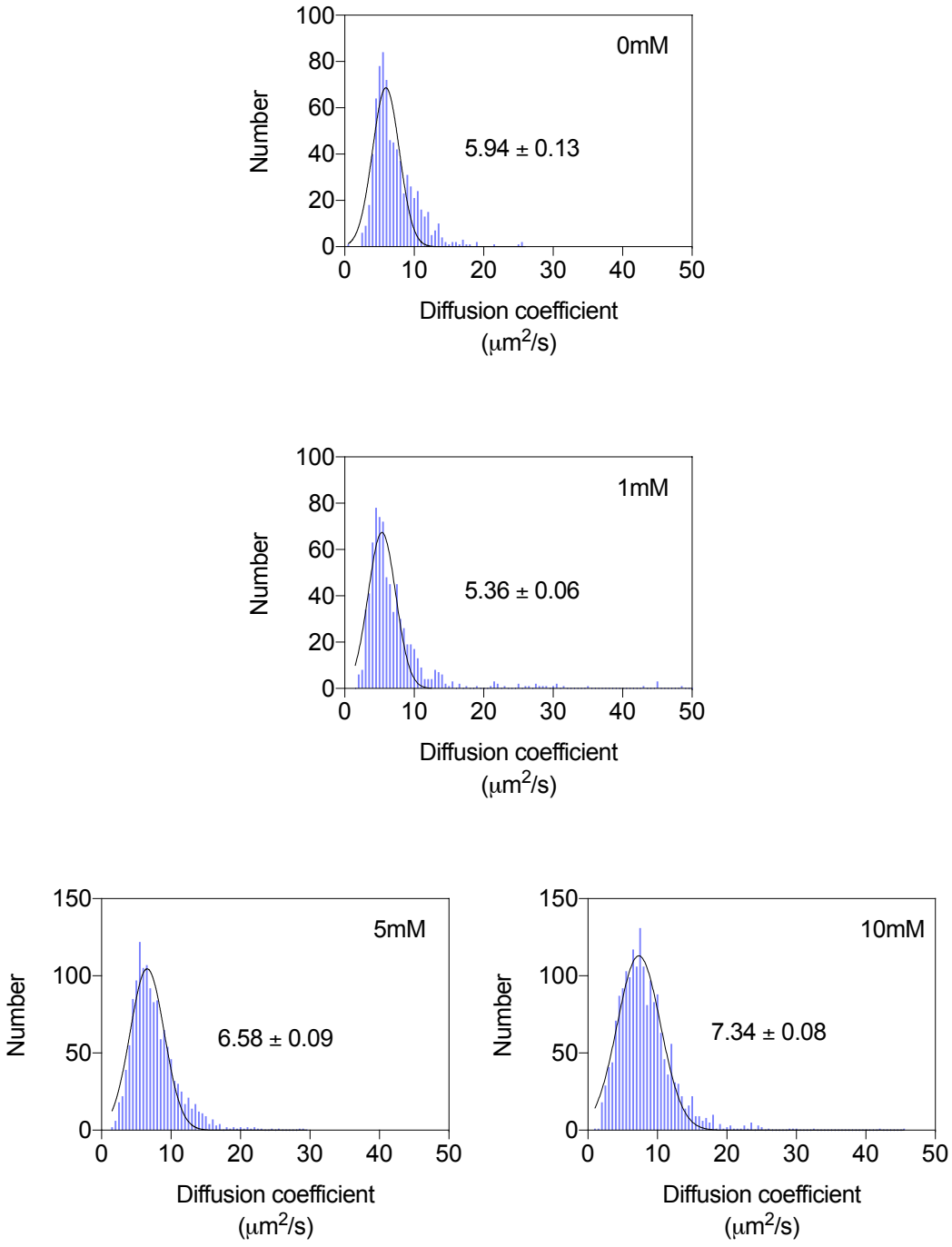

Figure 6-15 Histograms showing distribution of diffusion coefficients for all measured particle tracks, at 0,1,5 and 10mM added L-Lysine substrate concentrations. Trajectories were obtained by nanoparticle tracking analysis (NTA). Nanoparticle tracking conditions were at 37°C, 0.1M HEPES, 5Mm $MgCl_2$, pH 7.5, with L-lysine at the stated concentrations inset. Error values represent the standard error of the mean (s.e.m) of the Gaussian fitting to the intensity distributions.

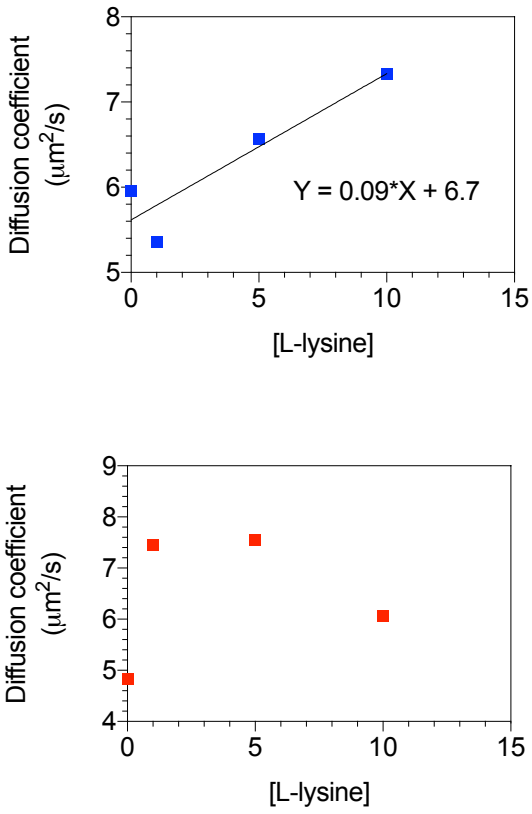

Figure 6-16 Relationship between L-lysine concentration and the measured diffusion coefficient by nanoparticle tracking analysis (NTA) and dynamic lights scattering (DLS). Top: the relationship observed between [L-lysine] and the measured diffusion coefficient by NTA. **Bottom:** [L-lysine] vs diffusion coefficient by DLS. Error bars are too small to be seen, but represent the standard error of the mean.

6.2.6 Analysis of NTA particle trajectories

At each concentration of L-lysine, the mean-square displacement (MSD) was plotted against lag time (t) for all particle trajectories measured, in order to obtain an ensemble average (figure 6-17). The profile of the MSD vs t curve can provide an indication of the type of motion undergone by tracked particles. For example, the MSD curve may indicate if particles are freely diffusing, transported, or confined in movement. Individual trajectories were analysed using MATLAB (@msdanalyzer MATLAB class[154]) to obtain an ensemble average over all tracks for each condition tested. The standard deviation over all MSD tracks is indicated by the black line, and the standard error of the mean by the error bars on the respective coloured curves (figure 6-17). With the addition of L-lysine substrate an enhancement in motion is observed, as indicated by the upward shift in the MSD curves for 1, 5 and 10mM L-lysine concentrations,

compared to that in the absence of L-lysine (purple line) (figure 6-17). The profile of the MSD curves in the presence of L-lysine are suggestive of enhanced diffusion and are consistent with the view that conversion of L-lysine by the tethered enzymes enhances the motion of the DNA-enzyme structure. A log-log plot the averaged MSD curves (figure 6-18 middle graph), clearly demonstrates the enhancement, particularly at the lower lag times. A comparison of the curve at 10mM vs no L-lysine is also included to highlight the shift (figure 6-18 bottom graph).

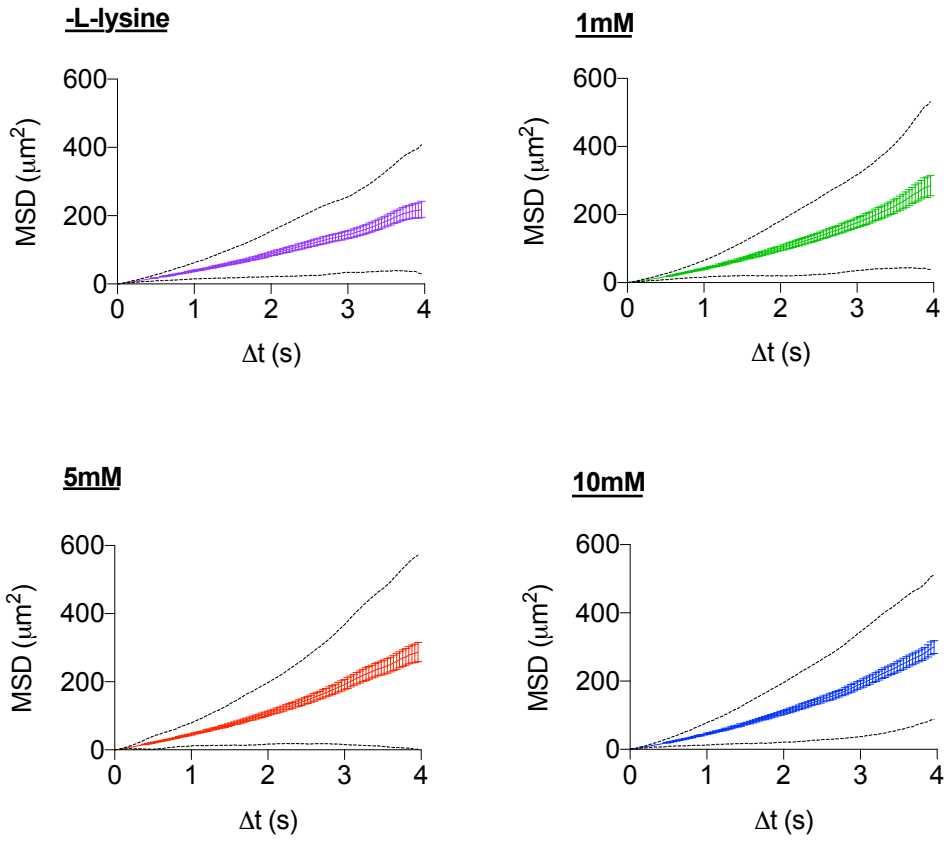

Figure 6-17 Calculation of the ensemble average over all measured tracks for 0-10mM L-lysine concentrations. Purple: -L-lysine, Green: 1mM, Red: 5mM and Blue: 10mm. MSD vs lag time curves and weighted averages were calculated using the @msdanalyzer MATLAB class[154]. The black lines represent the standard deviation and the error bars on the coloured lines represent the standard error of the mean.

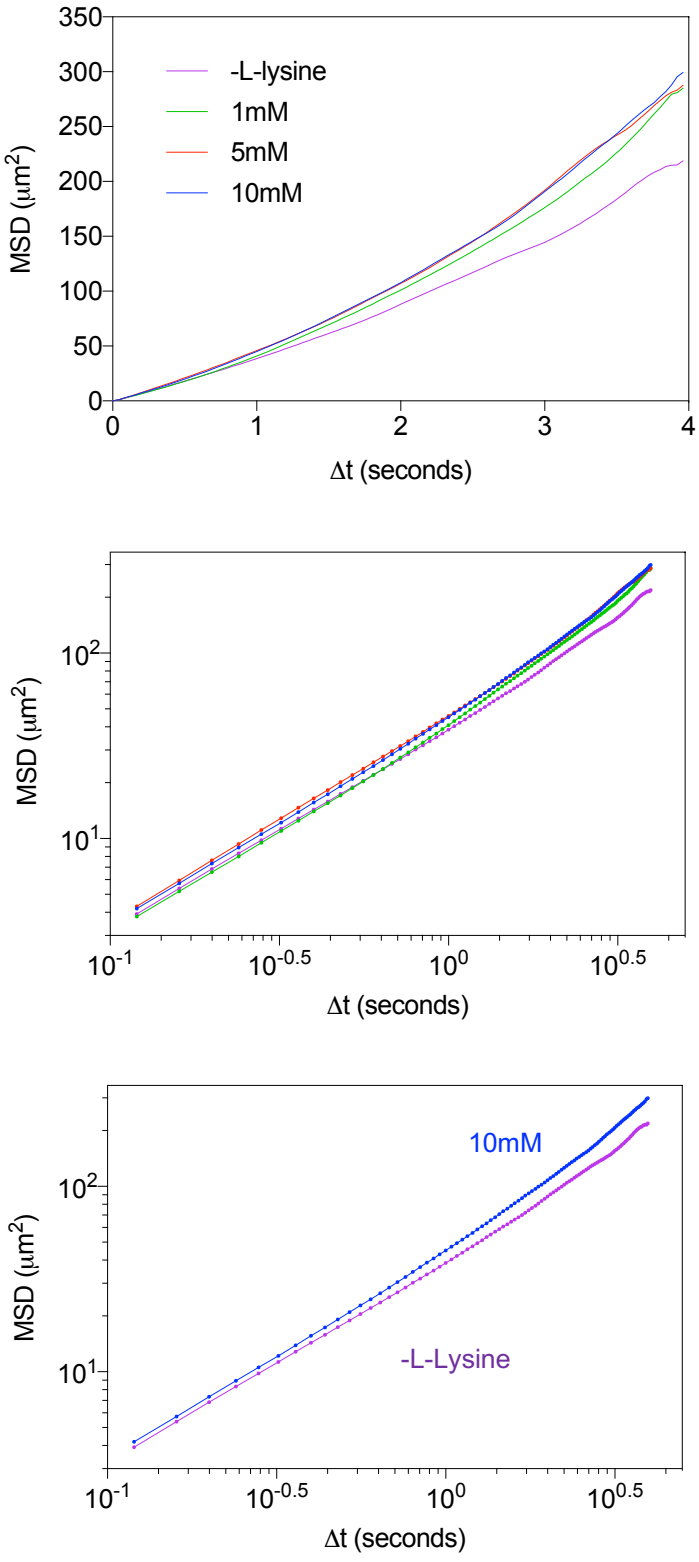

Figure 6-18 Log-Log plot showing the ensemble average MSD vs lag time calculated for all concentrations of L-lysine. Purple: -L-lysine, Green: 1mM, Red: 5mM and Blue: 10mm. MSD vs lag time curves tracks and weighted averages were calculated using the @msdanalyzer MATLAB class[154].

6.3 Discussion

This chapter outlines the use of enzymatic catalysis an alternative mechanism to affect the of motion of a DNA nanostructure. While movement across length scales can be achieved through mechanisms analogous to the molecular motion of motor proteins across microtubule filaments, such as by DNA based walkers along defined DNA/RNA tracks[25,238–240,248,262–267], or motion driven by external fields[230,231], enzymatic catalysis remains an unexplored method for inducing the motion of a DNA structure. Motion based on the catalytic conversion could extend the capabilities of DNA nanostructures beyond those that are constrained to a defined path or solid support[268], and opens their application in the areas of chemotaxis, directed delivery of cargo and nanomedicine. The diffusive motion of the DNA-enzyme structure was measured in the presence of increasing substrate concentration, L-lysine, to determine the effect of enzyme catalysis on the motion of a DNA structure (Figure 6-6). Enhanced diffusive motion was observed for the DNA-Lysine decarboxylase structure in the presence of its substrate L-lysine in a concentration dependent manner, by both NTA and DLS analysis. Although a discrepancy was observed between measurements obtained by DLS and NTA, in terms of the trend between substrate concentration and the apparent diffusion coefficient, analysis by both methods indicated a positive relationship between L-lysine concentration and the diffusive motion of the DNA-enzyme structure, which is indicative of self-propulsion.

Initially, it was thought that lysine decarboxylase could enhance the motion of a nanostructure through the generation of CO_2 , in a way that was analogous to that reported for micro-rockets[257]. Later it was realised that the mechanisms underlying enhanced diffusive motion or directed motion could be brought about through other mechanisms, such as through the asymmetric distribution of products which could result in self-electrophoresis induced by chemical or ionic gradients, as has been suggested elsewhere. We hypothesize that the enhancement of diffusive motion is the result of a self-phoretic mechanism whereby the structure is (attracted) due to a self-generated chemical gradient by the enzymatic conversion of the substrate. The reaction product cadaverine - a positively charged substrate (pKa1 = 10.25; pKa2 = 9.13) could induce such an effect by attracting the - charged DNA structure within a local chemical/ionic gradient.

Although the formation of the DNA-enzyme structure was confirmed by agarose gel electrophoresis and fluorescence analysis, for the incorporation of the lysine DeC conjugate, further structural characterization would have been beneficial to better understand the nature of the DNA-enzyme structure and whether enzyme molecules are immobilized in the same stoichiometry across all structures (for instance through AFM). For future development, other

enzymes or structural designs could be investigated to determine if similar effects are also found, as well as to improve the extent of diffusive motion for the structure. In terms of functional applications, one particular area of interest would be the tethering of cargo for use in targeted delivery through autonomous movement, for example in a biomedical setting - such as the delivery of drug molecules.

Chapter 7

Conclusions and outlook

7.1 Concluding remarks and future directions

In Chapter 4, a DNA based scaffold was proposed for the immobilization of enzyme cascades. Enzymes serve important roles in the bioprocessing industries, as well as for bioremediation and healthcare applications. Traditionally, enzyme immobilization has been performed on solid supports such as agarose, epoxy resins as well as other insoluble substrates. DNA nanotechnology has emerged as a highly versatile approach for the construction of nanoscale structures. In terms of programmability and amenability to functionalization, DNA remains unrivalled as a biomaterial. Here, DNA nanoballs were designed and synthesized by phi29 rolling circle amplification. The concatemeric ssDNA was designed such that it incorporated orthogonal sites for the hybridization of DNA oligonucleotide enzyme conjugates. Rather than spatially separate individual enzymes at defined distances, as described by others[269], we investigated the use of DNA NBs to sequester multiple copies of an enzyme cascade on a self-compacting concatemeric ssDNA. This method presents several advantages over other DNA systems for the immobilization of biomolecules, particularly for biotechnological applications. Firstly, DNA NBs do not require numerous unique oligonucleotides for assembly (since it relies on a single ssDNA starting template form which structures are generated), the enzymatic nature of NB synthesis eliminates the need for careful hybridization procedures, for instance, lengthy annealing steps over a number of hours[48]. Moreover, numerous biomolecules can be recruited to the structure without the need for multiple unique DNA oligonucleotides-biomolecule conjugates.

The synthesized ssDNA product was self-compacted to form a mesh network, which was evidenced by AFM analysis, which revealed compacted spherical structures in line with the hypothesized packing process through complementary hairpin loops. Dynamic light scattering (DLS) and NTA (nanoparticle tracking analysis) sizing analysis also supported the size range of structures and the mostly discrete nature of DNA NBs. Although the synthesized products observed by AFM were not entirely homogenous in their dimensions, generally, there was consistency in their morphology. A horseradish peroxidase/glucose oxidase enzyme pair was immobilized on DNA NBs through conjugation to carrier oligonucleotides, complementary to the ssDNA sequence of the NB structure. An amine to thiol crosslinking strategy was used for

the preparation of DNA-enzyme conjugates, and the hybridization of conjugates to the nanoballs was confirmed by fluorescence analysis. The reaction progress of the bi-enzyme cascade, using the reduction of the colorimetric substrate ABTS, was compared with the free conjugates (- DNA nanoball). An extended lag time (or transient time) was observed for conjugates immobilized on DNA nanoballs compared to the equivalent free conjugates. Unlike other DNA immobilized enzyme systems reported in the literature, immobilization or sequestration of the HRP/GOx bi-enzyme system did not enhance the reaction rate of the cascade. Rather, it appears that scaffolding by the DNA nanoball structure increases the time taken to establish the steady state (the steady state is the period of the reaction during which the concentration of the intermediate is constant, i.e. where its production and conversion occur at the same rate). It was hypothesised that the DNA nanoball structure imparts some barrier to the formation of the intermediate, or the diffusion of substrates into the DNA-enzyme structure. Owing to time, the effect of immobilization on the stability of the HRP/GOx cascade was not probed, but would be a key area for future investigation.

An alternative structure for the immobilization of enzymes, or other biomolecules, was described in chapter 3, based the assembly of a three-armed DNA tile to form polyhedral structures. Although there was evidence of self-assembly of the tile, in line with predictions, the number of correctly formed structures was outweighed by misfolded objects by AFM analysis, indicating a high degree of incorrect assembly. This was also supported by analysis of the assembly process by agarose gel electrophoresis, which indicated aggregation of the tile structures. For this reason, this particular design was not pursued further, and it would be necessary to redesign the DNA tile for future development. Other methods could be used to create similar polyhedral structures, such as using a scaffolded approach, as has been shown by others[156].

In chapter 5, the nanoball system was used to immobilize a bi-enzyme system for the synthesis of BIA precursors. Benzylisoquinoline alkaloids are a valuable class of plant secondary metabolites which exhibit varied and potent pharmacological properties. There has been significant interest in the reengineering of BIA pathways in synthetic biology, for instance, BIA pathways have been introduced in *E. coli*[208] and *S. cerevisiae*[206]. However, *ex vivo* approaches for the display and assembly of BIA pathways have not been explored. While almost all previous studies involving the use of DNA based devices for the display of enzymes have focused on a handful of model systems, most commonly the HRP/GOx bi-enzyme pair, here it has been shown for a genuinely biotechnologically relevant bi-enzyme system, the transaminase and norcoclaurine synthase enzyme pair for the synthesis of benzylisoquinoline precursors. TAm/NCS catalyse the conversion of a single starting substrate, dopamine, (or

another phenethylamine such as 3-hydroxyphenethylamine, which was also described) to produce norlaudanosoline, a valuable BIA precursor. While it was demonstrated that the NB system could be applied to an enzyme cascade beyond commonly used model systems, substrate conversion for both dopamine and 3-hydroxyphenethylamine was unaffected by the DNA NB (compared to the equivalent free conjugates in the absence of NBs). While both enzyme pairs HRP/GOx and TAm/NCS were successfully conjugated to target DNA oligonucleotides, a reduction in enzymatic activity was observed for both conjugate pairs compared to their free equivalents.

A key area for future work, would be the use of an alternative DNA-protein conjugation procedure as it was difficult to accurately determine the extent of modification on target enzymes. Moreover, the purification of DNA-enzyme conjugates also proved to be challenging in some cases. An alternative approach to the recruitment of biomolecules to the DNA nanoball, could be the incorporation of modified dNTPs during the amplification process, as a way of directly incorporating chemical groups for conjugation or non-covalent interactions to target biomolecules. In this way, the attachment procedure could be performed directly to the nanoball structure, without the requirement for a separate conjugation and purification step, which happened to be quite challenging during the process of these experiments. Alternatively, site-specific conjugation strategies could be used, such as the fusion systems described in chapter 1 (SNAP and CLIP tags). More generally, the results in chapters 4 and 5 demonstrate the limitations of current bioconjugate techniques, as they can often compromise the integrity of the target protein of interest or impart negative effects on their activity. In the context of existing studies on the use of DNA nanostructures for the display of enzyme cascades, the results found in this thesis do not support the view that spatial distance between enzymes an enzyme cascade improves reaction rate, or the view that a DNA structure can improve the reaction rate for the HRP/GOx pair by reducing the local pH, as has been proposed elsewhere[137].

In Chapter 6, the use of enzymatic catalysis was investigated as a means of actuating the motion of a DNA nanostructure. This involved tethering multiple lysine decarboxylase enzymes to a scaffold DNA, in order to investigate whether catalytic conversion by the enzyme would induce enhanced motion in response to the addition of its substrate L-lysine. A positive relationship was observed between L-lysine concentration and the apparent diffusion coefficient for the DNA-lysine deC structure. Although directed motion was not specifically observed, an increase in diffusivity was found, compared the to the structure in the absence of substrate l-lysine. This was supported by the analysis of the diffusion coefficient of particles by dynamic light scattering, nanoparticle tracking analysis and the analysis of the MSD vs lag time for particle trajectories. Although the exact mechanism underlying the increase in diffusivity is unclear,

one possible mechanism could be a self-phoretic effect, due to the generation of a local concentration gradient in which the structure experiences attraction towards. This could be brought about through the reaction product cadaverine, a positively charged product, which could induce such an effect by attracting the net negatively charged DNA structure. Self-autonomous nanoscale and microscale devices are receiving increasing interest in the field of nanotechnology, as researchers attempt to create devices with more sophisticated capabilities. The use of enzymatic conversion represents an alternative approach to the control of the motion of DNA based structures, which does not rely on its hybridization to a predefined path. To the best of our knowledge, enzymatic catalysis has not been used to affect the motion of a DNA nanostructure in this way previously.

References

1. Burge, S., Parkinson, G. N., Hazel, P., Todd, A. K. & Neidle, S. Quadruplex DNA: sequence, topology and structure. *Nucleic Acids Res.* **34,** 5402–5415 (2006).
2. Chapter 3. Nucleosides and Nucleotides. in *Nucleic Acids in Chemistry and Biology* 77–142 (Royal Society of Chemistry). doi:10.1039/9781847555380-00077
3. Soukup, G. A., Soukup & A, G. Nucleic Acids: General Properties. in *eLS* (John Wiley & Sons, Ltd, 2003). doi:10.1038/npg.els.0001335
4. Watson, J. D. & Crick, F. H. Molecular structure of nucleic acids; a structure for deoxyribose nucleic acid. *Nature* **171,** 737–8 (1953).
5. Chapter 2. DNA and RNA Structure. in *Nucleic Acids in Chemistry and Biology* 13–76 (Royal Society of Chemistry). doi:10.1039/9781847555380-00013
6. Bowater, R. P., Waller, Z. A., Bowater, R. P. & Waller, Z. A. DNA Structure. in *eLS* (John Wiley & Sons, Ltd, 2014). doi:10.1002/9780470015902.a0006002.pub2
7. Ussery, D. W. DNA Structure: A-, B- and Z-DNA Helix Families. in *Encyclopedia of Life Sciences* (John Wiley & Sons, Ltd, 2002). doi:10.1038/npg.els.0003122
8. *Nucleic Acids in Chemistry and Biology*. (Royal Society of Chemistry, 2007). doi:10.1039/9781847555380
9. Hagerman, P. J. Flexibility of DNA. *Annu. Rev. Biophys. Biophys. Chem.* **17,** 265–86 (1988).
10. *Oxford Dictionary of Biochemistry and Molecular Biology*. (Oxford University Press, 2006).
11. Holliday, R. A mechanism for gene conversion in fungi. *Genet. Res.* **5,** 282 (1964).
12. Duckett, D. R. *et al.* The structure of the Holliday junction, and its resolution. *Cell* **55,** 79–89 (1988).
13. Brázda, V., Laister, R. C., Jagelská, E. B. & Arrowsmith, C. Cruciform structures are a common DNA feature important for regulating biological processes. *BMC Mol. Biol.*

12, 33 (2011).

14. Luger, K. Nucleosomes: Structure and Function. in *eLS* (John Wiley & Sons, Ltd, 2001). doi:10.1038/npg.els.0001155

15. Wang, W. *et al.* Holliday Junction Thermodynamics and Structure: Coarse-Grained Simulations and Experiments. *Sci. Rep.* **6,** 22863 (2016).

16. Seeman, N. C. Nanomaterials based on DNA. *Annu. Rev. Biochem.* **79,** 65–87 (2010).

17. Seeman, N. C. DNA nanotechnology: novel DNA constructions. *Annu. Rev. Biophys. Biomol. Struct.* **27,** 225–48 (1998).

18. Seeman, N. C. Nucleic acid junctions and lattices. *J. Theor. Biol.* **99,** 237–247 (1982).

19. Wei, B., Dai, M. & Yin, P. Complex shapes self-assembled from single-stranded DNA tiles. *Nature* **485,** 623–6 (2012).

20. Fu, T. J. & Seeman, N. C. DNA double-crossover molecules. *Biochemistry* **32,** 3211–20 (1993).

21. Lin, C., Liu, Y. & Yan, H. Designer DNA nanoarchitectures. *Biochemistry* **48,** 1663–74 (2009).

22. Li, X., Yang, X., Qi, J. & Seeman, N. C. Antiparallel DNA Double Crossover Molecules As Components for Nanoconstruction. *J. Am. Chem. Soc.* **118,** 6131–6140 (1996).

23. Park, S. H. *et al.* Three-helix bundle DNA tiles self-assemble into 2D lattice or 1D templates for silver nanowires. *Nano Lett.* **5,** 693–6 (2005).

24. Reichel, A. *et al.* Noncovalent, site-specific biotinylation of histidine-tagged proteins. *Anal. Chem.* **79,** 8590–600 (2007).

25. Venkataraman, S., Dirks, R. M., Rothemund, P. W. K., Winfree, E. & Pierce, N. a. An autonomous polymerization motor powered by DNA hybridization. *Nat. Nanotechnol.* **2,** 490–4 (2007).

26. Liu, D., Wang, M., Deng, Z., Walulu, R. & Mao, C. Tensegrity: construction of rigid DNA triangles with flexible four-arm DNA junctions. *J. Am. Chem. Soc.* **126,** 2324–5 (2004).

27. Chen, J. H. & Seeman, N. C. Synthesis from DNA of a molecule with the connectivity

of a cube. *Nature* **350,** 631–3 (1991).

28. Goodman, R. P. *et al.* Rapid chiral assembly of rigid DNA building blocks for molecular nanofabrication. *Science* **310,** 1661–5 (2005).

29. He, Y. *et al.* On the chirality of self-assembled DNA octahedra. *Angew. Chem. Int. Ed. Engl.* **49,** 748–51 (2010).

30. Winfree, E., Liu, F., Wenzler, L. A. & Seeman, N. C. Design and self-assembly of two-dimensional DNA crystals. *Nature* **394,** 539–44 (1998).

31. Yan, H., Park, S. H., Finkelstein, G., Reif, J. H. & LaBean, T. H. DNA-templated self-assembly of protein arrays and highly conductive nanowires. *Science* **301,** 1882–4 (2003).

32. Yan, H., LaBean, T. H., Feng, L. & Reif, J. H. Directed nucleation assembly of DNA tile complexes for barcode-patterned lattices. *Proc. Natl. Acad. Sci. U. S. A.* **100,** 8103–8 (2003).

33. Shih, W. M., Quispe, J. D. & Joyce, G. F. A 1.7-kilobase single-stranded DNA that folds into a nanoscale octahedron. *Nature* **427,** 618–21 (2004).

34. Rothemund, P. W. K. Folding DNA to create nanoscale shapes and patterns. *Nature* **440,** 297–302 (2006).

35. Kick, B., Praetorius, F., Dietz, H. & Weuster-Botz, D. Efficient Production of Single-Stranded Phage DNA as Scaffolds for DNA Origami. *Nano Lett.* **15,** 4672–4676 (2015).

36. Brown, S. *et al.* An easy-to-prepare mini-scaffold for DNA origami. *Nanoscale* **7,** 16621–16624 (2015).

37. McLaughlin, C. K., Hamblin, G. D., Aldaye, F. A., Yang, H. & Sleiman, H. F. A facile, modular and high yield method to assemble three-dimensional DNA structures. *Chem. Commun. (Camb).* **47,** 8925–7 (2011).

38. Kuzuya, A. & Komiyama, M. Design and construction of a box-shaped 3D-DNA origami. *Chem. Commun. (Camb).* 4182–4 (2009). doi:10.1039/b907800b

39. Ke, Y. *et al.* Scaffolded DNA origami of a DNA tetrahedron molecular container. *Nano Lett.* **9,** 2445–7 (2009).

40. Endo, M., Hidaka, K., Kato, T., Namba, K. & Sugiyama, H. DNA prism structures constructed by folding of multiple rectangular arms. *J. Am. Chem. Soc.* **131,** 15570–1 (2009).

41. Andersen, E. S. *et al.* Self-assembly of a nanoscale DNA box with a controllable lid. *Nature* **459,** 73–6 (2009).

42. Douglas, S. M. *et al.* Self-assembly of DNA into nanoscale three-dimensional shapes. *Nature* **459,** 414–8 (2009).

43. Sobczak, J.-P. J., Martin, T. G., Gerling, T. & Dietz, H. Rapid folding of DNA into nanoscale shapes at constant temperature. *Science (80-.).* **338,** 1458–1461 (2012).

44. Douglas, S. M. *et al.* Self-assembly of DNA into nanoscale three-dimensional shapes. *Nature* **459,** 414–418 (2009).

45. Dietz, H., Douglas, S. M. & Shih, W. M. Folding DNA into twisted and curved nanoscale shapes. *Science* **325,** 725–30 (2009).

46. Liedl, T., Högberg, B., Tytell, J., Ingber, D. E. & Shih, W. M. Self-assembly of three-dimensional prestressed tensegrity structures from DNA. *Nat Nanotechnol* **5,** 520–524 (2010).

47. Douglas, S. M. *et al.* Rapid prototyping of 3D DNA-origami shapes with caDNAno. *Nucleic Acids Res.* **37,** 5001–6 (2009).

48. Castro, C. E. *et al.* A primer to scaffolded DNA origami. *Nat. Methods* **8,** 221–9 (2011).

49. Claridge, S. A. *et al.* Enzymatic ligation creates discrete multinanoparticle building blocks for self-assembly. *J. Am. Chem. Soc.* **130,** 9598–605 (2008).

50. Li, Y. *et al.* Controlled assembly of dendrimer-like DNA. *Nat. Mater.* **3,** 38–42 (2004).

51. Lin, C., Xie, M., Chen, J. J. L., Liu, Y. & Yan, H. Rolling-circle amplification of a DNA nanojunction. *Angew. Chem. Int. Ed. Engl.* **45,** 7537–9 (2006).

52. Hamblin, G. D., Carneiro, K. M. M., Fakhoury, J. F., Bujold, K. E. & Sleiman, H. F. Rolling circle amplification-templated DNA nanotubes show increased stability and cell penetration ability. *J. Am. Chem. Soc.* **134,** 2888–91 (2012).

53. Carneiro, K. M. M. *et al.* Stimuli-responsive organization of block copolymers on DNA

nanotubes. *Chem. Sci.* **3,** 1980 (2012).

54. Hamblin, G. D. *et al.* Simple design for DNA nanotubes from a minimal set of unmodified strands: rapid, room-temperature assembly and readily tunable structure. *ACS Nano* **7,** 3022–8 (2013).

55. Lin, C. *et al.* In vivo cloning of artificial DNA nanostructures. *Proc. Natl. Acad. Sci. U. S. A.* **105,** 17626–31 (2008).

56. Anderson, J. P., Reynolds, B. L., Baum, K. & Williams, J. G. Fluorescent structural DNA nanoballs functionalized with phosphate-linked nucleotide triphosphates. *Nano Lett.* **10,** 788–92 (2010).

57. Zhu, G. *et al.* Noncanonical self-assembly of multifunctional DNA nanoflowers for biomedical applications. *J. Am. Chem. Soc.* **135,** 16438–45 (2013).

58. Ouyang, X. *et al.* Self-assembly of DNA-based drug delivery nanocarriers with rolling circle amplification. *Methods* **67,** 198–204 (2014).

59. Hu, R. *et al.* DNA nanoflowers for multiplexed cellular imaging and traceable targeted drug delivery. *Angew. Chem. Int. Ed. Engl.* **53,** 5821–6 (2014).

60. Ouyang, X. *et al.* Rolling circle amplification-based DNA origami nanostructrures for intracellular delivery of immunostimulatory drugs. *Small* **9,** 3082–7 (2013).

61. Ma, Y. *et al.* RCA strands as scaffolds to create nanoscale shapes by a few staple strands. *J. Am. Chem. Soc.* **135,** 2959–62 (2013).

62. Hong, C. A., Jang, B., Jeong, E. H., Jeong, H. & Lee, H. Self-assembled DNA nanostructures prepared by rolling circle amplification for the delivery of siRNA conjugates. *Chem. Commun. (Camb).* 1–3 (2014). doi:10.1039/c4cc03834g

63. Menacher, F., Stepanenko, V., Würthner, F. & Wagenknecht, H.-A. Assembly of DNA triangles mediated by perylene bisimide caps. *Chemistry* **17,** 6683–8 (2011).

64. Edwardson, T. G. W., Carneiro, K. M. M., McLaughlin, C. K., Serpell, C. J. & Sleiman, H. F. Site-specific positioning of dendritic alkyl chains on DNA cages enables their geometry-dependent self-assembly. *Nat. Chem.* **5,** 868–75 (2013).

65. Lee, J. K., Jung, Y. H., Tok, J. B.-H. & Bao, Z. Syntheses of organic molecule-DNA

hybrid structures. *ACS Nano* **5,** 2067–74 (2011).

66. Wilner, O. I. & Willner, I. Functionalized DNA nanostructures. *Chem. Rev.* **112,** 2528–56 (2012).

67. Saccà, B. & Niemeyer, C. M. Functionalization of DNA nanostructures with proteins. *Chem. Soc. Rev.* **40,** 5910 (2011).

68. Cohen, J. D., Sadowski, J. P. & Dervan, P. B. Programming multiple protein patterns on a single DNA nanostructure. *J. Am. Chem. Soc.* **130,** 402–3 (2008).

69. Park, S. H. *et al.* Programmable DNA self-assemblies for nanoscale organization of ligands and proteins. *Nano Lett.* **5,** 729–33 (2005).

70. Voigt, N. V *et al.* Single-molecule chemical reactions on DNA origami. *Nat. Nanotechnol.* **5,** 200–3 (2010).

71. Yan, H., Park, S. H., Finkelstein, G., Reif, J. H. & LaBean, T. H. DNA-templated self-assembly of protein arrays and highly conductive nanowires. *Science* **301,** 1882–4 (2003).

72. Kuzuya, A. *et al.* Precisely programmed and robust 2D streptavidin nanoarrays by using periodical nanometer-scale wells embedded in DNA origami assembly. *Chembiochem* **10,** 1811–5 (2009).

73. Numajiri, K., Kimura, M., Kuzuya, A. & Komiyama, M. Stepwise and reversible nanopatterning of proteins on a DNA origami scaffold. *Chem. Commun. (Camb).* **46,** 5127–9 (2010).

74. Shen, W., Zhong, H., Neff, D. & Norton, M. L. NTA directed protein nanopatterning on DNA Origami nanoconstructs. *J Am Chem Soc* **131,** 6660–6661 (2009).

75. Goodman, R. P. *et al.* A facile method for reversibly linking a recombinant protein to DNA. *Chembiochem* **10,** 1551–7 (2009).

76. Lata, S. & Piehler, J. Stable and functional immobilization of histidine-tagged proteins via multivalent chelator headgroups on a molecular poly(ethylene glycol) brush. *Anal. Chem.* **77,** 1096–105 (2005).

77. Mitchell, N., Ebner, A., Hinterdorfer, P., Tampé, R. & Howorka, S. Chemical tags

mediate the orthogonal self-assembly of DNA duplexes into supramolecular structures. *Small* **6,** 1732–5 (2010).

78. Lee, J. H., Wong, N. Y., Tan, L. H., Wang, Z. & Lu, Y. Controlled alignment of multiple proteins and nanoparticles with nanometer resolution via backbone-modified phosphorothioate DNA and bifunctional linkers. *J. Am. Chem. Soc.* **132,** 8906–8 (2010).

79. Wong, N. Y., Zhang, C., Tan, L. H. & Lu, Y. Site-specific attachment of proteins onto a 3D DNA tetrahedron through backbone-modified phosphorothioate DNA. *Small* **7,** 1427–30 (2011).

80. Perrault, S. D. & Shih, W. M. Virus-inspired membrane encapsulation of DNA nanostructures to achieve in vivo stability. *ACS Nano* **8,** 5132–5140 (2014).

81. Zhang, Z., Yang, Y., Pincet, F., Llaguno, M. C. & Lin, C. Placing and shaping liposomes with reconfigurable DNA nanocages. *Nat. Chem.* **9,** 653–659 (2017).

82. Burns, J. R., Stulz, E. & Howorka, S. Self-assembled DNA nanopores that span lipid bilayers. *Nano Lett.* **13,** 2351–6 (2013).

83. Burns, J. R. *et al.* Lipid-bilayer-spanning DNA nanopores with a bifunctional porphyrin anchor. *Angew. Chem. Int. Ed. Engl.* **52,** 12069–72 (2013).

84. Langecker, M. *et al.* Synthetic lipid membrane channels formed by designed DNA nanostructures. *Science* **338,** 932–6 (2012).

85. Bell, N. A. W. *et al.* DNA origami nanopores. *Nano Lett.* **12,** 512–7 (2012).

86. Thacker, V. V. *et al.* DNA origami based assembly of gold nanoparticle dimers for surface-enhanced Raman scattering. *Nat. Commun.* **5,** 1–7 (2014).

87. Kuzyk, A. *et al.* Reconfigurable 3D plasmonic metamolecules. *Nat. Mater.* **13,** 862–866 (2014).

88. Pilo-Pais, M., Acuna, G. P., Tinnefeld, P. & Liedl, T. Sculpting Light by Arranging Optical Components with DNA Nanostructures. *MRS Bull.* 936–942 (2017). doi:10.1557/mrs.2017.278

89. Kiick, K. L., Saxon, E., Tirrell, D. A. & Bertozzi, C. R. Incorporation of azides into recombinant proteins for chemoselective modification by the Staudinger ligation. *Proc.*

Natl. Acad. Sci. **99,** 19–24 (2002).

90. Keppler, A. *et al.* A general method for the covalent labeling of fusion proteins with small molecules in vivo. *Nat. Biotechnol.* **21,** 86–89 (2003).

91. Gautier, A. *et al.* An Engineered Protein Tag for Multiprotein Labeling in Living Cells. *Chem. Biol.* **15,** 128–136 (2008).

92. Bernardinelli, G. & Högberg, B. Entirely enzymatic nanofabrication of DNA-protein conjugates. *Nucleic Acids Res.* **45,** e160 (2017).

93. Busuttil, K., Rotaru, A., Dong, M., Besenbacher, F. & Gothelf, K. V. Transfer of a protein pattern from self-assembled DNA origami to a functionalized substrate. *Chem Commun* **49,** 1927–1929 (2013).

94. Los, G. V. *et al.* HaloTag: A Novel Protein Labeling Technology for Cell Imaging and Protein Analysis. *ACS Chem. Biol.* **3,** 373–382 (2008).

95. Küchler, A., Yoshimoto, M., Luginbühl, S., Mavelli, F. & Walde, P. Enzymatic reactions in confined environments. *Nat. Nanotechnol.* **11,** 409–420 (2016).

96. Cao, L. Introduction: Immobilized Enzymes: Past, Present and Prospects . in *Carrier-bound Immobilized Enzymes* 1–52 (Wiley-VCH Verlag GmbH & Co. KGaA, 2005). doi:10.1002/3527607668.ch1

97. Mateo, C., Palomo, J. M., Fernandez-Lorente, G., Guisan, J. M. & Fernandez-Lafuente, R. Improvement of enzyme activity, stability and selectivity via immobilization techniques. *Enzyme Microb. Technol.* **40,** 1451–1463 (2007).

98. Johnson, B. J., Russ Algar, W., Malanoski, A. P., Ancona, M. G. & Medintz, I. L. Understanding enzymatic acceleration at nanoparticle interfaces: Approaches and challenges. *Nano Today* **9,** 102–131 (2014).

99. Cao, L. Adsorption-based Immobilization. in *Carrier-bound Immobilized Enzymes* 53–168 (Wiley-VCH Verlag GmbH & Co. KGaA, 2005). doi:10.1002/3527607668.ch2

100. Agapakis, C. M., Boyle, P. M. & Silver, P. A. Natural strategies for the spatial optimization of metabolism in synthetic biology. *Nat. Chem. Biol.* **8,** 527–535 (2012).

101. Conrado, R. J., Varner, J. D. & DeLisa, M. P. Engineering the spatial organization of

metabolic enzymes: mimicking nature's synergy. *Curr. Opin. Biotechnol.* **19,** 492–499 (2008).

102. Kerfeld, C. a, Heinhorst, S. & Cannon, G. C. Bacterial microcompartments. *Annu. Rev. Microbiol.* **64,** 391–408 (2010).

103. Yeates, T. O., Thompson, M. C. & Bobik, T. A. The protein shells of bacterial microcompartment organelles. *Curr. Opin. Struct. Biol.* **21,** 223–231 (2011).

104. Tsai, Y. *et al.* Structural Analysis of CsoS1A and the Protein Shell of the Halothiobacillus neapolitanus Carboxysome. *PLoS Biol.* **5,** e144 (2007).

105. Milani, M., Pesce, A., Bolognesi, M., Bocedi, A. & Ascenzi, P. Substrate channeling: Molecular bases. *Biochem. Mol. Biol. Educ.* **31,** 228–233 (2003).

106. Wheeldon, I. *et al.* Substrate channelling as an approach to cascade reactions. *Nat. Chem.* **8,** 299–309 (2016).

107. Hyde, C. C., Ahmed, S. A., Padlan, E. A., Miles, E. W. & Davies, D. R. Three-dimensional structure of the tryptophan synthase alpha 2 beta 2 multienzyme complex from Salmonella typhimurium. *J. Biol. Chem.* **263,** 17857–71 (1988).

108. Dunn, M. F. *et al.* The tryptophan synthase bienzyme complex transfers indole between the .alpha.- and .beta.-sites via a 25-30 .ANG. long tunnel. *Biochemistry* **29,** 8598–8607 (1990).

109. Elcock, A. H., Potter, M. J., Matthews, D. A., Knighton, D. R. & McCammon, J. A. Electrostatic Channeling in the Bifunctional Enzyme Dihydrofolate Reductase-thymidylate Synthase. *J. Mol. Biol.* **262,** 370–374 (1996).

110. Perham, R. N. Swinging Arms and Swinging Domains in Multifunctional Enzymes: Catalytic Machines for Multistep Reactions. *Annu. Rev. Biochem.* **69,** 961–1004 (2000).

111. Asturias, F. J. *et al.* Structure and molecular organization of mammalian fatty acid synthase. **12,** 225 (2005).

112. Brignole, E. J., Smith, S. & Asturias, F. J. Conformational Flexibility of Metazoan Fatty Acid Synthase Enables Catalysis. *Nature structural & molecular biology* **16,** 190–197 (2009).

113. Grossi, G., Dalgaard Ebbesen Jepsen, M., Kjems, J. & Andersen, E. S. Control of enzyme reactions by a reconfigurable DNA nanovault. *Nat. Commun.* **8,** 992 (2017).

114. Linko, V. *et al.* DNA-Based Enzyme Reactors and Systems. *Nanomaterials* **6,** 139 (2016).

115. Zhao, Z. *et al.* Nanocaged enzymes with enhanced catalytic activity and increased stability against protease digestion. *Nat. Commun.* **7,** 10619 (2016).

116. Wilner, O. I., Shimron, S., Weizmann, Y., Wang, Z. & Willner, I. Self-assembly of enzymes on DNA scaffolds: en route to biocatalytic cascades and the synthesis of metallic nanowires. *Nano Lett.* **9,** 2040–3 (2009).

117. Wilner, O. I. *et al.* Enzyme cascades activated on topologically programmed DNA scaffolds. *Nat. Nanotechnol.* **4,** 249–54 (2009).

118. Timm, C. & Niemeyer, C. M. Assembly and purification of enzyme-functionalized DNA origami structures. *Angew. Chemie - Int. Ed.* **54,** 6745–6750 (2015).

119. Niemeyer, C. M., Koehler, J. & Wuerdemann, C. DNA-directed assembly of bienzymic complexes from in vivo biotinylated NAD(P)H:FMN oxidoreductase and luciferase. *Chembiochem* **3,** 242–5 (2002).

120. Fu, J. *et al.* Assembly of multienzyme complexes on DNA nanostructures. *Nat. Protoc.* **11,** 2243–2273 (2016).

121. Numajiri, K., Yamazaki, T., Kimura, M., Kuzuya, A. & Komiyama, M. Discrete and active enzyme nanoarrays on DNA origami scaffolds purified by affinity tag separation. *J. Am. Chem. Soc.* **132,** 9937–9939 (2010).

122. Yamazaki, T., Heddle, J. G., Kuzuya, A. & Komiyama, M. Orthogonal enzyme arrays on a DNA origami scaffold bearing size-tunable wells. *Nanoscale* **6,** 9122–9126 (2014).

123. Fu, J., Liu, M., Liu, Y., Woodbury, N. W. & Yan, H. Interenzyme substrate diffusion for an enzyme cascade organized on spatially addressable DNA nanostructures. *J. Am. Chem. Soc.* **134,** 5516–9 (2012).

124. Ngo, T. A., Nakata, E., Saimura, M. & Morii, T. Spatially Organized Enzymes Drive Cofactor-Coupled Cascade Reactions. *J. Am. Chem. Soc.* **138,** 3012–3021 (2016).

125. Liu, M. *et al.* A Three-Enzyme Pathway with an Optimised Geometric Arrangement to Facilitate Substrate Transfer. *ChemBioChem* 1097–1101 (2016). doi:10.1002/cbic.201600103

126. Fu, J. *et al.* Multi-enzyme complexes on DNA scaffolds capable of substrate channelling with an artificial swinging arm. *Nat. Nanotechnol.* **9,** 531–6 (2014).

127. Wang, D. *et al.* A switchable DNA origami nanochannel for regulating molecular transport at the nanometer scale. *Nanoscale* **8,** 3944–8 (2016).

128. Müller, J. & Niemeyer, C. M. DNA-directed assembly of artificial multienzyme complexes. *Biochem. Biophys. Res. Commun.* **377,** 62–7 (2008).

129. Wang, Z. Z.-G., Wilner, O. I. O. & Willner, I. Self-Assembly of Aptamer− Circular DNA Nanostructures for Controlled Biocatalysis. *Nano Lett.* **9,** 4098–102 (2009).

130. Wilner, O. I. *et al.* Enzyme cascades activated on topologically programmed DNA scaffolds. *Nat. Nanotechnol.* **4,** 249–54 (2009).

131. Linko, V., Eerikäinen, M. & Kostiainen, M. A. A modular DNA origami-based enzyme cascade nanoreactor. *Chem. Commun.* **51,** 5351–5354 (2015).

132. Liu, M. *et al.* A DNA tweezer-actuated enzyme nanoreactor. *Nat. Commun.* **4,** 2127 (2013).

133. Xin, L., Zhou, C., Yang, Z. & Liu, D. Regulation of an enzyme cascade reaction by a DNA machine. *Small* **9,** 3088–91 (2013).

134. Fu, J. *et al.* Multi-enzyme complexes on DNA scaffolds capable of substrate channelling with an artificial swinging arm. *Nat. Nanotechnol.* **9,** 531–536 (2014).

135. Lin, J.-L. & Wheeldon, I. Kinetic Enhancements in DNA–Enzyme Nanostructures Mimic the Sabatier Principle. *ACS Catal.* **3,** 560–564 (2013).

136. van Santen, R. A. Molecular Catalytic Kinetics Concepts. in *Novel Concepts in Catalysis and Chemical Reactors* 1–30 (Wiley-VCH Verlag GmbH & Co. KGaA, 2010). doi:10.1002/9783527630882.ch1

137. Zhang, Y., Tsitkov, S. & Hess, H. Proximity does not contribute to activity enhancement in the glucose oxidase–horseradish peroxidase cascade. *Nat. Commun.* **7,** 13982 (2016).

138. Idan, O. & Hess, H. Origins of activity enhancement in enzyme cascades on scaffolds. *ACS Nano* **7,** 8658–8665 (2013).

139. Rodrigues, R. C., Ortiz, C., Berenguer-Murcia, Á., Torres, R. & Fernández-Lafuente, R. Modifying enzyme activity and selectivity by immobilization. *Chem. Soc. Rev.* **42,** 6290–6307 (2013).

140. Bauler, P., Huber, G., Leyh, T. & McCammon, J. A. Channeling by proximity: The catalytic advantages of active site colocalization using brownian dynamics. *J. Phys. Chem. Lett.* **1,** 1332–1335 (2010).

141. Solovev, A. A., Sanchez, S., Pumera, M., Mei, Y. F. & Schmidt, O. C. Magnetic control of tubular catalytic microbots for the transport, assembly, and delivery of micro-objects. *Adv. Funct. Mater.* **20,** 2430–2435 (2010).

142. Sengupta, S. *et al.* Enzyme molecules as nanomotors. *J. Am. Chem. Soc.* **135,** 1406–1414 (2013).

143. Hong, Y., Velegol, D., Chaturvedi, N. & Sen, A. Biomimetic behavior of synthetic particles: from microscopic randomness to macroscopic control. *Phys. Chem. Chem. Phys.* **12,** 1423–1435 (2010).

144. Dey, K. K. *et al.* Micromotors Powered by Enzyme Catalysis. *Nano Lett.* **15,** 8311–8315 (2015).

145. Ma, X. *et al.* Enzyme-Powered Hollow Mesoporous Janus Nanomotors. *Nano Lett.* **15,** 7043–7050 (2015).

146. Ma, X., Hortelão, A. C., Patiño, T. & Sánchez, S. Enzyme Catalysis to Power Micro/Nanomachines. *ACS Nano* **10,** 9111–9122 (2016).

147. Ma, X., Wang, X., Hahn, K. & Sánchez, S. Motion Control of Urea-Powered Biocompatible Hollow Microcapsules. *ACS Nano* **10,** 3597–3605 (2016).

148. Santiago, I. Nanoscale active matter matters: Challenges and opportunities for self-propelled nanomotors. *Nano Today* 1–5 (2018). doi:10.1016/j.nantod.2018.01.001

149. Du, C. J., Rios-Solis, L., Ward, J. M., Dalby, P. A. & Lye, G. J. Evaluation of CV2025 ω-transaminase for the bioconversion of lignin breakdown products into value-added

chemicals: Synthesis of vanillylamine from vanillin. *Biocatal. Biotransformation* **32,** 302–313 (2014).

150. Lichman, B. R. *et al.* One-pot triangular chemoenzymatic cascades for the syntheses of chiral alkaloids from dopamine. *Green Chem.* **17,** 852–855 (2015).

151. Lichman, B. R. *et al.* One-pot triangular chemoenzymatic cascades for the syntheses of chiral alkaloids from dopamine. *Green Chem.* **17,** 852–855 (2015).

152. Jeong, H. *et al.* Genome Sequences of Escherichia coli B strains REL606 and BL21(DE3). *J. Mol. Biol.* **394,** 644–652 (2009).

153. Nečas, D. & Klapetek, P. Gwyddion: An open-source software for SPM data analysis. *Cent. Eur. J. Phys.* **10,** 181–188 (2012).

154. Tarantino, N. *et al.* Tnf and il-1 exhibit distinct ubiquitin requirements for inducing NEMO-IKK supramolecular structures. *J. Cell Biol.* **204,** 231–245 (2014).

155. He, Y. *et al.* Hierarchical self-assembly of DNA into symmetric supramolecular polyhedra. *Nature* **452,** 198–201 (2008).

156. Benson, E. *et al.* DNA rendering of polyhedral meshes at the nanoscale. *Nature* **523,** 441–444 (2015).

157. Zhang, C. *et al.* Symmetry controls the face geometry of DNA polyhedra. *J Am Chem Soc* **131,** 1413–1415 (2009).

158. Mohamad, N. R., Marzuki, N. H. C., Buang, N. A., Huyop, F. & Wahab, R. A. An overview of technologies for immobilization of enzymes and surface analysis techniques for immobilized enzymes. *Biotechnol. Biotechnol. Equip.* **29,** 205–220 (2015).

159. Moehlenbrock, M. J. & Minteer, S. D. Enzyme Stabilization and Immobilization. **679,** 1–7 (2011).

160. Acharya, G., Mitra, A. K. & Cholkar, K. Chapter 10 - Nanosystems for Diagnostic Imaging, Biodetectors, and Biosensors. in *Emerging Nanotechnologies for Diagnostics, Drug Delivery and Medical Devices* (eds. Mitra, A. K., Cholkar, K. & Mandal, A.) 217–248 (Elsevier, 2017). doi:https://doi.org/10.1016/B978-0-323-42978-8.00010-3

161. Cooney, M. J. Kinetic Measurements for Enzyme Immobilization. in *Enzyme Stabilization and Immobilization: Methods and Protocols* (ed. Minteer, S. D.) 207–225 (Humana Press, 2011). doi:10.1007/978-1-60761-895-9_17

162. Pinheiro, A. V, Han, D., Shih, W. M. & Yan, H. Challenges and opportunities for structural DNA nanotechnology. *Nat Nanotechnol* **6,** 763–772 (2012).

163. Seeman, N. C. Nanomaterials based on DNA. *Annu Rev Biochem* **79,** 65–87 (2010).

164. Grossi, G., Jaekel, A., Andersen, E. S. & Saccà, B. Enzyme-functionalized DNA nanostructures as tools for organizing and controlling enzymatic reactions. *MRS Bull.* **42,** 920–924 (2017).

165. Yang, Y. R. *et al.* 2D Enzyme Cascade Network with Efficient Substrate Channeling by Swinging Arms. *ChemBioChem* 2–7 (2017). doi:10.1002/cbic.201700613

166. Yamazaki, T., Heddle, J. G., Kuzuya, A. & Komiyama, M. Orthogonal enzyme arrays on a DNA origami scaffold bearing size-tunable wells. *Nanoscale* **6,** 9122–9126 (2014).

167. Brodin, J. D., Sprangers, A. J., McMillan, J. R. & Mirkin, C. A. DNA-Mediated Cellular Delivery of Functional Enzymes. *J. Am. Chem. Soc.* **137,** 14838–14841 (2015).

168. Freeman, R., Sharon, E., Tel-Vered, R. & Willner, I. Supramolecular cocaine-aptamer complexes activate biocatalytic cascades. *J. Am. Chem. Soc.* **131,** 5028–9 (2009).

169. Freeman, R., Sharon, E., Teller, C. & Willner, I. Control of biocatalytic transformations by programmed DNA assemblies. *Chemistry* **16,** 3690–8 (2010).

170. Liu, Y. *et al.* Biomimetic enzyme nanocomplexes and their use as antidotes and preventive measures for alcohol intoxication. *Nat. Nanotechnol.* **8,** 187–92 (2013).

171. Zhang, F., Nangreave, J., Liu, Y. & Yan, H. Structural DNA Nanotechnology: State of the Art and Future Perspective. *J. Am. Chem. Soc.* (2014). doi:10.1021/ja505101a

172. Drmanac, R. *et al.* Human genome sequencing using unchained base reads on self-assembling DNA nanoarrays. *Science* **327,** 78–81 (2010).

173. Bateman, R. C. & Evans, J. A. Using the Glucose Oxidase/Peroxidase System in Enzyme Kinetics. *J. Chem. Educ.* **72,** A240 (1995).

174. Dueber, J. E. *et al.* Synthetic protein scaffolds provide modular control over metabolic

flux. *Nat. Biotechnol.* **27,** 753–9 (2009).

175. Lee, H., DeLoache, W. C. & Dueber, J. E. Spatial organization of enzymes for metabolic engineering. *Metab. Eng.* **14,** 242–251 (2012).

176. Castellana, M. *et al.* Enzyme clustering accelerates processing of intermediates through metabolic channeling. *Nat. Biotechnol.* **32,** (2014).

177. Ali, M. M. *et al.* Rolling circle amplification: a versatile tool for chemical biology, materials science and medicine. *Chem. Soc. Rev.* **43,** 3324 (2014).

178. Ali, M. M. *et al.* Rolling circle amplification: a versatile tool for chemical biology, materials science and medicine. *Chem. Soc. Rev.* **43,** 3324–41 (2014).

179. Hermanson, G. T. The Reactions of Bioconjugation. in *Bioconjugate Techniques* 229–258 (Elsevier, 2013).

180. Hermanson, G. T. Heterobifunctional Crosslinkers. in *Bioconjugate Techniques* 299–339 (Elsevier, 2013).

181. *Enzyme assays : a practical approach / edited by Robert Eisenthal and Michael Danson. Enzyme assays : a practical approach* (Oxford University Press, 2001).

182. Shih, J. H. C., Shannon, L. M., Kay, E. & Lew, J. Y. Peroxidase Isoenzymes from Horseradish Roots IV. Structural relationships. *J. Biol. Chem.* **242,** 55 (1967).

183. Kay, E., Shannon, L. M. & Lew, J. Y. Peroxidase Isozymes from Horseradish Roots II. catalytic properties. *J. Biol. Chem.* **242,** 55 (1967).

184. Morawski, B. *et al.* Functional expression of horseradish peroxidase in Saccharomyces cerevisiae and Pichia pastoris. *Protein Eng.* **13,** 377–384 (2000).

185. Wong, C. M., Wong, K. H. & Chen, X. D. Glucose oxidase: natural occurrence, function, properties and industrial applications. *Appl. Microbiol. Biotechnol.* **78,** 927–938 (2008).

186. Lavery, C. B. *et al.* Purification of Peroxidase from Horseradish (Armoracia rusticana) Roots. *J. Agric. Food Chem.* **58,** 8471–8476 (2010).

187. Guo, S. *et al.* One of the possible mechanisms for the inhibition effect of Tb(III) on peroxidase activity in horseradish (Armoracia rusticana) treated with Tb(III). *JBIC J.*

Biol. Inorg. Chem. **13,** 587–597 (2008).

188. Zakharova, G. S., Uporov, I. V & Tishkov, V. I. Horseradish peroxidase: Modulation of properties by chemical modification of protein and heme. *Biochem.* **76,** 1391–1401 (2011).

189. Hagel, J. M. & Facchini, P. J. Benzylisoquinoline alkaloid metabolism: a century of discovery and a brave new world. *Plant Cell Physiol.* **54,** 647–72 (2013).

190. Desgagné-Penix, I., Facchini, P. J. & Desgagn, I. Benzylisoquinoline Alkaloid Biosynthesis. in *Plant Metabolism and Biotechnology* 241–261 (Wiley-Blackwell, 2011). doi:10.1002/9781119991311.ch9

191. Glaucine A2 - Aronson, J.K. BT - Meyler's Side Effects of Drugs: The International Encyclopedia of Adverse Drug Reactions and Interactions (Fifteenth Edition). 1510 (2006). doi:https://doi.org/10.1016/B0-44-451005-2/01336-X

192. Winzer, T. *et al.* A Papaver somniferum 10-Gene Cluster for Synthesis of the Anticancer Alkaloid Noscapine. *Science (80-.).* **336,** 1704–1708 (2012).

193. Trost, B. M. & Tang, W. Enantioselective synthesis of (-)-codeine and (-)-morphine. *J. Am. Chem. Soc.* **124,** (2002).

194. Taber, D. F., Neubert, T. D. & Rheingold, A. L. Synthesis of (-)-morphine. *J. Am. Chem. Soc.* **124,** (2002).

195. Uchida, K., Yokoshima, S., Kan, T. & Fukuyama, T. Total synthesis of (+/-)-morphine. *Org. Lett.* **8,** (2006).

196. Facchini, P. J. Alkaloid biosynthesis in plants: Biochemistry, Cell Biology, Molecular Regulation, and Metabolic Engineering Applications. *Annu. Rev. Plant Physiol. Plant Mol. Biol.* **52,** 29–66 (2001).

197. Newhouse, T., Baran, P. S. & Hoffmann, R. W. The economies of synthesis. *Chem. Soc. Rev.* **38,** 3010 (2009).

198. Hao, D. C., Gu, X.-J. & Xiao, P. G. 6 - Phytochemical and biological research of Papaver pharmaceutical resources. in *Medicinal Plants* (eds. Hao, D. C., Gu, X.-J. & Xiao, P. G.) 217–251 (Woodhead Publishing, 2015). doi:https://doi.org/10.1016/B978-

0-08-100085-4.00006-2

199. Minami, H. *et al.* Microbial production of plant benzylisoquinoline alkaloids. *Proc. Natl. Acad. Sci.* **105,** 7393–7398 (2008).

200. Ato, B. F. S., Umagai, H. K., SATO, F. & KUMAGAI, H. Microbial production of isoquinoline alkaloids as plant secondary metabolites based on metabolic engineering research. *Proc. Japan Acad. Ser. B* **89,** 165–182 (2013).

201. Nakagawa, A. *et al.* A bacterial platform for fermentative production of plant alkaloids. *Nat. Commun.* **2,** 326 (2011).

202. Minami, H. Fermentative production of plant benzylisoquinoline alkaloids in microbes. *Biosci. Biotechnol. Biochem.* **77,** 1617–1622 (2013).

203. Hawkins, K. M. & Smolke, C. D. Production of benzylisoquinoline alkaloids in Saccharomyces cerevisiae. *Nat. Chem. Biol.* **4,** 564–573 (2008).

204. Fossati, E. *et al.* Reconstitution of a 10-gene pathway for synthesis of the plant alkaloid dihydrosanguinarine in Saccharomyces cerevisiae. *Nat. Commun.* **5,** 1–11 (2014).

205. Galanie, S., Thodey, K., Trenchard, I. J., Filsinger Interrante, M. & Smolke, C. D. Complete biosynthesis of opioids in yeast. *Science* **349,** 1095–100 (2015).

206. DeLoache, W. C. *et al.* An enzyme-coupled biosensor enables (S)-reticuline production in yeast from glucose. *Nat. Chem. Biol.* **11,** 465–471 (2015).

207. Alcantara, J., Bird, D. A., Franceschi, V. R. & Facchini, P. J. Sanguinarine Biosynthesis Is Associated with the Endoplasmic Reticulum in Cultured Opium Poppy Cells after Elicitor Treatment 1. *Plant Physiol.* **138,** 173–183 (2005).

208. Narcross, L., Fossati, E., Bourgeois, L., Dueber, J. E. & Martin, V. J. J. Microbial Factories for the Production of Benzylisoquinoline Alkaloids. *Trends Biotechnol.* **34,** 228–241 (2016).

209. Trenchard, I. J. & Smolke, C. D. Engineering strategies for the fermentative production of plant alkaloids in yeast. *Metab. Eng.* **30,** 96–104 (2015).

210. KIM, J.-S. *et al.* Improvement of Reticuline Productivity from Dopamine by Using Engineered *Escherichia coli*. *Biosci. Biotechnol. Biochem.* **77,** 2166–2168 (2013).

211. Jones, J. A., Toparlak, T. D. & Koffas, M. A. G. Metabolic pathway balancing and its role in the production of biofuels and chemicals. *Curr. Opin. Biotechnol.* **33,** 52–59 (2015).

212. Beaudoin, G. A. W. & Facchini, P. J. Benzylisoquinoline alkaloid biosynthesis in opium poppy. *Planta* **240,** 19–32 (2014).

213. Kaulmann, U., Smithies, K., Smith, M. E. B., Hailes, H. C. & Ward, J. M. Substrate spectrum of ω-transaminase from Chromobacterium violaceum DSM30191 and its potential for biocatalysis. *Enzyme Microb. Technol.* **41,** 628–637 (2007).

214. Kim, J.-S. *et al.* Improvement of Reticuline Productivity from Dopamine by Using Engineered Escherichia coli. *Biosci. Biotechnol. Biochem.* **77,** 2166–2168 (2013).

215. Kasner, E., Hunter, C. A., Ph, D., Kariko, K. & Ph, D. NIH Public Access. **70,** 646–656 (2013).

216. Boettcher, C., Fellermeier, M., Boettcher, C., Dräger, B. & Zenk, M. H. How human neuroblastoma cells make morphine. *Proc. Natl. Acad. Sci. U. S. A.* **102,** 8495–8500 (2005).

217. Poeaknapo, C., Schmidt, J., Brandsch, M., Dräger, B. & Zenk, M. H. Endogenous formation of morphine in human cells. *Proc. Natl. Acad. Sci. U. S. A.* **101,** 14091–14096 (2004).

218. Li, J., Rozen, I. & Wang, J. Rocket Science at the Nanoscale. *ACS Nano* **10,** 5619–5634 (2016).

219. Wang, J. *Nanomachines*. (WILEY-VCH Verlag, 2013).

220. Li, J., Esteban-Fernández de Ávila, B., Gao, W., Zhang, L. & Wang, J. Micro/nanorobots for biomedicine: Delivery, surgery, sensing, and detoxification. *Sci. Robot.* **2,** eaam6431 (2017).

221. Douglas, S. M., Bachelet, I. & Church, G. M. A Logic-Gated Nanorobot for Targeted Transport of Molecular Payloads. *Science (80-.).* **335,** 831–834 (2012).

222. Mavroidis, C., Dubey, A. & Yarmush, M. L. Molecular Machines. *Annu. Rev. Biomed. Eng.* **6,** 363–395 (2004).

223. Purcell, E. M. Life at low Reynolds number. *Am. J. Phys.* **45,** 3–11 (1977).

224. *A Dictionary of Physics*. (Oxford University Press, 2009). doi:10.1093/acref/9780199233991.001.0001

225. Wang, W., Duan, W., Ahmed, S., Mallouk, T. E. & Sen, A. Small power: Autonomous nano- and micromotors propelled by self-generated gradients. *Nano Today* **8,** 531–554 (2013).

226. Lauga, E. Life around the scallop theorem. *Soft Matter* **7,** 3060–3065 (2011).

227. Kumar, M. S. & Philominathan, P. The physics of flagellar motion of E. coli during chemotaxis. *Biophys. Rev.* **2,** 13–20 (2010).

228. Turner, L., Ryu, W. S. & Berg, H. C. Real-time imaging of fluorescent flagellar filaments. *J. Bacteriol.* **182,** 2793–2801 (2000).

229. Wang, J. *Nanomachines. Fundamentals and Applications*. *Angewandte Chemie International Edition* **53,** (2014).

230. Kopperger, E. *et al.* A self-assembled nanoscale robotic arm controlled by electric fields. *Science (80-.).* **359,** 296 LP-301 (2018).

231. Maier, A. M. *et al.* Magnetic Propulsion of Microswimmers with DNA-Based Flagellar Bundles. *Nano Lett.* **16,** 906–910 (2016).

232. Shelley, M. J. The Dynamics of Microtubule / Motor-Protein Assemblies in Biology and Physics. (2016). doi:10.1146/annurev-fluid-010814-013639

233. Houdusse, A. & Carter, A. P. Dynein Swings into Action. *Cell* **136,** 395–396 (2009).

234. Alberts, B. *et al. Molecular Biology of the Cell, Fourth Edition*. (Garland Science, 2002).

235. Delalez, N. J. Bacterial Flagella: Flagellar Motor. *eLS* (2001). doi:10.1002/9780470015902.a0000744.pub4

236. Pan, J., Li, F., Cha, T. G., Chen, H. & Choi, J. H. Recent progress on DNA based walkers. *Curr. Opin. Biotechnol.* **34,** 56–64 (2015).

237. Cha, T. G. *et al.* Design Principles of DNA Enzyme-Based Walkers: Translocation Kinetics and Photoregulation. *J. Am. Chem. Soc.* **137,** 9429–9437 (2015).

238. Bath, J., Green, S. J. & Turberfield, A. J. A free-running DNA motor powered by a nicking enzyme. *Angew. Chemie - Int. Ed.* **44,** 4358–4361 (2005).

239. Tian, Y., He, Y., Chen, Y., Yin, P. & Mao, C. A DNAzyme that walks processively and autonomously along a one-dimensional track. *Angew. Chemie - Int. Ed.* **44,** 4355–4358 (2005).

240. Bath, J., Green, S. J., Allen, K. E. & Turberfield, A. J. Mechanism for a directional, processive, and reversible DNA motor. *Small* **5,** 1513–1516 (2009).

241. Wickham, S. F. J. *et al.* Direct observation of stepwise movement of a synthetic molecular transporter. *Nat. Nanotechnol.* **6,** 166–9 (2011).

242. Genot, A. J., Zhang, D. Y., Bath, J. & Turberfield, A. J. Remote toehold: a mechanism for flexible control of DNA hybridization kinetics. *J Am Chem Soc* **133,** 2177–2182 (2011).

243. Zhang, D. Y. & Winfree, E. Control of DNA strand displacement kinetics using toehold exchange. *J Am Chem Soc* **131,** 17303–17314 (2009).

244. Green, S. J., Lubrich, D. & Turberfield, A. J. DNA hairpins: fuel for autonomous DNA devices. *Biophys J* **91,** 2966–2975 (2006).

245. Shin, J. & Pierce, N. A. A synthetic DNA walker for molecular transport. *J Am Chem Soc* **126,** 10834–10835 (2004).

246. Omabegho, T., Sha, R. & Seeman, N. C. A bipedal DNA Brownian motor with coordinated legs. *Science (80-.).* **324,** 67–71 (2009).

247. Yehl, K. *et al.* High-speed DNA-based rolling motors powered by RNase H. *Nat Nano* **11,** 184–190 (2016).

248. Cha, T.-G. *et al.* A synthetic DNA motor that transports nanoparticles along carbon nanotubes. *Nat. Nanotechnol.* **9,** 39–43 (2013).

249. Zhao, X. *et al.* Substrate-driven chemotactic assembly in an enzyme cascade. *Nat. Chem.* 1–7 (2017). doi:10.1038/nchem.2905

250. Riedel, C. *et al.* The heat released during catalytic turnover enhances the diffusion of an enzyme. *Nature* **517,** 227–230 (2015).

251. Golestanian, R. Enhanced Diffusion of Enzymes that Catalyze Exothermic Reactions. **108102,** 1–5 (2015).

252. Golestanian, R. & Ajdari, A. Stochastic low Reynolds number swimmers. *J. Phys. Condens. Matter* **21,** 204104 (2009).

253. Muddana, H. S. *et al.* Substrate Catalysis Enhances Single-Enzyme Diffusion. 2110–2111 (2010). doi:10.1039/b917741h.(16)

254. Joseph, A. *et al.* Chemotactic synthetic vesicles : Design and applications in blood-brain barrier crossing. (2017).

255. Abdelmohsen, L. K. E. A. *et al.* Dynamic Loading and Unloading of Proteins in Polymeric Stomatocytes: Formation of an Enzyme-Loaded Supramolecular Nanomotor. *ACS Nano* **10,** 2652–2660 (2016).

256. Paxton, W. F. *et al.* Catalytic Nanomotors: Autonomous Movement of Striped Nanorods. *J. Am. Chem. Soc.* **126,** 13424–13431 (2004).

257. Gao, W. *et al.* Polymer-based tubular microbots: role of composition and preparation. *Nanoscale* **4,** 2447–2453 (2012).

258. Malloy, A. Count, size and visualize nanoparticles. *Mater. Today* **14,** 170–173 (2011).

259. Filipe, V., Hawe, A. & Jiskoot, W. Critical evaluation of nanoparticle tracking analysis (NTA) by NanoSight for the measurement of nanoparticles and protein aggregates. *Pharm. Res.* **27,** 796–810 (2010).

260. Frisken, B. J. Revisiting the method of cumulants for the analysis of dynamic light-scattering data. *Appl. Opt.* **40,** 4087 (2001).

261. Kusumi, A., Sako, Y. & Yamamoto, M. Confined Lateral Diffusion of Membrane-Receptors as Studied by Single-Particle Tracking (Nanovid Microscopy) - Effects of Calcium-Induced Differentiation in Cultured Epithelial-Cells. *Biophys. J.* **65,** 2021–2040 (1993).

262. Jung, C., Allen, P. B. & Ellington, A. D. A stochastic DNA walker that traverses a microparticle surface. *Nat. Nanotechnol.* **11,** 157–163 (2015).

263. Yin, P., Yan, H., Daniell, X. G., Turberfield, A. J. & Reif, J. H. A unidirectional DNA

walker that moves autonomously along a track. *Angew. Chemie - Int. Ed.* **43,** 4906–4911 (2004).

264. Sherman, W. B. & Seeman, N. C. A Precisely Controlled DNA Biped Walking Device. *Nano Lett.* **4,** 1801 (2004).

265. Wickham, S. F. J. *et al.* A DNA-based molecular motor that can navigate a network of tracks. *Nat. Nanotechnol.* **7,** 169–73 (2012).

266. Sherman, W. B. & Seeman, N. C. A Precisely Controlled DNA Biped Walking Device. *Nano Lett.* **4,** 1801 (2004).

267. Turberfield, a. *et al.* DNA Fuel for Free-Running Nanomachines. *Phys Rev Lett* **90,** 118102 (2003).

268. Yang, H. & Sleiman, H. F. Templated synthesis of highly stable, electroactive, and dynamic metal-DNA branched junctions. *Angew. Chem. Int. Ed. Engl.* **47,** 2443–6 (2008).

269. Lin, C. & Yan, H. DNA nanotechnology: A cascade of activity. *Nat. Nanotechnol.* **4,** 211–2 (2009).

Appendix A

A.1 DNA Nanoball oligonucleotide sequences

Oligonucleotide name	Sequence 5’ -> 3’ (length b)
200-mer	/5Phos/TTC AAC ACATCT TCA CTC ATC TCC GAG GCG CTATAG CGC CTC GAC ACATCT ACCTAC CCT CCATCT ACT CAC ACC CACTCA CACTCA TCT CGG GTC CGA GCT CGG ACC CGT TTT TCT CCC AACTAC ACATACTCA CTT ACT TCA CTT CTC AACTTC TCC GCC GGCTGG AGC CGG CGGTAC ATA CTC AAT ACATCC ATC AA (200)
200-bridge primer	TGTGTTGAATTGATGGATGT (25)
200 S3’TAMRA	THI-ACATCTACCTACCCTCCATCZ-3' TAMDT
200 SH 3’FAM	THI-CATACTCAATACATCCATCAZ-3' FLUDT
Cy5 probe	Cy5 5’- C ATA CTC AAT ACATCC ATC A -3’ (25)
Cy3 probe	Cy3 5’- ACATCT ACCTAC CCT CCATC-3’(25)

A.2 200nt ssDNA template sequence

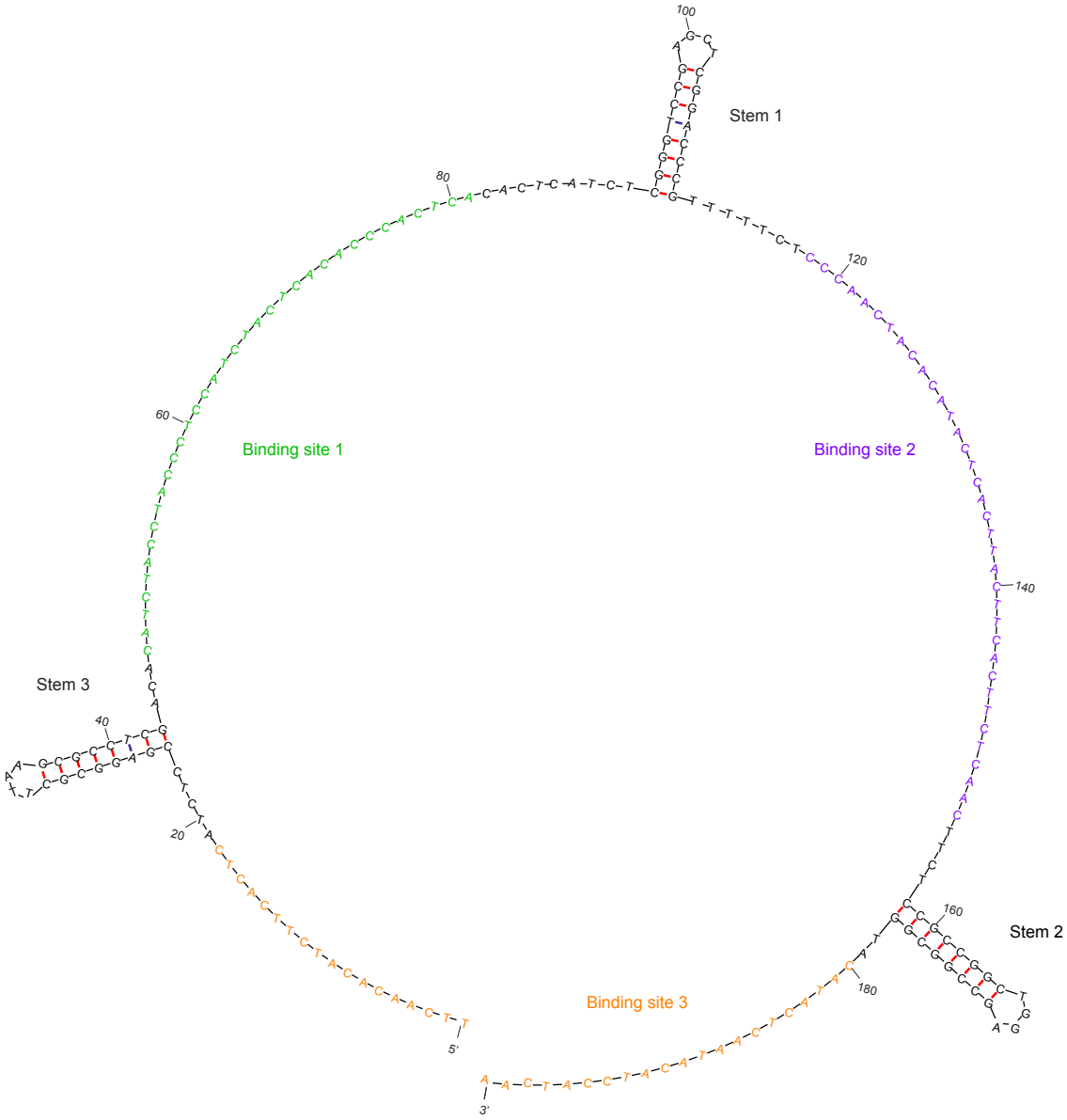

A.3 Oligonucleotides used for conjugation of TAm and NCS enzymes (Chapter 4)

Oligonucleotide name	Sequence 5' -> 3' (length bases) (MW)
200 SH cy5	[ThiC6] ACATCTACCTACCCTCCATC [cy5] (20) (7166)

A.4 Δ29TfNCS (norcoclaurine synthase) DNA Sequence

> Δ29TfNCS SEQUENCE
GTTTAACTTTTAGGAGGTAAAACATATGTTGCATCACCAGGGTATCATCAATCAAGTTAG
CACCGTCACGAAAGTAATTCATCACGAGCTGGAAGTTGCGGCATCCGCTGACGACATTT
GGACCGTGTACAGCTGGCCGGGTCTGGCGAAGCACTTGCCGGATCTGCTGCCTGGCGC
GTTCGAAAAACTGGAGATTATCGGCGATGGCGGTGTTGGTACGATTCTGGACATGACCT
TTGTCCCGGGTGAATTCCCGCACGAGTATAAAGAGAAATTCATCCTGGTTGATAACGAAC
ATCGTCTGAAGAAGGTGCAGATGATCGAAGGCGGCTATCTGGACCTGGGTGTGACGTAT
TACATGGACACGATTCACGTTGTGCCGACCGGTAAAGACAGCTGCGTCATCAAGAGCAG
CACTGAGTACCACGTCAAGCCGGAGTTTGTGAAGATTGTTGAGCCGCTGATCACCACCG
GTCCACTGGCAGCCATGGCAGATGCCATTAGCAAGTTGGTCCTGGAACATAAATCTAAA
AGCAACTCCGATGAAATTGAGGCGGCGATCATCACCGTGCTGGAGCATCACCACCACCA
TCAC TGATAAAAGCTTCCCC

Denotes 6X Histidine tag

A.5 CV2025 TAm (transaminase) DNA sequence

>ENA|AAQ59697|AAQ59697.1 Chromobacterium violaceum
ATGCAGAAGCAACGTACGACCAGCCAATGGCGCGAACTGGATGCCGCCCATCACCTGC
ATCCGTTCACCGATACCGCATCGCTGAACCAGGCGGGCGCGCGCGTGATGACGCGCG
GAGAGGGCGTCTACCTGTGGGATTCGGAAGGCAACAAGATCATCGACGGCATGGCCGG
ACTGTGGTGCGTGAACGTCGGCTACGGCCGCAAGGACTTTGCCGAAGCGGCGCGCCG
GCAGATGGAAGAGCTGCCGTTCTACAACACCTTCTTCAAGACCACCCATCCGGCGGTGG
TCGAGCTGTCCAGCCTGCTGGCTGAAGTGACGCCGGCCGGTTTCGACCGCGTGTTCTA
TACCAATTCCGGTTCCGAATCGGTGGACACCATGATCCGCATGGTGCGCCGCTACTGGG
ACGTGCAGGGCAAGCCGGAGAAGAAGACGCTGATCGGCCGCTGGAACGGCTATCACG
GCTCCACCATCGGCGGCGCCAGCCTGGGCGGCATGAAGTACATGCACGAGCAGGGCG
ACTTGCCGATTCCGGGCATGGCCCACATCGAGCAGCCTTGGTGGTACAAGCACGGCAA
GGACATGACGCCGGACGAGTTCGGCGTGGTGGCCGCGCGCTGGCTGGAAGAGAAGAT
TCTGGAAATCGGCGCCGACAAGGTGGCCGCCTTCGTCGGCGAACCCATCCAGGGCGC
CGGCGGCGTGATCGTCCCGCCGGCCACCTACTGGCCGGAAATCGAGCGCATTTGCCGC
AAGTACGACGTGCTGCTGGTGGCCGACGAAGTGATCTGCGGCTTCGGGCGTACCGGCG
AATGGTTCGGCCATCAGCATTTCGGCTTCCAGCCCGACCTGTTCACCGCCGCCAAGGG
CCTGTCCTCCGGCTATCTGCCGATAGGCGCGGTCTTTGTCGGCAAGCGCGTGGCCGAA
GGCCTGATCGCCGGCGGCGACTTCAACCACGGCTTCACCTACTCCGGCCACCCGGTCT
GCGCCGCCGTCGCCCACGCCAACGTGGCGGCGCTGCGCGACGAGGGCATCGTCCAGC
GCGTCAAGGACGACATCGGCCCGTACATGCAAAAGCGCTGGCGTGAAACCTTCAGCCG
TTTCGAGCATGTGGACGACGTGCGCGGCGTCGGCATGGTGCAGGCGTTCACCCTGGTG
AAGAACAAGGCGAAGCGCGAGCTGTTCCCCGATTTCGGCGAGATCGGCACGCTGTGCC
GCGACATCTTCTTCCGCAACAACCTGATCATGCGGGCATGCGGCGACCACATCGTGTCG
GCGCCGCCGCTGGTGATGACGCGGGCGGAAGTGGACGAGATGCTGGCGGTGGCGGAA
CGCTGTCTGGAGGAATTCGAGCAGACGCTGAAGGCGCGCGGGCTGGCTTAG

A.6 pET29a-CV_2025 plasmid map

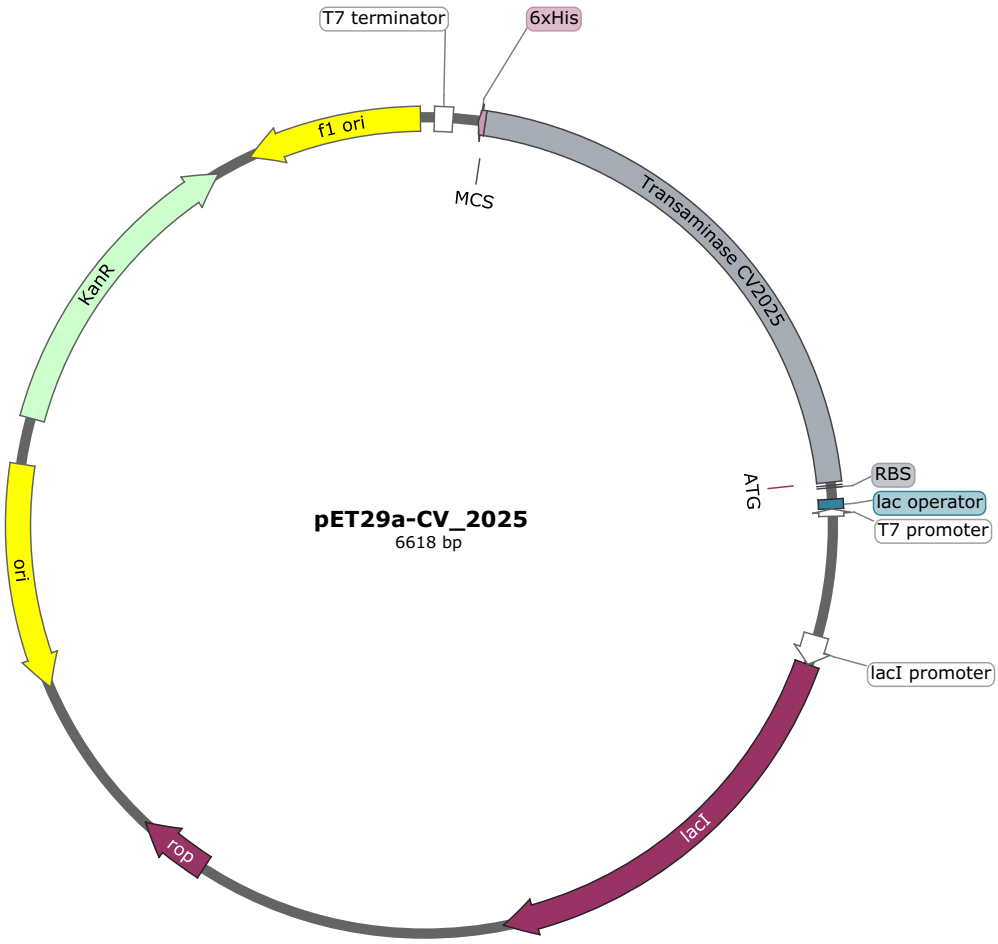

Appendix B

B.1 pBluescript II SK (-) sequence

>pBluescript SK (-)
CACCTGACGCGCCCTGTAGCGGCGCATTAAGCGCGGCGGGTGTGGTGGTTACGCGCAGCGTGAC
CGCTACACTTGCCAGCGCCCTAGCGCCCGCTCCTTTCGCTTTCTTCCCTTCCTTTCTCGCCACGTT
CGCCGGCTTTCCCCGTCAAGCTCTAAATCGGGGGCTCCCTTTAGGGTTCCGATTTAGTGCTTTACG
GCACCTCGACCCCAAAAAACTTGATTAGGGTGATGGTTCACGTAGTGGGCCATCGCCCTGATAGA
CGGTTTTTCGCCCTTTGACGTTGGAGTCCACGTTCTTTAATAGTGGACTCTTGTTCCAAACTGGAAC
AACACTCAACCCTATCTCGGTCTATTCTTTTGATTTATAAGGGATTTTGCCGATTTCGGCCTATTGGT
TAAAAAATGAGCTGATTTAACAAAAATTTAACGCGAATTTTAACAAAATATTAACGCTTACAATTTCCA
TTCGCCATTCAGGCTGCGCAACTGTTGGGAAGGGCGATCGGTGCGGGCCTCTTCGCTATTACGCC
AGCTGGCGAAAGGGGGATGTGCTGCAAGGCGATTAAGTTGGGTAACGCCAGGGTTTTCCCAGTCA
CGACGTTGTAAAACGACGGCCAGTGAATTGTAATACGACTCACTATAGGGCGAATTGGGTACCGG
GCCCCCCCTCGAGGTCGACGGTATCGATAAGCTTGATATCGAATTCCTGCAGCCCGGGGGATCCA
CTAGTTCTAGAGCGGCCGCCACCGCGGTGGAGCTCCAGCTTTTGTTCCCTTTAGTGAGGGTTAATT
TCGAGCTTGGCGTAATCATGGTCATAGCTGTTTCCTGTGTGAAATTGTTATCCGCTCACAATTCCAC
ACAACATACGAGCCGGAAGCATAAAGTGTAAAGCCTGGGGTGCCTAATGAGTGAGCTAACTCACAT
TAATTGCGTTGCGCTCACTGCCCGCTTTCCAGTCGGGAAACCTGTCGTGCCAGCTGCATTAATGAA
TCGGCCAACGCGCGGGGAGAGGCGGTTTGCGTATTGGGCGCTCTTCCGCTTCCTCGCTCACTGAC
TCGCTGCGCTCGGTCGTTCGGCTGCGGCGAGCGGTATCAGCTCACTCAAAGGCGGTAATACGGTT
ATCCACAGAATCAGGGGATAACGCAGGAAAGAACATGTGAGCAAAAGGCCAGCAAAAGGCCAGGA
ACCGTAAAAAGGCCGCGTTGCTGGCGTTTTTCCATAGGCTCCGCCCCCCTGACGAGCATCACAAA
AATCGACGCTCAAGTCAGAGGTGGCGAAACCCGACAGGACTATAAAGATACCAGGCGTTTCCCCC
TGGAAGCTCCCTCGTGCGCTCTCCTGTTCCGACCCTGCCGCTTACCGGATACCTGTCCGCCTTTCT
CCCTTCGGGAAGCGTGGCGCTTTCTCATAGCTCACGCTGTAGGTATCTCAGTTCGGTGTAGGTCGT
TCGCTCCAAGCTGGGCTGTGTGCACGAACCCCCCGTTCAGCCCGACCGCTGCGCCTTATCCGGTA
ACTATCGTCTTGAGTCCAACCCGGTAAGACACGACTTATCGCCACTGGCAGCAGCCACTGGTAACA
GGATTAGCAGAGCGAGGTATGTAGGCGGTGCTACAGAGTTCTTGAAGTGGTGGCCTAACTACGGC
TACACTAGAAGGACAGTATTTGGTATCTGCGCTCTGCTGAAGCCAGTTACCTTCGGAAAAAGAGTT
GGTAGCTCTTGATCCGGCAAACAAACCACCGCTGGTAGCGGTGGTTTTTTTGTTTGCAAGCAGCAG
ATTACGCGCAGAAAAAAAGGATCTCAAGAAGATCCTTTGATCTTTTCTACGGGGTCTGACGCTCAG
TGGAACGAAAACTCACGTTAAGGGATTTTGGTCATGAGATTATCAAAAAGGATCTTCACCTAGATCC
TTTTAAATTAAAAATGAAGTTTTAAATCAATCTAAAGTATATATGAGTAAACTTGGTCTGACAGTTACC
AATGCTTAATCAGTGAGGCACCTATCTCAGCGATCTGTCTATTTCGTTCATCCATAGTTGCCTGACT
CCCCGTCGTGTAGATAACTACGATACGGGAGGGCTTACCATCTGGCCCCAGTGCTGCAATGATAC
CGCGAGACCCACGCTCACCGGCTCCAGATTTATCAGCAATAAACCAGCCAGCCGGAAGGGCCGA
GCGCAGAAGTGGTCCTGCAACTTTATCCGCCTCCATCCAGTCTATTAATTGTTGCCGGGAAGCTAG
AGTAAGTAGTTCGCCAGTTAATAGTTTGCGCAACGTTGTTGCCATTGCTACAGGCATCGTGGTGTC
ACGCTCGTCGTTTGGTATGGCTTCATTCAGCTCCGGTTCCCAACGATCAAGGCGAGTTACATGATC
CCCCATGTTGTGCAAAAAAGCGGTTAGCTCCTTCGGTCCTCCGATCGTTGTCAGAAGTAAGTTGGC
CGCAGTGTTATCACTCATGGTTATGGCAGCACTGCATAATTCTCTTACTGTCATGCCATCCGTAAGA
TGCTTTTCTGTGACTGGTGAGTACTCAACCAAGTCATTCTGAGAATAGTGTATGCGGCGACCGAGT
TGCTCTTGCCCGGCGTCAATACGGGATAATACCGCGCCACATAGCAGAACTTTAAAAGTGCTCATC
ATTGGAAAACGTTCTTCGGGGCGAAAACTCTCAAGGATCTTACCGCTGTTGAGATCCAGTTCGATG
TAACCCACTCGTGCACCCAACTGATCTTCAGCATCTTTTACTTTCACCAGCGTTTCTGGGTGAGCAA
AAACAGGAAGGCAAAATGCCGCAAAAAAGGGAATAAGGGCGACACGGAAATGTTGAATACTCATAC
TCTTCCTTTTTCAATATTATTGAAGCATTTATCAGGGTTATTGTCTCATGAGCGGATACATATTTGAAT
GTATTTAGAAAAATAAACAAATAGGGGTTCCGCGCACATTTCCCCGAAAAGTGC

B.2 pBluescript II SK (-) plasmid map

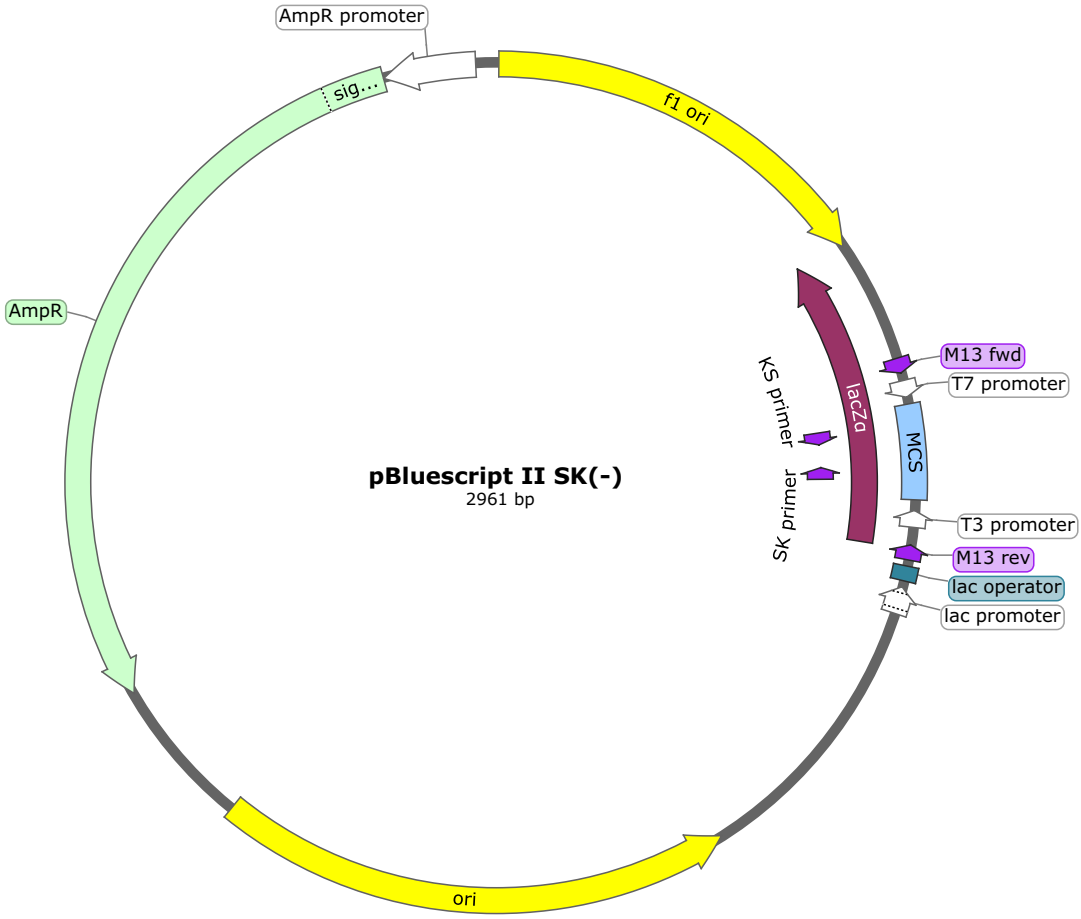

B.2 Oligonucleotide sequences used in chapter 5

Oligonucleotide name	Sequence 5’ -> 3’ (length bases)
1	GCACTTTTCGGGGAAATGTGCGCGTCCACTATTAAAGAACGTGGACTC (25)
2	TGTTGTTCCAGTTTGGAACAAGAGGAACCCCTATTTGTTTATTTTTCT (25)
3	AACGCTGGTGAAAGTAAAAGATGCCGCACCGATCGCCCTTCCCAACAG (25)
4	AGCTGGCGTAATAGCGAAGAGGCCTGAAGATCAGTTGGGTGCACGAGT (25)
5	CACTATTCTCAGAATGACTTGGTTCTGCAGGAATTCGATATCAAGCTT (25)
6	TCTAGAACTAGTGGATCCCCCGGGGAGTACTCACCAGTCACAGAAAAG (25)
7	ATCGTTGGGAACCGGAGCTGAATGGCTCACTCATTAGGCACCCCAGGC (25)
8	GCGCAACGCAATTAATGTGAGTTAAAGCCATACCAAACGACGAGCGTG (25)
9	TATTGCTGATAAATCTGGAGCCGGGTATTACCGCCTTTGAGTGAGCTG (25)
10	TATCCCCTGATTCTGTGGATAACCTGAGCGTGGGTCTCGCGGTATCAT (25)
11	ATACTTTAGATTGATTTAAAACTTCCAGGGGGAAACGCCTGGTATCTT (25)
12	ACAGGAGAGCGCACGAGGGAGCTTCATTTTTAATTTAAAAGGATCTAG (25)
13	TACCAGCGGTGGTTTGTTTGCCGGACGATAGTTACCGGATAAGGCGCA (25)
14	GTGTCTTACCGGGTTGGACTCAAGATCAAGAGCTACCAACTCTTTTTC (25)
conjcapture-1	CAACGTCAAAGGGCGAAAAAGAGAAGTGAAGTAAGTGAGTATGTA
conjcapture-2	CCGTCTATCAGGGCGATGGCGAGAAGTGAAGTAAGTGAGTATGTA
conjcapture-3	CCACTACGTGAACCATCACCGAGAAGTGAAGTAAGTGAGTATGTA
conjcapture-4	CTAATCAAGTTTTTTGGGGTGAGAAGTGAAGTAAGTGAGTATGTA
conjcapture-5	CGAGGTGCCGTAAAGCACTAGAGAAGTGAAGTAAGTGAGTATGTA
conjcapture-6	AATCGGAACCCTAAAGGGAGGAGAAGTGAAGTAAGTGAGTATGTA
conjcapture-7	CCCCCGATTTAGAGCTTGACGAGAAGTGAAGTAAGTGAGTATGTA
conjcapture-8	GGGGAAAGCCGGCGAACGTGGAGAAGTGAAGTAAGTGAGTATGTA
conjcapture-9	GCGAGAAAGGAAGGGAAGAAGAGAAGTGAAGTAAGTGAGTATGTA

conjcapture-10	AGCGAAAGGAGCGGGCGCTAGAGAAGTGAAGTAAGTGAGTATGTA
conjcapture-11	GGGCGCTGGCAAGTGTAGCGGAGAAGTGAAGTAAGTGAGTATGTA
conjcapture-12	GTCACGCTGCGCGTAACCACGAGAAGTGAAGTAAGTGAGTATGTA
conjcapture-13	CACACCCGCCGCGCTTAATGGAGAAGTGAAGTAAGTGAGTATGTA
conjcapture-14	CGCCGCTACAGGGCGCGTCAGGTGGAGAAGTGAAGTAAGTGAGTATGTA
Comp A S Cy5	[ThiC6] ACATCTACCTACCCTCCATC [Cyanine5]

B.3 Lysine decarboxylase enzyme DNA sequence

>Lysine Decarboxylase_87095
ATGAATATAGCAGTATTTTGTTCTGCAAATAATAACATTGCTCCCGACTACTTCCGTGCTG
CGGAAGAGTTGGGACGATGGATTGGAGAGAATGGGCATACGCTCGTTTATGGTGGAGC
CAACAGTGGATTGATGGAGTGTATTGGTAAAGCTGTACACGAAGCTGGTGGACGTACTA
TCGGAGTTATCCCTCGTATCTTAGAGGAAGGACGTAGAGTTAGCGACTATGTAGATGTA
GATATTCCTTGTGAGGACCTTACTGATCGCAAGGCAATCATTATGGAACGCTCTGATGAG
TTCTATGCTTTACCAGGTGGTATCGGAACAATTGATGAAATTTTCACTGTTGCAGCCTCT
GCTTCTATTGGTTATCATCATAAGAAGGTTACCTTAGTCAACGTGCAGGGCTTCTGGGAT
AGTCTTATTGCCCTGCTAAATGACCAACAAGAAAAAGGTATGATGCGTGGTAGACTCCAC
GATTATATAGAGATTAAGAATATAGACGACTTTTAA

B.3 pET29a(+)-deC_ 87095 plasmid map

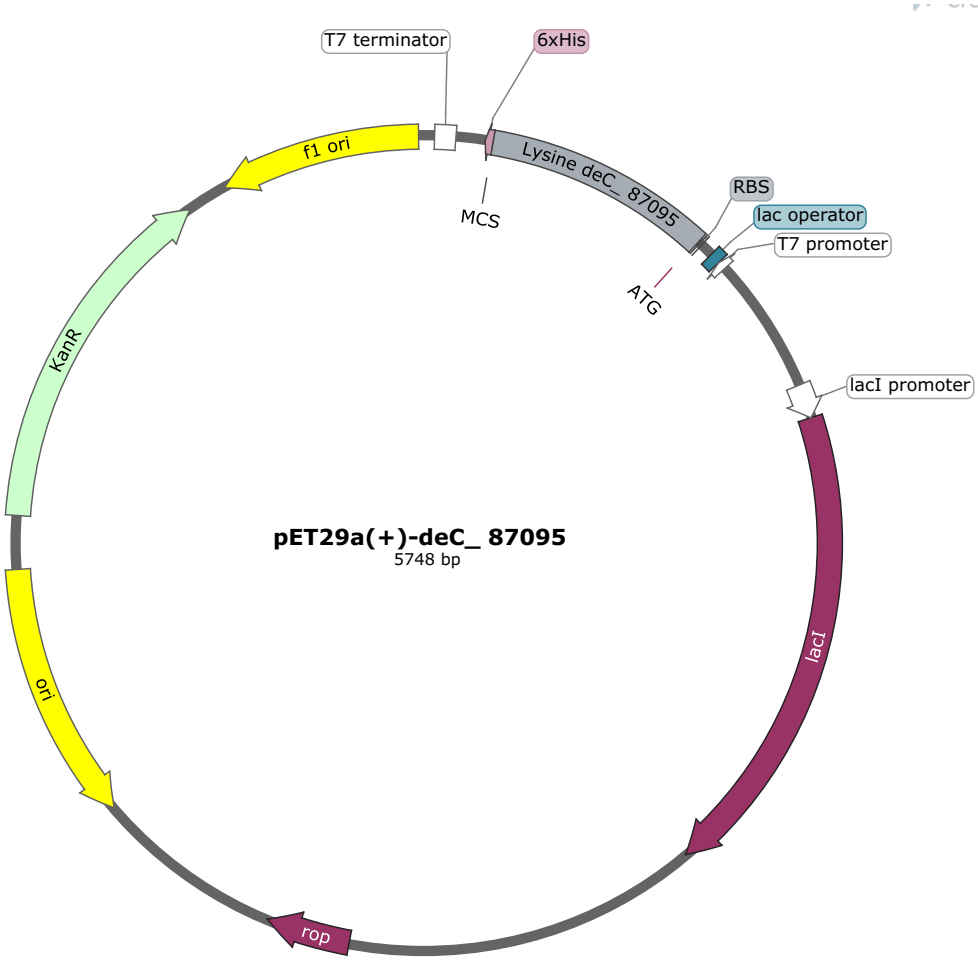

Appendix C

C.1 Oligonucleotides described for the polyhedral structure in chapter 6

Oligonucleotide name	Sequence 5’ -> 3’ (length b)
A-3	TTTGGTTAGAGACCTATG TGCAGTGGAGGAGATCT TC AAA CTGCGGTCTCCAAGTACA ATCAGGTGT AGCTAAGGACGCACAAG CAC (87)
B-3	AGACGAACAGAAACTGA GT AAA TACTCACGTGTAGTTATC GTGTCGAAT CTAAGAACACGCACAAG CAC (87)
C-3	CTCTGTACACAAGTGAAT C AAA AATCCACATTATGTATAC ACTAGGTCA ACAATAGGATGCACAAGC AC (87)
D (A1.25-C2.13)	TCTCCTCCACTGCACATA GGTCTGACCTAGTGTATA (54)
E (C1.25-B2.13)	ACTTGTGTACAGAGATGT ATCAATTCGACACGATAA (54)
F (B1.25-A2.13)	TTGGAGACCGCAGACTC AGTTTCTGTTCGTCTCAA TATCAACACCTGATTGTA C (54)
G (A2.25-B1.13)	GTCCTTAGCTACTAATCG TCGTGCTTGTGC (30)
H (B2.25-C1.13)	GTGTTCTTAGGATTAACT GAGTGCTTGTGC (30)
I (C2.25-A1.13)	ATCCTATTGTTCTAACCA AAGTGCTTGTGC (30)